

Numerical Simulation Study of Plasma Flow in the  
GAMMA 10/PDX End-cell by Using a Fluid Code

Hisato Takeda  
Doctoral Program in Physics

Submitted to the Graduate School of  
Pure and Applied Sciences  
in Partial Fulfillment of the Requirements  
for the Degree of Doctor of Philosophy in  
Science

at the  
University of Tsukuba

## Contents

Chapter 1. Introduction .....	1
1.1 Nuclea Fusion .....	1
1.2 The Tokamak.....	5
1.3 Scrape-off-Layer and Divertor .....	6
1.3.1. Detachment Plasma .....	7
1.4 Linear Device .....	9
1.4.1 GAMMA 10/PDX .....	9
1.5 Numerical Simulation for Divertor Plasma.....	12
1.5.1 The Importance of Numerical Simulation for Studying SOL Plasma.....	12
1.5.2 The Numerical Simulation in The Linear Device for Divertor Study.....	13
1.6 Objection Reserch and Outline This Thesis .....	13
Chapter 2. Physical Model of Plasma Transport in The Linear Fusion Devices for Divertor Study	15
2.1 Inroduction.....	15
2.2 Basic Equations .....	15
2.3 The Transport Coefficents.....	18
2.4 The Mesh Structure.....	20
2.5 The Boundary Conditions .....	21
2.6 Numerical Suchme to Solve The Fluid Equations .....	22
2.6.1 Characteristics of Convergence in The Numerical Solusions .....	23
Chapter 3. Simulation Results .....	26
3.1 Introduction .....	26
3.2 The Characteristic Plasma of GAMMA 10/PDX in The End-cell.....	26
3.2.1 The Basic Features of The End-loss Plasma with The Magentic Tube Expansion in The GAMMA 10/PDX West End-cell .....	26
3.2.2 The Systematic Comprison Between Cylindrical and Expanded Magnetic Configuration .....	28
3.3 Injection of Neutral or Impurity Gas into The End-cell.....	36
3.3.1 Reducing Plasma Energy by Injecting Neutral or Impurity Gas into Plasma .....	36
3.3.2 Axial Distibution in Standard Condition.....	37
3.3.3 Effect of Additional Neutral Hydrogen in Low Temperature Condition .....	41
3.3.4 Effect of Impurity Gas .....	43
Chapter 4. Simulation Results with The Extended Numerical Domain and Multi-Fluids Modeling .....	45
4.1 The Expansion of The Mesh Structure and of Muti-Fluid Code.....	45
4.1.1 The Expansion of Mesh from Plug/Barrier Cell to End Cell .....	45
4.1.2 Extending Multi-Fluid Code .....	48

4.2	Injection of Neutral and/or Impurity Gas into Edge Plasma by Using Multi-Fluid Code..	50
4.2.1	The Only Neutral Hydrogen Gas Injection.....	50
4.2.2	The Only Ar Injection Effects .....	53
4.2.3	Simulataneous Injection of Hydrogen and Argon Gases .....	60
Capter 5.	The combining test the DEGAS code with fluid code .....	70
5.1	The DEGAS code.....	70
5.2	The method of copling DEGAS code with fluid code.....	71
Capter 6.	Conclusion.....	76
6.1	Adadting fluid code in GAMMA 10/PDX.....	76
6.2	Conparision between cylindrical and expand magnetic configuration.....	77
6.3	Injection of neutral or impurity gas into the end-cell by using single fluid code.....	77
6.4	Injection of neutral or impurity gs into the end-cell by using multi-fluid code .....	78
6.5	The test comboninig with DEGAS code .....	79
6.6	Concluding Remark .....	79
Reference	.....	80
Acknowledgments	.....	84

# Chapter 1

## Introduction

### 1.1 Nuclear Fusion

The development of new energy sources will be required because energy consumption in the world keeps increasing as the years rolled on. In addition, the problems such as global warming and depletion of energy sources are expected due to deriving most of present energy from fossil fuel at present. Additionally, the population of the world is expected to increase to about ninety three hundred million due to rising the population in the developing country such as Asia region in 2050. With rising global population, it is considered that the increasing trend in the amount of energy consumption becomes increasingly large. The energy consumption in 2030 is expected to be 1.4 as large as in 2014.

For addressing the rising needed energy in the future, nuclear fusion power generation most appears promising with the object of the economy and low environment load. Typical nuclear fusion reactions exist (1.1) D-D reaction, (1.2) D-T reaction and (1.3) D-He<sup>3</sup> reaction. Figure1 shows the energy dependence of the rate coefficient of reactions (1.1), (1.2) and (1.3).

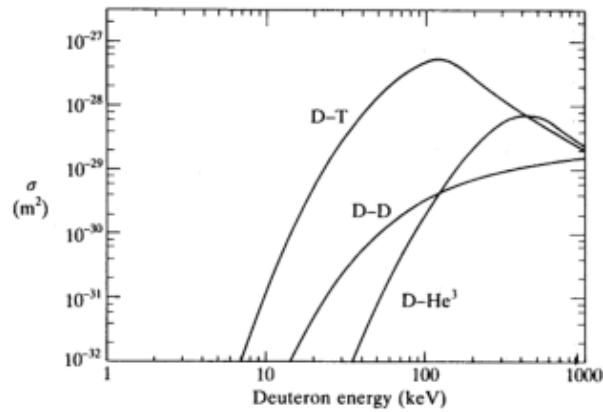


Fig. 1 The rate coefficient of nuclear fusion reactions D-T, D-D and D-<sup>3</sup>He.

Here, D and T indicate hydrogen isotopes deuterium and tritium. The neutron and proton are represented as n and p in above equations. D-<sup>3</sup>He reaction has an advantages in producing the largest energy and no neutron. However the reaction rate is low. Therefore, D-T reaction is chosen as a candidate for the first generation nuclear fusion reactors because of high reaction rate and the large energy production following D-<sup>3</sup>He reaction. It is needed that T (tritium) is generated by reaction of Li and neutron produced D-T reaction in the reactor because almost no T exists in the natural world. A few amount of Li causes barrier of energy source for nuclear fusion reactor. However, the method extracting Li from the sea has been developed [1, 2, 3]. The anticipated amount of Li is expected to be able to run one thousand nuclear fusion reactors for twenty-three million years [4].

The view showing the frame format of nuclear fusion reactor (ITER) is shown in Fig. 2. In the nuclear fusion reactor used D-T reaction, it is necessary to generate T and take out thermal energy produced by D-T reaction by installing blanket outside the first wall. To keep thermal nuclear fusion reaction, the energy input for heating plasma must be less than the output energy from the reactor.

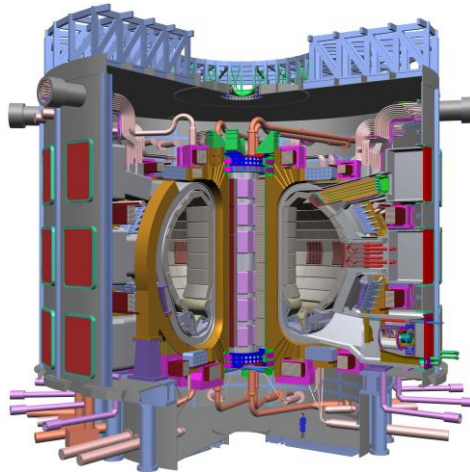


Fig. 2 The schematic of the nuclear fusion reactor, ITER.

The energy balance equation for fusion core plasma is shown as follows,

$$\frac{d}{dt}(3n_i T) = P_\alpha + P_H - P_L = \frac{n_i^2}{4} \langle \sigma v \rangle E_\alpha + P_H - \frac{3n_i T}{\tau_E}, \quad (1.4)$$

where,

$3n_i T$ : The sum of electron and ion thermal energy per unit volume.

$P_\alpha$ : Alpha particle heating power.

$P_H$ : Input power of additional plasma heating power

$P_L$ : Energy loss power from plasma.

In a steady state operation, Eq. (1.4) is represented as follows,

$$n_i \tau_E = \frac{3n_i^2 T}{P_\alpha + P_H} = \frac{12T}{\langle \sigma v \rangle E_\alpha \left(\frac{1+A}{Q}\right)} \quad (1.5)$$

$Q$ : The ratio output of nuclear fusion to input of heating power. That is  $Q = P_F / P_H$ .  $P_F$  is defined as all power generated by the nuclear fusion reaction.

$A$ : The ratio of alpha particle heating power to all power output by nuclear fusion reaction. "A" is defined as  $A = P_F / P_\alpha$ .

The condition " $Q = 1$ " is called critical plasma condition. On the other hand, the condition of  $Q = \infty$  is called self-ignition condition. In the self-ignition condition, once nuclear fusion reaction is occurred, only alpha particle heating keeps inducing nuclear reaction without external input heating energy. If  $Q$ -value is constant,  $n_i \tau_E$  becomes function dependent on only plasma temperature by (1.5). The dependence property of  $Q = 1$  or  $Q = \infty$  is called at Lawson diagram. The diagram shown in Fig. 3 is important for indicating plasma confinement capability.

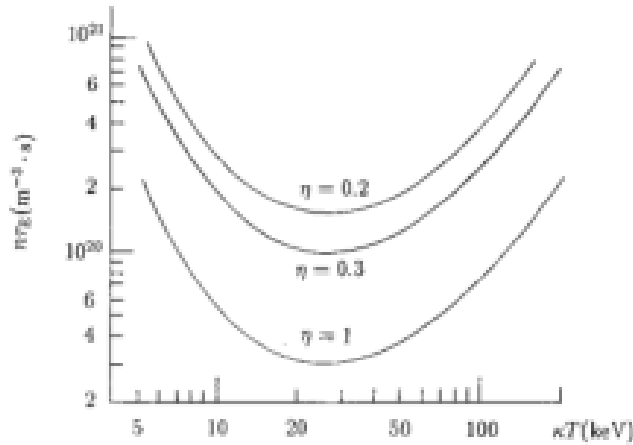


Fig. 3 T -  $n\tau$  diagram

In general, upper limit of the plasma density is decided by heat load toward the vacuum vessel. If it is assumed that heat load toward the first wall is allowed to 5 MW / m<sup>2</sup>, it is considered that maximum plasma density becomes about 10<sup>20</sup> ~ 10<sup>21</sup> m<sup>-3</sup>. Generating and confining high temperature plasma will lead to achieve the nuclear fusion.

## 1.2 Tokamak

For achieving nuclear fusion reaction, it is needed that high temperature plasma is confined. Currently, the most promising concept of nuclear fusion reactor is tokamak which is magnetic confinement fusion reactor [5, 6]. The tokamak is designed by Igor Tamm and Andrei Sakharov who are Russian scientists. The shape of the tokamak fusion reactor is circularity like a doughnut shown in Fig. 4.

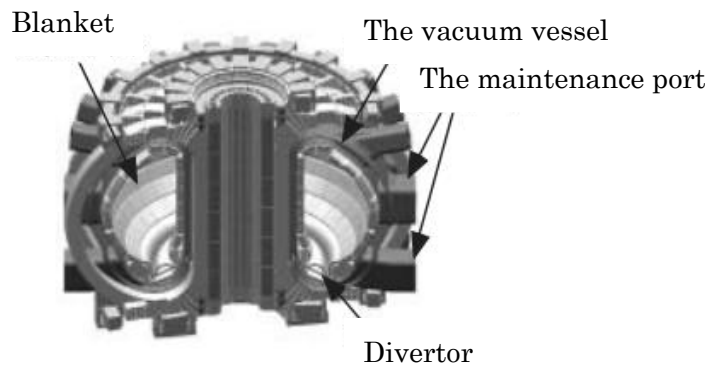


Fig. 4 The shape of the tokamak fusion reactor.

The periphery direction of torus is called toroidal direction. In addition, the direction perpendicular to the toroidal direction is called poloidal direction. The magnetic configuration of tokamak becomes helical trajectory around the torus because the magnetic field is configured by summation of the toroidal magnetic field along with torus and the poloidal magnetic field generated by plasma current in the tokamak plasma. The experiments and studies for nuclear fusion are performed by using the tokamak fusion reactor which is built and improved in the world. Also, the tokamak fusion reactor is adopted as the design of International Thermonuclear Experimental Reactor (ITER).

### 1.3 Scrape-off-Layer and Divertor

In the magnetic confinement fusion reactors such as tokamak, high temperature and density plasmas confined in the core region flow out toward the vacuum vessel. When plasma diffused from core hits to the wall, the impurity gas and particulates arise from the wall. If impurity particles penetrate into the core region, the core plasma is cooled by interaction between the core plasma and impurities. This processes interferes with nuclear fusion reaction. Therefore, magnetic configuration of scrape-off-layer region is improved to the divertor magnetic configuration shown in Fig.5. The divertor magnetic configuration has a sepatartix. The sepatartix is a surface which separates magnetic field into two regions. One is closed magnetic surface in the core region. The

other is opened magnetic surface at the edge region. At the end of open magnetic field, divertor plate made by carbon or tungsten and so on is installed. The impurity ion and low temperature ion transported along the magnetic field line is neutralized at the divertor plate surface recombination. The part of neutrals produced by the surface recombination is re-ionized by plasma from SOL region and the ions flow toward the divertor plate, again. Therefore, plasma parameters such as  $T_e$ ,  $n_e$  and pressure are varied widely by increasing the interaction between charge particles and neutral in the divertor region in Fig.6. The particles passing between plasma and neutral is pumped by the pump installed near the divertor plate.

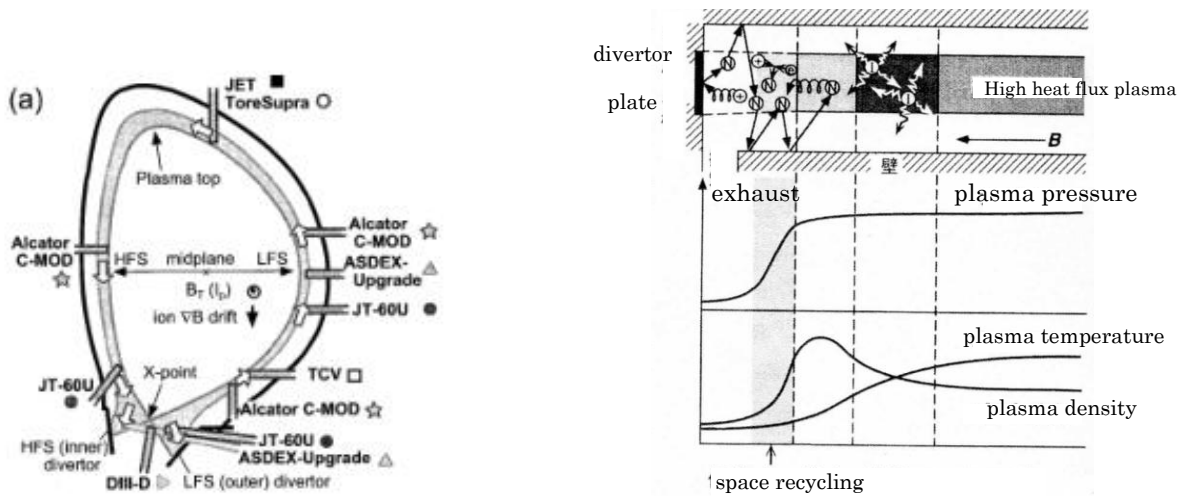


Fig. 5 The divertor magnetic configuration in tokamak. Fig. 6 The interactions between charge and neutral particles in the divertor region.

By adapting the divertor magnetic configuration, plasma confinement is improved dramatically. However, divertor configuration particle and heat fluxes from diffused core region plasma are localized onto the divertor plate. It is expected that the heat flux at the divertor plate reaches about  $10 \sim 20 \text{ MW/m}^2$  without the countermeasure. If this high heat load is put on the divertor plate, divertor plate made does not endure the heat load. Therefore, it is needed that heat and particle flux at the divertor plate is reduced. For decreasing heat and particle fluxes, the following schemes are proposed :

1. Increasing radiation cooling,
2. The formation of the detached plasma which does not contact with the divertor plate near the divertor plate,
3. Expansion of magnetic field line in the divertor region are considered.

### 1.3.1 Detached plasma

As noted above, detached plasma is the state in which plasma cannot reach the divertor plate. For forming detached plasma, to reduce electron temperature  $T_e$  below 5 eV is needed under the condition of high plasma density because it is needed that the effect of volume recombination becomes the dominant process by enhanced the ion momentum loss. Detachment state includes three processes. The first is the reduction of heat load. By increase of plasma density, interaction between plasma and impurity or neutral is enhanced largely. As a results, the heat load on the divertor plate reduces because of decrease in plasma temperature in the divertor region. The second is the reduction of plasma pressure near the divertor plate. Charge exchange reaction becomes dominant because the electron-impact ionization tends to become less by low  $T_e$ . At charge exchange reaction, the high energy plasma is transformed to neutral particles, and neutral particles are lost in the divertor region. The momentum of plasma is scattered and lost to the wide region because neutral does not subject to magnetic field line. For such occasions, plasma pressure is reduced. The third is reduction of particle flux on the divertor plate. In the case of  $T_e < 1$  eV, ( plasma ) volume recombination reaction is dominant in all other reactions. As a results, plasma near the target plate disappears. For this reason, particle flux reached the divertor plate decreases greatly.

Detached plasma is observed in tokamak experiments as well as these in linear devices [7, 8, 9, 10, 11]. The example of detachment in the linear device is shown Fig. 7 [12]. In Fig. 7, the plasma pressure decreases along with magnetic field line. Especially, the reduction of plasma pressure under the condition of high electron density is larger than low electron density. Under the high electron density, it is observed that plasma pressure disappears. This results shows the phenomena of detached plasma.

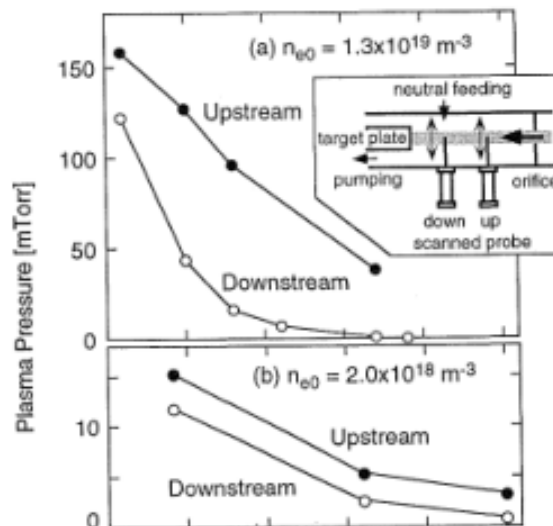


Fig. 7 Dependence of plasma pressure on neutral gas pressure. The plasma pressure at two different positions are estimated by the  $n_e$  and  $T_e$  measured with the scanned probe in (a) high plasma density ( $I_p \sim 67A$ ) and (b) low plasma density ( $I_p \sim 10A$ ) Ref. [11].

## 1.4 Linear devices

Linear devices have several advantages such as plasma controllability, convenience of experimental measurements due to the simple geometry and steady state operation for studying divertor plasma. Therefore, linear machine has contributed for tokamak divertor physics such as plasma material interaction and plasma transport in the SOL or divertor region. Moreover, numerical modeling of plasma behavior is required in order to translate the results of linear device plasma experiments to the SOL region and divertor region.

In the world, studies of divertor physics have been performed energetically. These linear devices focus on different physics. PISCES which is at University of California in the USA is operated for analyzing impurity transport mainly. NAGDIS-II which is at Nagoya University in Japan is performed in order to study non-linear phenomena such as Blob transport. JULE-PSI which is at Forschungszentrum Julich in Germany will start studying neutron injection effects into the materials. Magnum-PSI which is at FOM Institute DIFFER in Netherland achieved high particle flux and plasma parameter equaled to ITER divertor parameters.

### 1.4.1 GAMMA 10/PDX

The GAMMA 10/PDX ( "GAMMA 10" and "GAMMA Potential-control and Divertor-simulation eXperiments" ) tandem mirror in the Plasma Research Center at University of Tsukuba is the world's largest linear device which has high ion temperature than others. The schematic view of GAMMA 10/PDX tandem mirror is shown in Fig. 8. GAMMA 10/PDX consists of 7 cells such as central cell, two anchor-cells, two plug/barrier-cells and two end-cells. High power plasma heating systems which are composed of ion cyclotron range of frequencies ( ICRF ) waves, neutral beam injection ( NBI ) and electron cyclotron heating ( ECH ) are installed for plasma production, heating and confinement. The hydrogen plasma generated mainly in the central-cell flows toward the end cells through other cells as a end-loss plasma. Ion temperature in the end-cell is obtained about 100 ~ 400 eV by using ICRF heating and electron temperature in the end-cell is about 30 eV. Other parameters are to be shown in Table 1. The divertor simulation experiments in GAMMA 10/PDX had been started by using end cell in GAMMA 10/PDX.

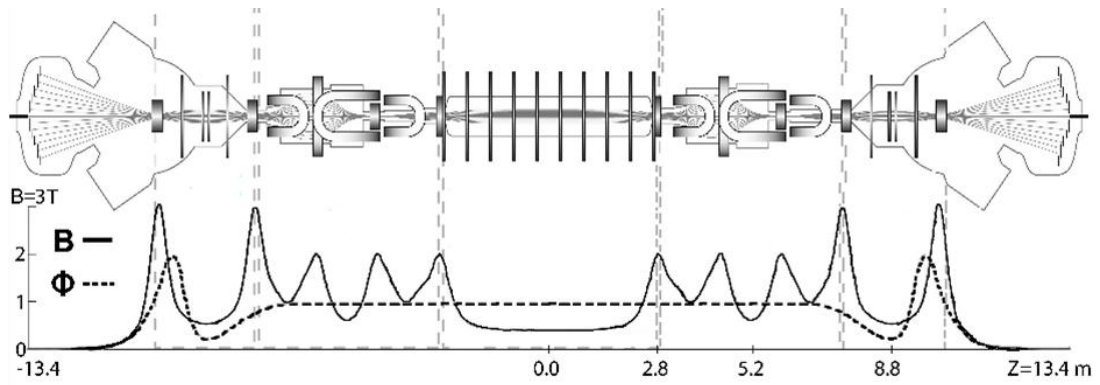


Fig. 8 The schematic view of GAMMA 10/PDX tandem mirror. It shows that the vacuum vessel, the installation positions of coils and line of magnetic force and electric potential configurations.

Table 1. End-loss plasma parameters in GAMMA 10/PDX

Plasma bore	0.1 ~ 1.0 m $\phi$
Plasma density	$\sim 10^{18}$ m $^{-3}$
Particle flux density	with $10^{22\sim 23}$ m $^2$ s $^{-1}$
Heat flux density	$\leq 1$ MW m $^{-2}$ (by ICRF), $\sim 10$ MW m $^{-2}$ (with ECH).
The discharge time	0.2 ~ 0.4 s
Fluence	$\sim 10^{21}$ m $^{-2}$ / shot, $\sim 10^{23}$ m $^{-2}$ / week

And so, it was needed that the values of heat and particle fluxes were estimated in case of regarding GAMMA 10/PDX as divertor simulation device. The results of heat and particle fluxes distribution in the end-cell are measured by using probe and calorimeter in Fig. 9 (a) and (b) [13].

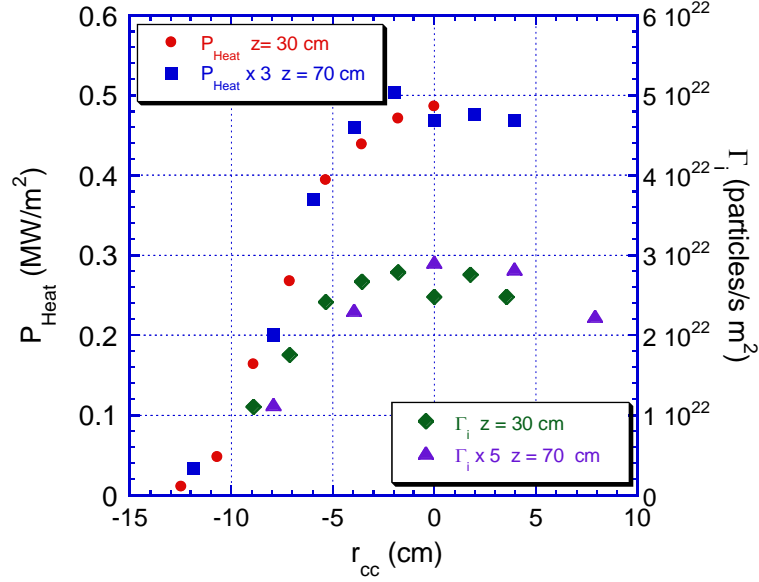


Fig. 9 (a) Radial distribution of heat and particle fluxes

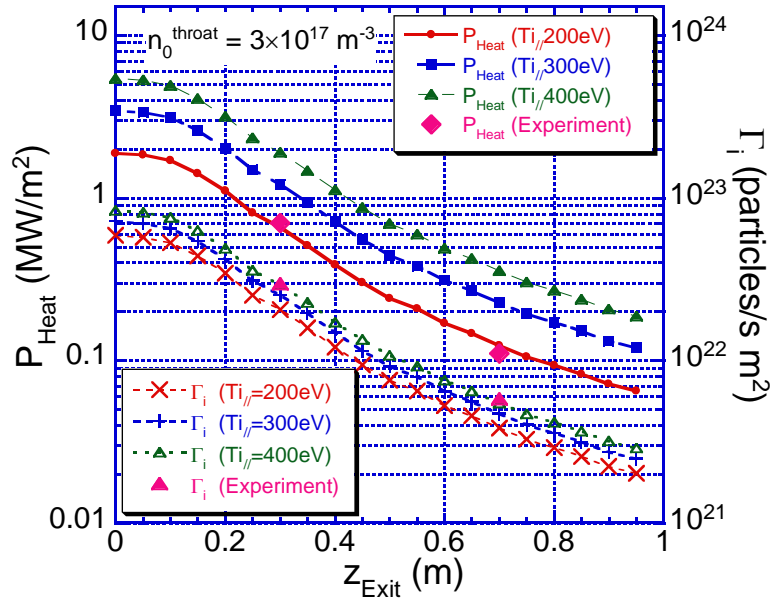


Fig. 9 (b) z axial distribution of heat and particle fluxes.

In Fig. 9 (a), each position is normalized at mid-plane position of the central-cell according to the shape of the magnetic flux tube. In both heat and particle profiles, it is found that a good agreement

is obtained. It is confirmed that the transport of the heat and particle flux from the end-mirror exit is basically governed by the magnetic field configuration in the end-mirror region under the collision less condition. Figure 9 (b) shows the z-axial distribution of heat and particle fluxes in the end-mirror region. Heat flux density in Fig. 9 (b) is corrected by the following particle reflection coefficients [14]. Measured results of heat and particle flux densities are agree with the calculation results which are considered magnetic configuration simply. The maximum consistent  $T_{i//}$  ( temperature of parallel to the line of magnetic force ) is estimated to be  $\sim 400$  eV. This ion temperature agrees in the result measured by ELIEA ( End Loss Ion Energy Analyzer ) [15, 16]. Moreover, heat and particle fluxes can be increased by handling plasma parameters in the central cell or heating conditions. Therefore, it is considered that performing the divertor simulation experiments in GAMMA 10/PDX have good prospects from these results.

## 1.5 Numerical simulation for divertor plasma

### *1.5.1 The importance of numerical simulation for studying SOL plasma*

The simulation of the plasma in the divertor and SOL regions is very important due to not only the evaluations heat load and particle flux reached the target plate and the understanding the divertor physics but also the core plasma confinement indicated in section 1.3. For example, the effects of plasma drifts to the SOL plasma and impurity transport, the physical mechanism of high speed plasma flow at generated detached plasma [17] and the dependence on the divertor geometric configuration and so on are elucidated by using simulation code. By clarifying the correct physical mechanism of plasma behaviors, not only the useful guideline of future reactor design and the safety of the plasma control in the reactors but also the evaluation of advanced methods for controlling the plasma behavior in the divertor region can be produced. The numerical simulation codes are used for studying plasma physics and modeling new reactor configuration in the world with comparison examinations between the codes included another physical assumptions.

In the divertor region, the interactions between charge particles and neutral is very important because the physics simulated in the divertor plasma conditions is characterized by the strong interaction between plasma and neutral. The numerical code to simulate the plasma behavior exists two main type of the fluid code and the Monte Carlo code. Naturally, the plasma transports along with magnetic field line therefore the connection length is more longer than the mean free path of the several collisions in the tokamaks. In this reason, the plasma behavior is calculated by using the fluid code. In addition, it is useful for the fluid assumptions to become the low calculation cost. The fluid code simulated SOL plasma is widely used in the world such as B2 [18], B2.5 [19, 20] and UEDGE [21]. On the other hand, the mean free path of neutral is almost always longer beyond adapting the fluid assumption. The neutral behavior depends on the geometrical configuration

because the neutral particles can freely transport without binding the magnetic field line. Therefore, the neutral is calculated by the kinetic code solving the Boltzmann equation such as EIRENE [22, 23, 24], DEGAS [25, 26] and NEUT2D [27]. These codes include the detail collision processes and use the Monte Carlo method. Especially, the collision processes is important due to dominant processes for the neutral behaviors.

### 1.5.2 *The numerical simulation in the linear device for divertor study*

Linear devices has simple magnetic field compared with tokamak magnetic configuration. It seems that physical mechanisms are analyzed obviously. Injecting neutral or impurity gases in the edge plasma is useful to reduce particle and heat load toward the divertor plate. However, it is concerned that neutral and/or impurity injection lead to the degradation of core plasma performance if they penetrate into core region. It is important to investigate plasma and impurity transport, and also the effects of the particle and heat reduction by injecting neutral and impurity.

Numerical simulation is useful for analyzing these phenomena. In addition, the existence of effective processes can be estimated or evaluated between other conditions. The combination use of the experimental results in the linear devices and the results of numerical simulation are performed in the world by using linear devices [28, 29, 30]. The numerical codes performed by simulating the plasma or neutral in the linear devices are used by the code which is used in the tokamak such as B2.5 and UEDGE. By adapting the codes used in the tokamak, the validity of algorism under the mixed different time scale conditions and the condition of the plasma parameters like near the detachment state is verified at the same time.

## 1.6 Objectives of the research and outline of this thesis

The purpose of this thesis is to clarify the effects of reduction heat load and particle flux toward the divertor plate and impurity transport in the divertor region at the GAMMA 10/PDX based on a numerical simulation using fluid code. Especially, we will make a comparative study with and without the effect of impurity ions such as argon and atomic molecule interactions. Finding knowledge and information is important under the high ion temperature condition which is different to other linear devices in the world for divertor studies.

After introducing the first chapter, Chapter 2 describes the physical model of edge plasma. Fluid equations, the boundary conditions and the transport coefficients are explained. In Chapter 3, the simulation results in case of the single fluid code are shown. Neutral particles considered only recycling neutrals or injected neutral gas are mentioned. In this section, It is assumed that impurity must not ionized in the plasma. In Chapter 4, simulation results calculated multi-fluid and extended the mesh structure to west plug/barrier cell are discussed. The difference of mesh

configuration is compared. In addition, more detail interactions between ions and neutral or impurity are introduced in the simulation code. In Chapter 5, neutral hydrogen particles is calculated not by a simple analytical solution but by using DEGAS code [25, 26]. Neutral is not constrained by magnetic field line. Therefore, more correct solutions are obtained by using Monte Carlo code than using fluid code or others because the distribution of neutral particles is largely depended on the structure geometry of the calculation space. Finally, this thesis is concluded in Chapter 6.

# Chapter 2

## Physical model of plasma transport in the linear fusion devices for divertor study

In the following Chapters, simulation results will be presented for plasma transport phenomena in GAMMA 10/PDX with a numerical simulation code developed in this study. The numerical code is based on the same fluid model as the B2-code, which has been originally developed by Braams [18] for the numerical simulation of tokamak SOL and divertor plasmas.

In this chapter, main assumptions and basic equations of the fluid code used in the present study will be summarized in Sec. 2.1. Then, transport coefficients used in the fluid model will be described in Sec.2.3. Finally, boundary conditions used in the analysis will be summarized in Sec.2.4.

### 2.1 Main assumptions and basic equations

As mentioned above, the basic equations in the present code is the same as the B2-code. They are originally based on the system of fluid equations derived by Braginskii [31]. Therefore, the system of fluid equations is sometimes called "Braginskii equations". The Braginskii equations are derived by taking the velocity moment of the Boltzmann equation. They consist in the B2 and the present code, the Braginskii equations are simplified by the following assumptions;

#### 1. Quasi-neutrality of plasma .

Continuity equations only for the ion species are solved, and the electron density  $n_e$  is assumed to be satisfied the relation  $n_e = \sum (i = 1, \dots, N_\alpha) Z_\alpha \times n_\alpha$ , where  $n_\alpha$  is the ion density with the charge state  $Z_\alpha$  and  $N_\alpha$  is the number of charge state. The total ion density is given by  $n_i = \sum (i = 1, \dots, N_\alpha) n_\alpha$ .

#### 2. Assumed electron mass as zero and only the momentum balance equation for the ion species.

Inertia term in electron momentum balance equation is taken to be zero. The resultant electron momentum balance equation together with the assumption 1 ( plasma quasi-neutrality ) is used to eliminate the Lorentz force term and Coulomb collision term in the ion momentum equation. As a results, only the ion momentum equations are solved.

#### 3. Two dimensional model

In the B2 code, the two dimensional model of tokamak plasmas has been developed on the basis of the toroidal axi-symmetry. The parallel component of the ion momentum equation is projected to the poloidal plane. The 2D simulations has been done in the poloidal plane of the tokamak magnetic configuration. The system of fluid equations are solved for the plasma density  $n_\alpha$ , plasma flow velocity  $u_{\parallel\alpha}$  parallel to the magnetic field, electron temperature  $T_e$  and ion temperature  $T_i$  are solved in the poloidal plane.

In the present model, we have developed 2D model of the mirror magnetic configuration in GAMMA 10/PDX linear device ad in the same manner as the B2 code. We assume the axi-symmetric of the GAMMA 10/PDX plasma, the dependence of physical quantities on the azimuthal angle ( theta ) in a cylindrical coordinate system ( r, theta, z ) has been neglected.

#### 4. Anomalous radial transport

Diffusion approximation is introduced instead of solving the radial component of the momentum equation in the radial direction.

#### 5. Simplified viscosity tensor

Cross-field derivative terms are neglect.

The equations take the following form.

- Continuity equation of species  $\alpha$

$$\frac{\partial n_\alpha}{\partial t} + \frac{\partial}{\partial x}(n_\alpha u_\alpha) + \frac{\partial}{\partial y}(n_\alpha v_\alpha) = S_n^\alpha. \quad (2.1)$$

- Momentum balance equation of species  $\alpha$

$$\begin{aligned} & \frac{\partial}{\partial t}(m_\alpha n_\alpha u_{\parallel\alpha}) + \frac{\partial}{\partial x}\left(m_\alpha n_\alpha u_\alpha u_{\parallel\alpha} - \eta_x^\alpha \frac{\partial u_{\parallel\alpha}}{\partial x}\right) + \frac{\partial}{\partial y}\left(m_\alpha n_\alpha v_\alpha u_{\parallel\alpha} - \eta_y^\alpha \frac{\partial u_{\parallel\alpha}}{\partial y}\right) \\ &= \frac{B_\theta}{B} \left[ -\frac{\partial p_\alpha}{\partial x} - \frac{Z_\alpha n_\alpha}{n_e} \frac{\partial p_e}{\partial x} + c_e \left(\frac{Z_\alpha}{Z_{eff}} - 1\right) Z_\alpha n_e \frac{\partial T_e}{\partial x} + c_i \left(\frac{Z_\alpha}{Z_{eff}} - 1\right) Z_\alpha n_\alpha \frac{\partial T_i}{\partial x} \right] \\ &+ \sum_{\beta=1}^N F_{\alpha\beta} + S_{mu\parallel}^\alpha. \end{aligned} \quad (2.2)$$

On the right side of Eq. (2.2), the first and the second terms are ion and electron pressure gradient forces along with magnetic field line, respectively. The third and fourth terms indicate thermal force from electron and ion. The symbols  $c_e$  and  $c_i$  are the coefficients of thermal force. Thermal force is very important, because it influences impurity transport.

- Diffusion approximation of species  $\alpha$  in the radial direction is used,

$$v_\alpha = -D_n^\alpha \frac{\partial}{\partial y} (\ln n_\alpha) \quad (2.3)$$

The coefficient  $D_n^\alpha$  is the diffusion coefficient. Generally, this coefficient is defined as including anomalous effects.

- Electron energy balance equation

$$\begin{aligned} \frac{\partial}{\partial t} \left( \frac{3}{2} n_e T_e \right) + \frac{\partial}{\partial x} \left( \frac{5}{2} n_e u_e T_e - \kappa_x^e \frac{\partial T_e}{\partial x} \right) + \frac{\partial}{\partial y} \left( \frac{5}{2} n_e v_e T_e - \kappa_y^e \frac{\partial T_e}{\partial y} \right) \\ = u_e \frac{\partial p_e}{\partial x} + v_e \frac{\partial p_e}{\partial y} - k(T_e - T_i) + S_E^e \end{aligned} \quad (2.4)$$

In the right side of equation, the first and second terms represent work done by the electric field. The third term is energy transfer between electron and ion by the Coulomb collision. The fourth term is volume sources of electron energy.

- Ion energy balance equation

$$\begin{aligned} \frac{\partial}{\partial t} \left( \frac{3}{2} n_i T_i + \sum_\alpha \frac{1}{2} \rho_\alpha u_{||\alpha}^2 \right) + \frac{\partial}{\partial x} \left[ \left( \sum_\alpha \frac{5}{2} n_\alpha u_\alpha T_i + \sum_\alpha \frac{1}{2} m_\alpha n_\alpha u_\alpha u_{||\alpha}^2 \right) - \left( \kappa_x^i \frac{\partial T_i}{\partial x} + \sum_\alpha \frac{1}{2} \eta_x^\alpha \frac{\partial u_{||\alpha}^2}{\partial x} \right) \right] \\ + \frac{\partial}{\partial y} \left[ \left( \sum_\alpha \frac{5}{2} n_\alpha v_\alpha T_i + \sum_\alpha \frac{1}{2} m_\alpha n_\alpha v_\alpha u_{||\alpha}^2 \right) - \left( \kappa_y^i \frac{\partial T_i}{\partial y} + \sum_\alpha \frac{1}{2} \eta_y^\alpha \frac{\partial u_{||\alpha}^2}{\partial y} \right) \right] \\ = -u_e \frac{\partial p_e}{\partial x} - v_e \frac{\partial p_e}{\partial y} + k(T_e - T_i) + S_E^i \end{aligned} \quad (2.5)$$

In the right side of Eq. (2.5), the first, second and third terms have the same effects as the term of electron energy balance. The fourth term is volume the source of ion energy. The total energy balance equation for ion with common ion temperature  $T_i$  is solved in this code.

Electron velocities, density and pressure are defined as

$$n_e = \sum_\alpha Z_\alpha n_\alpha, \quad u_e = \frac{1}{n_e} \sum_\alpha Z_\alpha n_\alpha u_\alpha, \quad v_e = \frac{1}{n_e} \sum_\alpha Z_\alpha n_\alpha v_\alpha, \quad p_e = n_e T_e. \quad (2.6)$$

The definition of effective charge state is:

$$Z_{eff} = \frac{\sum_\alpha Z_\alpha^2 n_\alpha}{\sum_\alpha Z_\alpha n_\alpha} \quad (2.7)$$

## 2.2 The transport coefficients

As for the parallel transport, classical transport coefficients are used. The transport coefficients are different between single fluid and multi fluid. In case of single fluid, the transport coefficients are indicated [kotov 53]. On the other hand, the coefficients used in multi-fluid are defined as simplification of the complete multi-species transport theory [31].

- Classical thermal conductivity coefficient of electron:

$$\text{Simple plasma} \quad \kappa_{\parallel}^e = \frac{2.4}{e^4 \sqrt{2\pi m_e}} \frac{T_e^{\frac{5}{2}}}{Z \ln \Lambda} \quad (2.8)$$

$$\text{Multiple ion species} \quad \kappa_{\parallel}^e = 3.488 \times 10^{-4} \frac{n_e T_e}{m_e Z_{eff}} \frac{T_e^{\frac{3}{2}}}{\left(\frac{n_e}{10^{20}}\right) \ln \Lambda} \quad (2.9)$$

In case of multiple ion species, Braginskii's form collision between ion and electron is considered.

- Classical thermal conductivity coefficient of ion

$$\text{Simple plasma} \quad \kappa_{\parallel}^i = 3.9 \frac{12\pi\sqrt{\pi}\epsilon_0^2}{e^4} \frac{T_i^{\frac{5}{2}}}{\ln \Lambda} \quad (2.10)$$

$$\text{Multiple ion species} \quad \kappa_{\parallel}^i = 3.9 \frac{12\pi\sqrt{\pi}\epsilon_0^2}{e^4} \sum_{\alpha} \frac{Z_{\alpha}^{-2} n_{\alpha}}{\sum_{\beta} \left( Z_{\beta}^2 n_{\beta} \sqrt{\frac{2m_{\alpha}m_{\beta}}{m_{\alpha}+m_{\beta}}} \right)} \frac{T_i^{\frac{5}{2}}}{\ln \Lambda} \quad (2.11)$$

Above both classical thermal conductivity coefficients give the result in W / (m J).

- The parallel viscosity coefficient

$$\text{Simple plasma} \quad \eta_{\parallel} = 0.96 \frac{12\pi\sqrt{\pi}\epsilon_0^2 \sqrt{m_i}}{e^4} \frac{T_i^{\frac{5}{2}}}{Z_i^4 \ln \Lambda} \quad (2.12)$$

$$\text{Multiple ion species} \quad \eta_{\parallel} = 0.96 \frac{12\pi\sqrt{\pi}\epsilon_0^2}{e^4} \frac{Z_{\alpha}^{-2} n_{\alpha}}{\sum_{\beta} \left( n_{\beta} Z_{\beta}^2 \sqrt{\frac{2}{m_{\alpha}+m_{\beta}}} \right)} \frac{T_i^{\frac{5}{2}}}{\ln \Lambda} \quad (2.13)$$

The formula for parallel viscosity is given by Braginskii [32].

- Energy equipartition coefficient between ion and electron

Simple plasma

$$k = \frac{3 e^4 \sqrt{m_e} n_e Z \ln \Lambda}{2 \cdot 3 \sqrt{2 \pi \pi \epsilon_0^2} m_i T_i^{\frac{3}{2}}} \quad (2.14)$$

Multiple ion species

$$k = \frac{3 e^4 \sqrt{m_e}}{2 \cdot 3 \sqrt{2 \pi \pi \epsilon_0^2}} \left( \frac{Z_\alpha^2 n_\alpha}{m_\alpha} \right) \frac{n_e \ln \Lambda}{T_e^{\frac{3}{2}}} \quad (2.15)$$

The coulomb logarithm  $\ln \Lambda$  is a factor that is used to take account long range character of the coulomb collisions. The coulomb logarithm is presented below formula.

$$\ln \Lambda = 15.2 - 0.5 \ln \frac{n_e}{10^{20}} + \ln \frac{T_e}{1000} \quad (2.16)$$

For using the fluid approximation in this paper, the flux along with magnetic field line is not allowed to transgress the free streaming flux. Therefore, flux limits are used for electron thermal conductivity coefficient and the parallel viscosity coefficient. These flux limits are expressed below.

- Flux limit of the electron thermal conductivity and parallel viscosity coefficients.

$$\kappa_{||lim}^e = \kappa_{||SH}^e \left[ 1 + \left| \frac{q_{SH}}{q_{FL}} \right|^\gamma \right]^{-1}, \quad \eta_{||lim}^\alpha = \eta_{||}^\alpha \left| 1 + \frac{\eta_{||}^\alpha \frac{\partial u_{||\alpha}}{\partial x}}{\mu p_\alpha} \right|^{-1} \quad (2.17)$$

$\kappa_{||SH}^e$  is the classical Spitzer-Harm coefficient.  $\mu$  is a constant factor coefficient.

- As in tokamak experiments, the radial transport is considered to be anomalous in many cases also in the linear devices. Large uncertainty still exists for the anomalous transport coefficients. Therefore, we use Bohm scaling is used for particle transport. The diffusion coefficient in the radial direction, i.e., perpendicular to magnetic field line,

$$D_\perp = \frac{1}{16} \frac{T_e}{eB}. \quad (2.18)$$

Bohm diffusion coefficient is assumed as the diffusion coefficient.

- The perpendicular ion and electron thermal conductivity and viscosity coefficients are assumed by using Ref. 17. These radial transport coefficients should be assumed by the condition of GAMMA 10/PDX.

$$\kappa_\perp^i = 0.2 \times n_i, \quad \kappa_\perp^e = 4.0 \times n_e, \quad \eta_\perp = 0.2 \times m_i \times n_i. \quad (2.19)$$

## 2.3 The mesh structure

In the following simulations with the present code, the numerical meshes are created on the basis of GAMMA 10/PDX magnetic configuration. As mentioned above, in our present model, 2D model parallel and perpendicular to the magnetic field is employed under the assumption of axial symmetry. Therefore, the local curvilinear orthogonal coordinate system  $(x, y)$  has been employed instead of the usual cylindrical coordinate system  $(r, z)$ . The  $x$ -direction and  $y$ -direction in the local orthogonal coordinate system are corresponding, respectively, to the direction parallel and perpendicular to the magnetic field at each spatial point. The present model assumes the axial symmetry and 2D model in the  $x$  and  $y$  direction, while physical quantities are uniform in the  $\theta$  direction.

In Fig. 10 (a), the numerical mesh used in Chap. 4 with the coils and vacuum vessels in GAMMA 10/PDX geometry is shown. The detailed mesh structure is shown in Fig. 10 (b). These mesh structure is constructed from the GAMMA 10/PDX magnetic configuration in such a way that each cell becomes a rectangle shape with its sides being locally orthogonal each other. In addition, the tungsten target is designed at the end of the mesh structure.

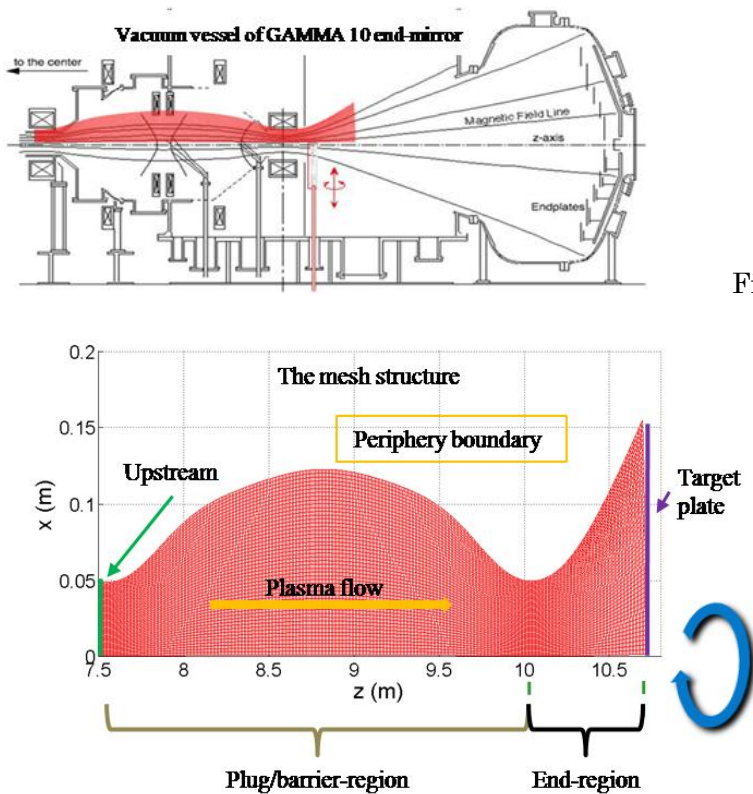


Fig. 10 (a) : The vacuum vessels of plug/barrier cell and end cell in the GAMMA 10/PDX and (b) : the detail mesh geometry. The tungsten target plate is installed at end of mesh.

The mesh structure is composed of quadrangular cells with  $0 \sim 15$  cm in the radial ( $x$  axis) direction and  $1004 \sim 1070$  cm or  $750 \sim 1070$  cm in the  $z$  axial direction. In GAMMA 10/PDX,

hydrogen plasma is mainly generated in the central-cell and flows out through the plug/barrier cell to the end-cell.

## 2.4 The boundary conditions

The plasma parameters at the main plasma upstream region on the most left-side of Fig. 8 are defined as fixed boundary ( Dirichlet condition ). Fixed boundary conditions at upstream region is shown below.

- Upstream boundary

$$\text{Ion density} \quad n_i = n_0 \left\{ \frac{r_0(0)}{r_0(z)} \right\}^2 e^{-\frac{1}{2} \left( \frac{r(z)}{r_0(z)} \right)^2} \quad (2.19)$$

$$\text{Ion temperature} \quad T_i = 100 \times e^{-\frac{1}{2} \left( \frac{r(z)}{r_0(z)} \right)^2} \quad (2.20)$$

$$\text{Electron temperate} \quad T_e = 30 \times e^{-\frac{1}{2} \left( \frac{r(z)}{r_0(z)} \right)^2} \quad (2.21)$$

where  $r_0$  indicats half maximum full-width of physical quantities,  $r(z)$  is spatial position of physical quantities and  $z$  is  $z$  axial position.

The divertor boundary condition in the ion and electron energy balance equations is defined by heat flux flowed into the target plate. For ion velocity along with magnetic field line, Bohn condition near the sheath entrance is adapted.  $\sigma$  represents ion and electron heat transfer coefficient.

- Divertor boundary

$$Q_i = \sigma_j n_\alpha T_j, (j = i, e) \quad (2.22)$$

$$u_{\parallel\alpha} \geq \sqrt{\frac{T_{i\alpha} + T_e}{m_\alpha}} \quad (2.23)$$

At the  $z$  axial, the boundary condition is defined as symmetry boundary because plasma is assumed as cylindrical configuration.

- $Z$  axial boundary

$$\frac{\partial n_\alpha}{\partial x} = \frac{\partial T_e}{\partial x} = \frac{\partial T_i}{\partial x} = \frac{\partial u_{\parallel\alpha}}{\partial x} = 0 \quad (2.24)$$

The periphery boundary is indicated as Neuman condition

- The periphery boundary condition

$$\frac{\partial T_{i\alpha}}{\partial x} = \frac{\partial T_e}{\partial x} = \frac{\partial n_{i\alpha}}{\partial x} = const \quad (2.25)$$

In this paper, Dirichlet boundary condition is imposed on the boundary in the radial direction with the fixed value, e.g., zero.

The distribution of neutral particle is given by analytical solutions of one dimensional continuity equation for neutrals under the condition of constant neutral velocity. The particle flux of neutral on the target is presented below.

$$n_{n,target} \cdot u_n = R_N \cdot \Gamma_{i,target} \quad (2.26)$$

$R_N$ : particle reflection coefficient,

$\Gamma_{i,target}$ : ion particle flux density on the target,

$u_n$ : neutral particle velocity,  $n_{n,target}$ : neutral density on the target.

Continuity equation of neutral particle is presented as follows,

$$\frac{\partial(n_n u_n)}{\partial x} = -n_n n_e \langle \sigma v \rangle \leftrightarrow n_n = n_{n,target} e^{-\left[\int \frac{dx}{\lambda}\right]} \quad (2.27)$$

$$\lambda = \frac{u_n}{n_e \langle \sigma v \rangle_{ei}} \quad (2.28)$$

where

$n_n$ : The neutral density,

$u_n$ : The neutral velocity,

$\langle \sigma v \rangle_{ei}$ : The rate coefficient of the electron-impact ionization.

## 2.6 Numerical scheme to solve the fluid equations

Basic equations Eqs. (2.1) - (2.5) are discretized and numerically solved almost in the same way as in Ref. [18]. In this section, the discretization method and numerical scheme to solved the resultant discretized algebraic equation are briefly summarized. We employed the finite-volume discretization method developed largely by S.V. Patanckar [33, 34]. In this method, discretization equation for each numerical cell ( control volume ) can be obtained by integrating the basic equation over the control volume. Therefore, in this method, it is easy to check the conservation property of

physical quantity in each cells, e.g., momentum conservation.

The resultant desretized equations for all cells can be expressed in the matrix form:

$$Ax = b \quad (2.29)$$

where A is the  $(N_g \times N_g)$  matrix, and x and b are, respectively, the vector of  $N_g$  unknown values and the given  $N_g$  sources. ( In the 2D modeling, the number becomes  $N_g = M \times N$ , where M and N are the number of cells in each direction ). More specifically, x is the unknown vector, whose element is corresponding to the solution of the basic equation at each grid point in the control volume. For example, if we discretize electron energy balance equation, each element of the vector x is corresponding to  $T_e$  at each spatial grid point.

In order to numerically solve the matrix equation above, " Stone's Strongly Implicit Procedure (SIP)" [35], has been used. The SIP scheme is classified into so-called the incomplete LU decomposition method. The iterative process is needed to obtain the solution, because basic equations are nonlinear equation for unknown variables.

The residual vector r in the i-th iteration process is defined as

$$r(i) = A x(i) - b \quad (2.30)$$

where x(i) is the numerical obtained in the i-th iteration processes.

$$dr = r(i + 1) - r(i) = A(x(i + 1) - x(i)) \quad (2.31)$$

Therefore, the difference in the residual dr becomes getting smaller, then the solution is getting closer to the convergent solution, i.e.,

$$x(i + 1) \geq x(i). \quad (2.32)$$

### 2.5.1 Characteristics of convergence in the numerical solutions

As mentioned above Section, the basic equations are calculated by using numerical scheme shown in Sec. 2.5. The boundary conditions are used as shown Sec. 2.4. Especially, ion and electron heat transfer coefficients are defined as 2.5 for ion and 4.0 for electron. The only west end-cell of GAMMA 10/PDX defined the range of region from 10.04 m to 10.70 m on z-axis is considered as the calculation area and the hydrogen ion plasma is considered.

A number of test calculations are executed. The calculation results is checked for validity and convergence. The validity of the calculation results has been established in Ref. [36]. This check of the validity of the calculation results is performed by comparing solutions between analytical result and calculation result and checking the preservative quality of all terms included equations. Therefore, the residual error of plasma parameters is used as an index of convergence. The definition of the residual error is indicated at the equation (3.1). The residual error of plasma parameter is shown in Fig. 11. Figure 11 shows the dependence which is the variations of plasma parameters during one calculation cycle on the iteration number as follows,

$$\Delta\tilde{\varphi} = \frac{\sum_i \sqrt{(\varphi^1 - \varphi^0)^2}}{\sum_i \varphi}, \quad (2.32)$$

where,

$\varphi$	Physical amount	$\varphi^0$	Physical amount of previous calculation step
$\varphi^1$	New defined physical amount	$\sum_i$	The summation in all meshes

In Figs. 11 (a) ~ (d), all residual errors of plasma parameters are convergence about  $10^{-14}$  after iteration number over 3500 despite the non-linear equations used in the fluid code. It is considered that the parameters calculated in the GAMMA 10/PDX mesh structure by using the fluid code becomes convergence.

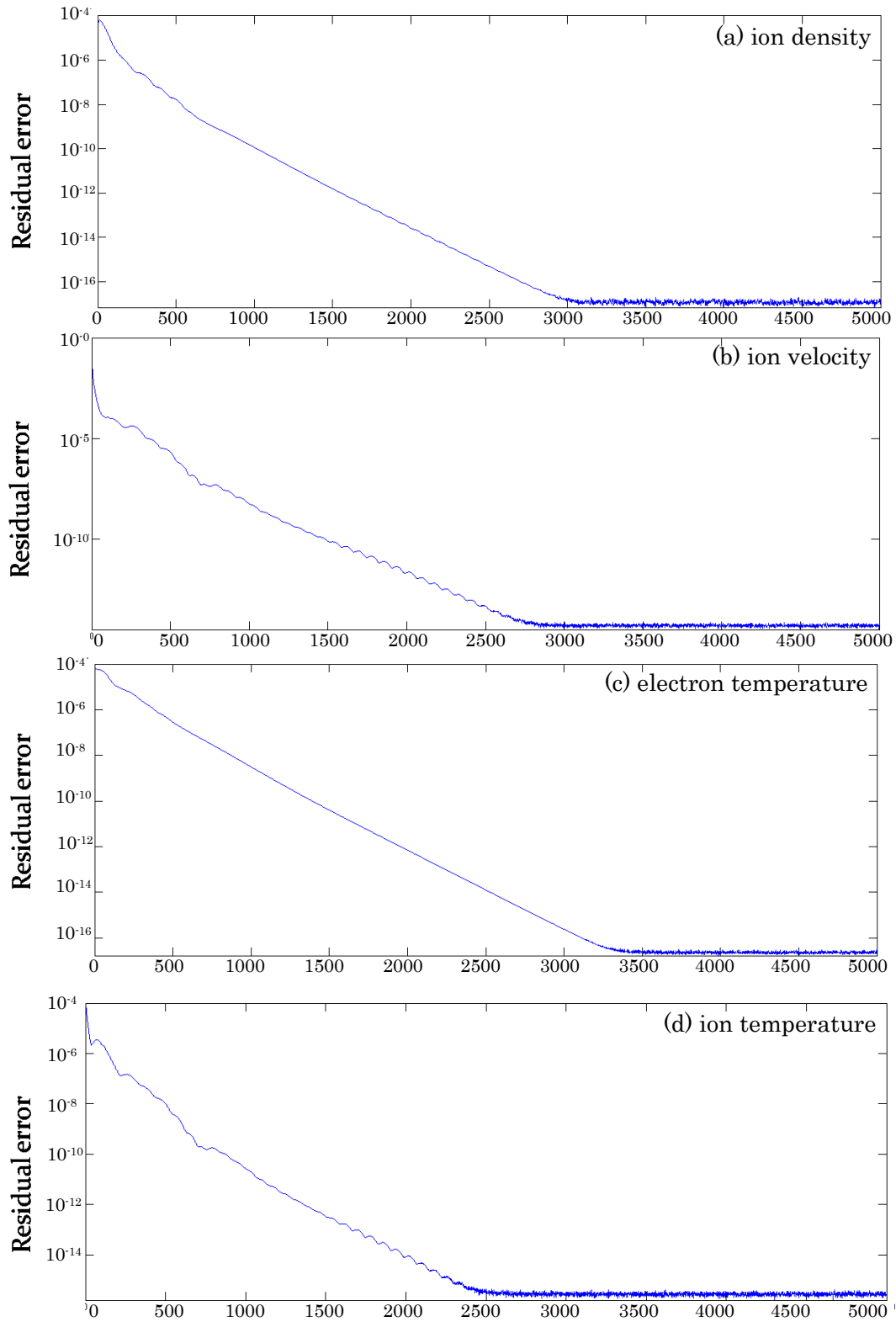


Fig. 11 (d) the residual error variation about iteration number (a): ion density,(b): ion velocity, (c): electron temperature and (d): ion temperature.

# Chapter 3

## Simulation result using single-fluid code

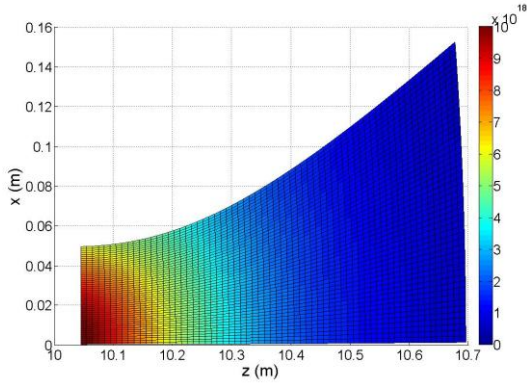
In this Chapter, we discuss the effect of (1) Magnetic flux expansion, (2) Neutral gas injection and (3) Impurity gas injection on the reduction of the heat load onto the divertor plate. The purpose of this chapter is to discuss and to obtain the basic understanding of these effects. For this purpose, further simplifications have been done with respect to the basic equations described in Chap. 2.

In Sec. 3.2.1, based on the simulation results for a relatively simple case, we first discuss the basic features of the end-loss plasma with the magnetic flux expansion in GAMMA 10/PDX. The effect of flux expansion will be discussed. Secondary, in Sec. 3.2.2, systematic comparisons have been made between cylindrical and expanded magnetic configuration in order to understand the effect of the magnetic flux expansion on the reduction of the heat and particle load onto the target plate. In Sec. 3.3, thirdly, the effect of neutral or impurity gas injection into end-loss plasma will be evaluated for obtaining the suggestions of decreasing plasma energy. In Sec. 3.3.2, axial distribution under condition of standard condition which means the typical plasma quantities in GAMMA 10/PDX end-loss plasma will be shown with hydrogen gas injection. In Sec. 3.3.3, the profile of electron temperature on the z-axis will be discussed. Finally, in Sec. 3.3.4, heat load and electron temperature on the z-axis with impurity injection will be described. In each sections, additional simplifications and or assumptions used in the analyses will be mentioned.

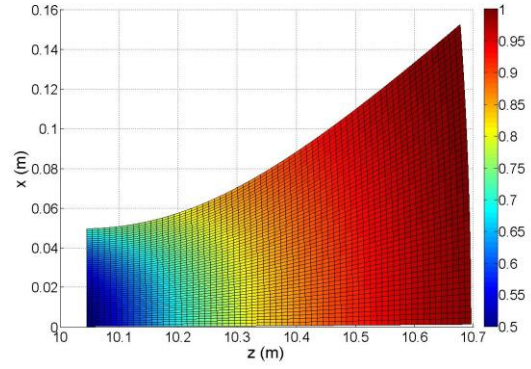
### 3.1 Characteristics of plasma in the GAMMA 10/PDX end-cell.

#### *3.1.1 The basic features of the end-loss plasma with the magnetic tube expansion in the GAMMA 10/PDX west end-cell.*

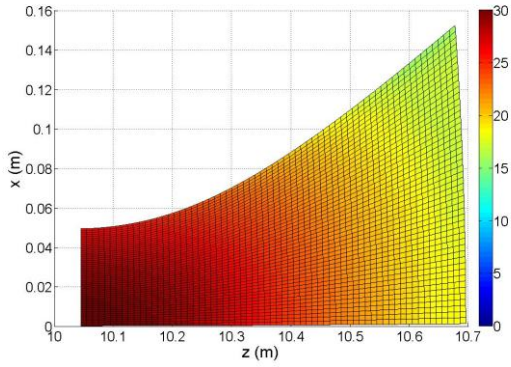
The characteristics of end-loss plasma at west end-cell in GAMMA 10/PDX had been partially investigated. However, the global images is not understood completely. For analyzing the effect of the flux expansion and characteristics in the west end cell, the fluid code is run without volume source terms. Therefore, the interactions between plasma and neutrals such as ionization, charge exchange and recombination are ignored in this section. The calculation results are shown in Fig. 12.



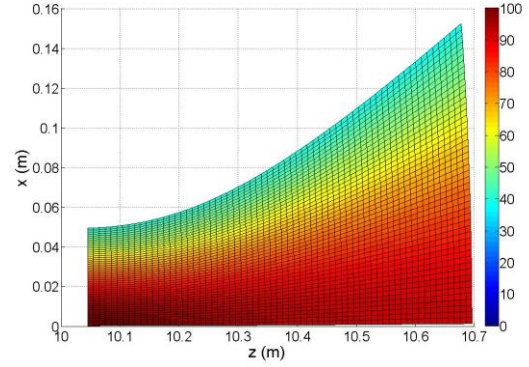
(a) Ion density



(b) Mach Number of ion flow



(c) Electron temperature



(d) Ion temperature

Fig. 12 Two dimensional distribution of plasma parameters, (a) ion density, (b) Mach number of ion flow, (c) electron temperature and (d) Ion temperature.

In Fig. 12 (a), ion density  $n_i$  decreases toward  $z$  axis and radial directions. The difference of ion density between at upstream and target plate becomes about 10 times. In the upstream region,  $n_i$  is  $\sim 10^{19} \text{ m}^{-3}$ . On the other hand,  $n_i$  becomes  $\sim 10^{18} \text{ m}^{-3}$  near the target plate. This result suggests that the distribution of  $n_i$  is influenced by the magnetic flux expansion as Fig. 9 in Chapter 1.

Calculated ion Mach number of ion flux shown in Fig. 12 (b) rises monotonically toward the target plate from 0.5 to 1. Ion flow satisfies Bohm conditions and accelerates toward the target plate. Mach number tends to become large toward the radial direction. This flow profile shows countertrend to the distribution of plasma density.

The distribution of electron temperature  $T_e$  is shown in Fig. 12 (c).  $T_e$  decreases with expanding magnetic field line. The electron temperature  $T_e$  varies from 30 eV at upstream to about 17 eV near the target plate on the  $z$  axis. The electron temperature  $T_e$  decreases without interaction between electron and neutral particles, because it is easy for the energy of electron to transfer along with

magnetic field line due to the large parallel thermal conductivity of electron and the electron pressure-driven flow effect. The pressure driven force and the electrostatic force on the electrons must be closely balanced in the small mass limit ( $m_e \Rightarrow 0$ ) without collisional drag force. This situation leads to the Boltzmann relation [37]. On the other hand, ion temperature  $T_i$  near the target plate has little difference from the value of upstream in Fig. 12 (d). Moreover, the profile in the radial direction also has little change in the calculation area as same as  $T_e$ . These features of  $T_e$  and  $T_i$  are obtained from the numerical simulations of the end loss plasma in the GAMMA 10/PDX. Especially, such non-equilibrating feature of  $T_e$  and  $T_i$  is similar to that in the low density upstream SOL and/or low recycling divertor plasma in the attached state (in tokamak).

From above simulation results of the end loss plasma in the west end-cell region of the GAMMA 10/PDX with the magnetic flux expansion, the end loss plasma has the following features;

- Plasma pressure and density is lower toward the target plate.
  - Under the condition without volume source terms, heat and particle fluxes on the target plate decrease.
- The distribution of ion and electron temperatures in the end-cell of the GAMMA 10/PDX has a property similar to the upstream SOL plasma and/or low recycling divertor plasma in tokamaks.
- Ion and electron temperatures,  $T_i$  and  $T_e$  are not equilibrating with each other.
- The plasma flow is accelerated at the point of end-cell away from the target plate in the GAMMA 10/PDX

### 3.1.2 The systematic comparison between cylindrical and expanded magnetic configuration.

Plasma behavior near the target plate is influenced by the magnetic configuration. From this fact, the effect of divertor magnetic configuration is investigated mainly for reduction of heat load toward the target plate.

For understanding such effects by the magnetic structure, comparison between cylindrical geometry without the magnetic flux expansion and expanding geometry with the magnetic flux expansion is performed. In the cylindrical geometry, the magnetic field is uniform in space and its strength is taken as the same value at the end-mirror throat coil ( $B = 3.0$  T). The expanding geometry, on the other hand, has the same magnetic field configuration as in the west end-cell of GAMMA 10/PDX which has been used in the horn-like geometry. The mesh structure produce for the later magnetic configuration (horn-like configuration) is shown in Fig. 13 (a), while it is shown in Fig. 13 (b) for the cylindrical configuration without the flux expansion.

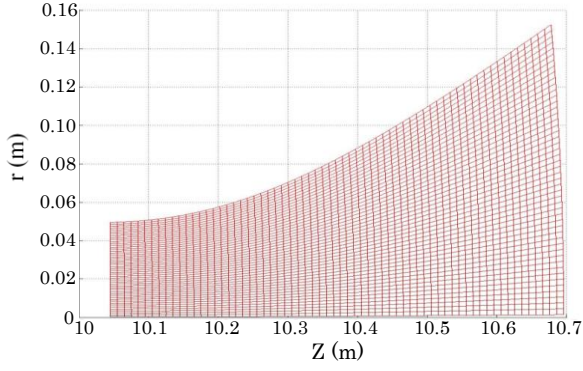
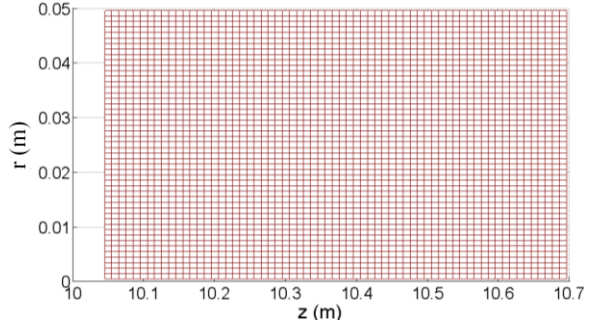


Fig. 13 (a) : The expansion mesh,



(b) : The cylindrical mesh

In both configurations, the numerical domain is extended with a same system length  $L_z = 0.7$  m in the  $z$  direction on the  $z$ -axis ( $r = 0$ ). The radial extent of the mesh for each configuration is different. In the cylindrical configuration, the radial extent  $L_r$  is fixed as  $L_r = 0.05$  m, while it depends on the axial  $z$  position in the horn-like configuration with the flux expansion as shown in Fig. 13 (a). The difference of the volume between horn-like configuration with the flux expansion and the cylindrical configuration is calculated to be

$$\frac{V_{\text{cylind}}}{V_{\text{Expansion}}} \approx 0.25 . \quad (3.1)$$

The ratio of the total area perpendicular to the magnetic field at the end of numerical domain ( the right-hand-side boundary in Fig. 13 ) at the end of mesh between the two configurations is evaluated as

$$\frac{A_{\text{div}}^{\text{cylind}}}{A_{\text{div}}^{\text{Expansion}}} \approx 0.104 . \quad (3.2)$$

The boundary condition of  $n_i$  at the upstream boundary is defined as  $n_0 = 1.0 \times 10^{19} \text{ m}^{-3}$ . The value of gradient in the radial boundary is defined as 0. The axial distribution of neutral density is given by recycling neutrals at the target plate. The calculation results of different two magnetic configurations are shown in Fig. 14.

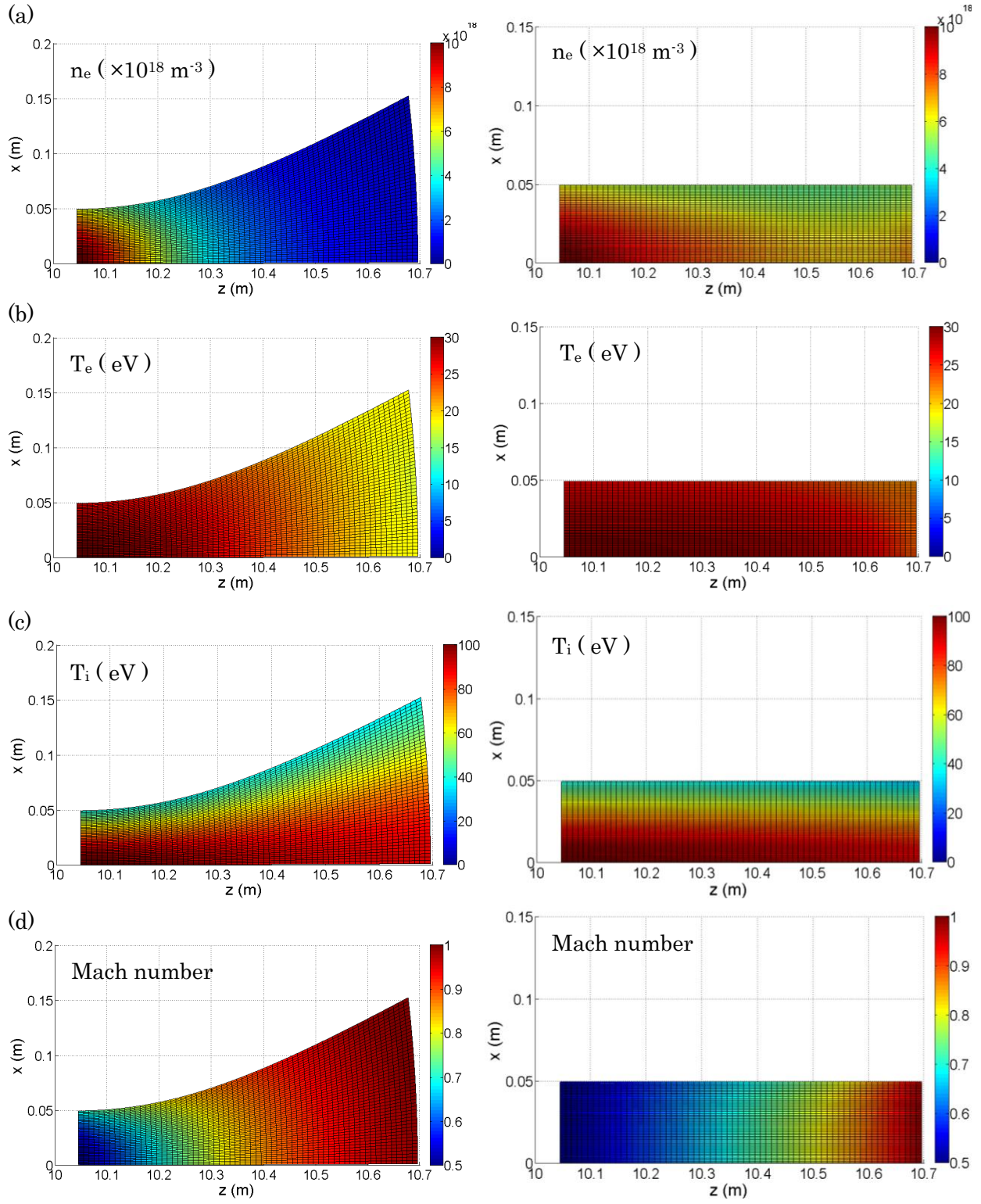


Fig. 14 The two-dimensional distribution of plasma parameters in expanded and cylindrical configurations. (a) : Plasma density, (b) : electron temperature, (c) : ion temperature and (d) : Mach number.

In Fig. 14 (a), the distribution of plasma density in case of ( horn-like ) expanding configuration and cylindrical configuration are shown. The range of plasma density is  $10^{17} \sim 10^{19} \text{ m}^{-3}$  in the expansion configuration. While in the cylindrical configuration, the range of plasma density becomes from  $10^{18} \sim 10^{19} \text{ m}^{-3}$ . The difference in plasma density between expanding and cylindrical configurations reaches about 10 times. It should be noted that a density peak appears in front of the target plate in the cylindrical configuration without the magnetic flux expansion. As will be discussed more in detail below, the ionization source increases by recycling neutral particles. In this cylindrical configuration, the ion flux density to the target plate becomes larger without flux expansion. Therefore, recycling neutrals and the resultant ionization source becomes also larger than the expanding configuration, which produce the peak of the electron density in front of the target plate in the cylindrical configuration.

The distribution of  $T_e$  is shown in Fig. 14 (b). The electron temperature  $T_e$  varies slightly near the target plate in the case of cylindrical configuration. As shown in Fig. 14 (a),  $T_e$  in the cylindrical configuration becomes higher than in expansion configuration. The distribution of  $T_e$  in the cylindrical configuration does not monotonically decrease like  $T_e$  in the expanding configuration. These results suggests the effect of expanding configuration because the heat flux density per unit area is larger in the cylindrical configuration compared with heat flux density per unit area in the expanding configuration.

Fig. 14 (c) shows the distribution of  $T_i$ . Near the target plate,  $T_i$  in the cylindrical configuration tends to be low slightly than  $T_i$  in the expansion configuration. In addition, the region decreasing  $T_i$  near the target plate in the cylindrical configuration is broader than in the expanded configuration. However, the distribution of  $T_i$  does not have so much difference between the two configurations.

Finally, ion Mach number is shown in Fig. 14 (d) under the different two configurations. Both behaviors of Mach number is similar in the sense that they are increasing toward the target plate from 0.5 to approximately 1. However Mach number in the expanding configuration begins to increase around  $z = 10.3 \text{ m}$ , Mach number in the cylindrical configuration starts rising in more upstream region at nearly  $z = 10.5 \text{ m}$ . The dependence on the radial direction under the cylindrical configuration is weaker than under the expanding configuration.

Not only the distribution of plasma parameters but also the volume source terms are influenced by the magnetic structures. Figure 15 shows the neutral particle density distribution as (a), the particle volume source as (b) and the momentum volume source as (c).

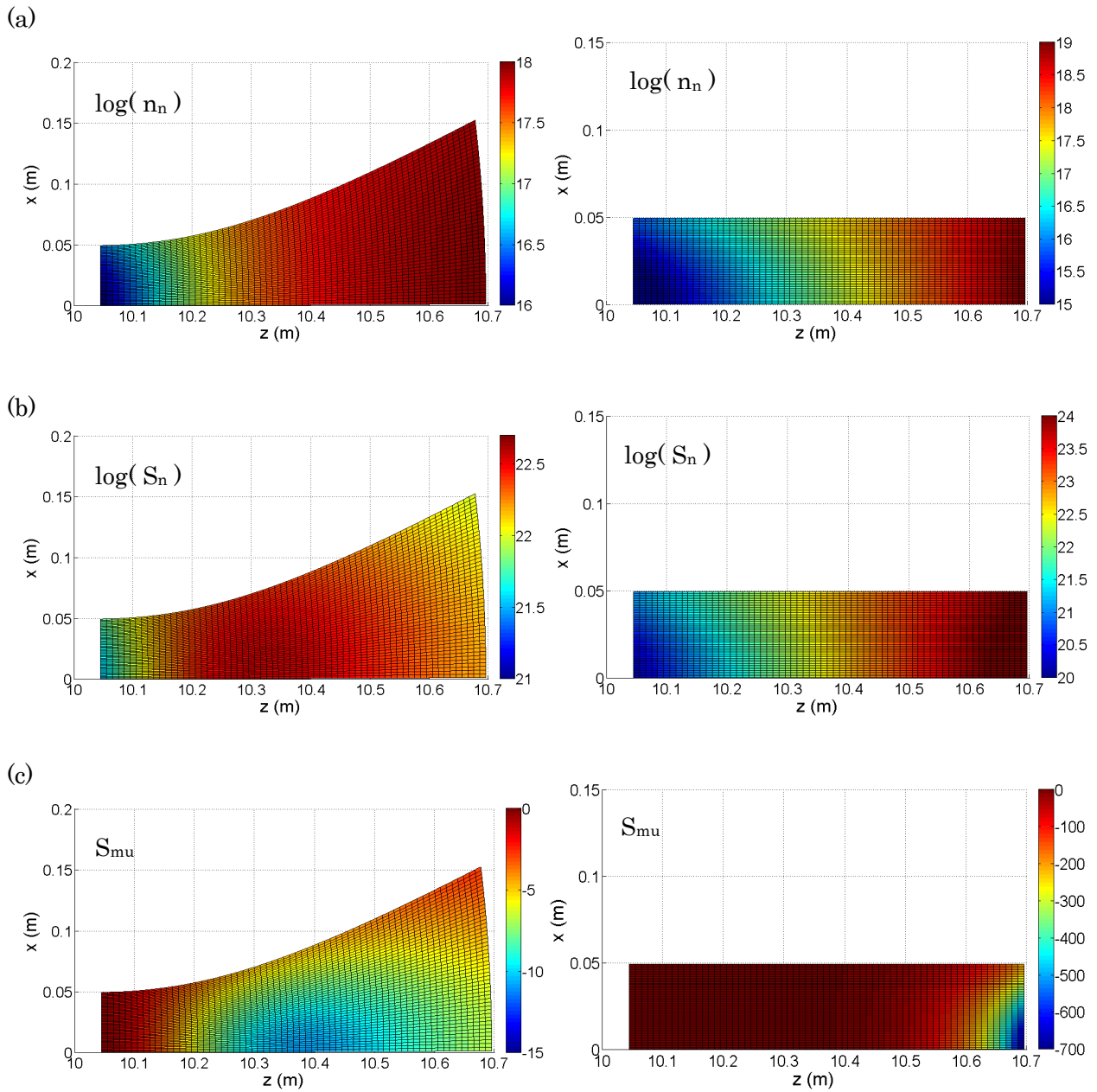


Fig. 15 2-D. distribution of the volume sources and the neutral particle density in the expanding configuration and cylindrical configuration. (a) : The distribution of neutral particle density, (b) : The volume source for particle and (c) : the volume loss for the momentum.

The distribution of the neutral density is shown in Fig.15 (a). The distribution of neutral density in the cylindrical configuration is localized compared with in the expanding configuration. The neutral density in the cylindrical configuration is distributed within the range of  $10^{15} \sim 10^{19} \text{ m}^{-3}$ . In the expanding configuration, the distribution of neutral density falls in the range of  $10^{16} \sim 10^{18} \text{ m}^{-3}$ . The neutral distribution is calculated by Eq. (2.27) in Cap. 2. The recycling neutral density at the target plate becomes large with increasing the ion flux reached the target plate. Therefore, the neutral density in the cylindrical magnetic configuration is larger than in the expanded magnetic configuration. In Fig. 15 (b), the position of the maximum particle volume source is located about  $z = 10.3 \sim 10.4 \text{ m}$  in case of expanding configuration. On the other hand, the position where the particle volume source take its maximum value exists near the target plate. In addition, the position where the particle volume source take its maximum value in the expanding configuration and in the cylindrical configuration shown in Fig. 15 (c). The peak point of ion density appears where the particle volume source has the maximum value in both configurations. The volume sources relate to neutral and electron density or electron temperature. In this condition, the rate coefficient of hydrogen ionization keeps almost the same value because  $T_e$  does not change largely. Therefore, the difference of the points where the volume source takes its maximum and/or minimum value is almost determined by the distribution of plasma and neutral particles. In cylindrical configuration, the peak point of plasma density and neutral density is produced near the target plate. On the other hand, in case of expanding configuration, the distribution of neutral density has a peak near the target plate, however the peak of the ion density occurs in the upstream region.

In addition, the effects of the magnetic flux expansion on heat load and particle flux on the target plate are studied. In Fig. 16 (a), (b) and (c), the radial distribution of heat and particle fluxes and heat and particle flux on the target plate are shown.

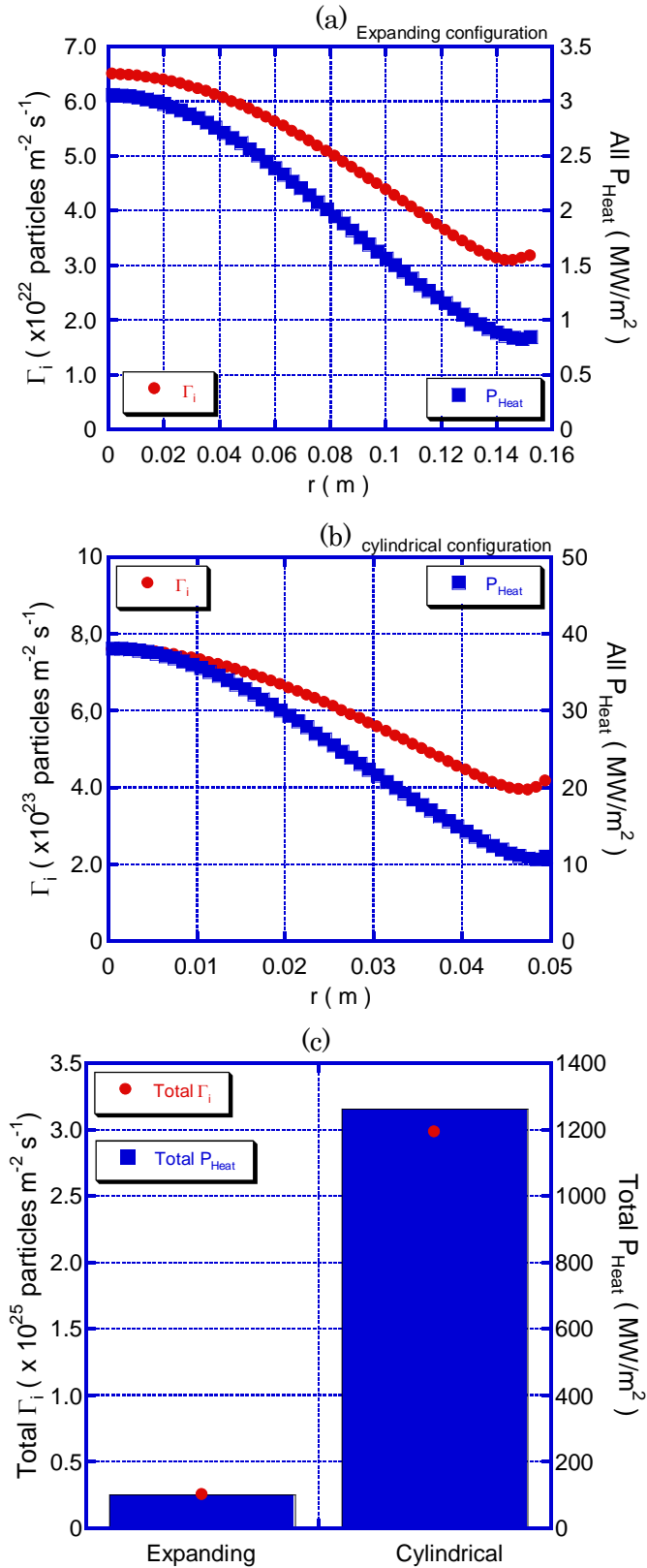


Fig. 16 The radial distribution of heat flux on the target plate ( $z = 10.70$  m) at the red line and particle flux at the blue line. (a) : the expanding configuration, (b) : the cylindrical configuration and (c) : total heat and particle fluxes on the target plate.

Figures 16 (a) and (b) show the distribution of heat and particle fluxes at  $z = 10.70$  m in cases of expanding configuration and cylindrical configuration, respectively. The radial distribution profiles in the both magnetic field line is similar to each other. Only the value of heat and particle fluxes is different. In Fig. 15 (c), all heat and particle fluxes reached target plate are indicated. The rate of heat and particle fluxes between expansion and cylindrical mesh is shown below,

$$\frac{P_{Heat}^{cylind}}{P_{Heat}^{Expansion}} \approx 12, \quad \frac{\Gamma_i^{cylind}}{\Gamma_i^{Expansion}} \approx 10 . \quad (3.3)$$

The rate of the heat and particle fluxes between two meshes roughly depends on the inverse of the area at the target plate. Heat and particle fluxes in the cylindrical mesh is ten times larger than in the expansion mesh.

This calculation results are checked by analytical solution in case of expanding configuration. Therefore, the momentum equation is intergraded from the inlet to the target plate without volume source term.

$$\begin{aligned} \int dx dy \left[ \frac{\partial}{\partial x} \{n(m_i u_{\parallel}^2 + 2T)\} + \frac{\partial}{\partial y} \{n(m_i u_{\parallel}^2 + 2T)\} \right] &= 0 \\ \Leftrightarrow [n(m_i u_{\parallel}^2 + 2T)]_{A_e} - [n(m_i u_{\parallel}^2 + 2T)]_{A_w} + [n(m_i u_{\parallel}^2 + 2T)]_{A_n} - [n(m_i u_{\parallel}^2 + 2T)]_{A_s} &= 0 \\ &= 0 \\ \Leftrightarrow [n(m_i u_{\parallel}^2 + 2T)]_{A_e} - [n(m_i u_{\parallel}^2 + 2T)]_{A_w} &= 0 \quad \because A_n \approx A_s \end{aligned} \quad (3.4)$$

By adding assumption  $A_e / A_w \approx 10.43$  then,

$$\begin{aligned} 10.43 \times [2n_d T_d (1 + M_d^2)] - 2n_0 T_0 (1 + M_0^2) &= 0 \\ \Leftrightarrow 10.43 \times [2n_d T_d (1 + M_d^2)] - 2n_0 T_0 (1 + M_0^2) &= 0 \Leftrightarrow 41.72 n_d T_d - \frac{5}{2} n_0 T_0 = 0 \\ \Leftrightarrow n_0 T_0 = 16.68 n_d T_d \quad \because M_d &= \sqrt{\frac{2T}{m_i}} \end{aligned} \quad (3.5)$$

Here, the index "0" means the parameters at the west mirror throat and the index "d" indicates the parameters on the target plate. In the calculation results,  $n_0 T_0 \approx 3.0 \times 10^{20} \text{ m}^{-3} \text{ eV}$ ,  $n_d T_d \approx 1.08 \times 10^{19} \text{ m}^{-3} \text{ eV}$ . Therefore, analytical result is roughly consistent with the calculation result.

From above results, the present modeling or code is useful to understand the basic effects of the magnetic flux expansion. Also, it is shown that the flux expansion in the west end-cell region of the GAMMA 10/PDX is effective to reduce the heat and particle load towards the target plate.

## 3.3 Injection of neutral or impurity gas into the end-cell using the single code

### *3.3.1 Reducing plasma energy by injecting neutral or impurity gas into plasma*

Injecting neutral or impurity gases into the edge plasma is useful to reduce particle and heat load toward the target plate. However, it is concerned that neutral and/or impurity injection lead to the degradation of the plasma energy confinement due to the impurity radiation if they are penetrating into the core plasma region. Therefore, it is important to evaluate the effects of neutral or impurity injection.

In this section, argon ( Ar ) is considered as impurity and hydrogen atom is defined as injected neutral particle. In this section, the effects of Ar impurities are taken into account in the following manner;

- (1) Eqs. (2.1), (2.2) and (2.3) has been solved in the trace impurity limit, i.e., these equation has been solved only for the fuel hydrogen ion species.
- (2) The Ar impurity density  $n_z$  is taken as parameter.
- (3) Only the effect of the radiation cooling effect by the Ar impurity is taken into account in Eq. (2.4) as an energy loss term,
- (4) The radiation function for Ar is used by shown Fig. 16 [38].

As for the hydrogen neutrals, molecular processes are not taken into account, only the reaction processes related to the atomic hydrogen are included in the analysis such as ionization, charge-exchange reaction and plasma recombination. In addition, sheath heat transmission factors in Eq. (2.4) and (2.5) are assumed at 2.5 and 4.0 for ions and electrons under the same value with the previous section.

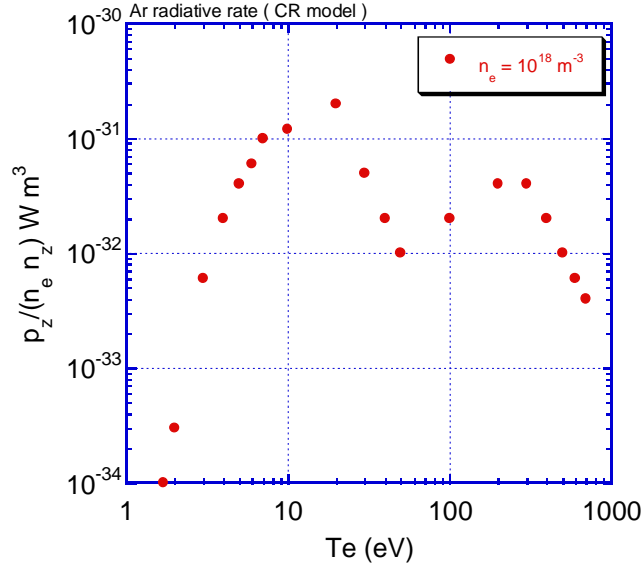


Fig. 16 The radiation rate for argon

### 3.3.2 Axial distribution in standard condition

The condition of simulation are shown in Table 1. The symbols  $T_{i0}$  and  $T_{e0}$  are the ion and electron temperature, respectively, at the entrance ( $z = 10.4$  m) of the numerical domain on the  $z$ -axis. The symbol  $\Delta n_{0in}$  is the additional neutral particle density to simulate the neutral and impurity injection, which is given uniformly in the calculation area. Figure 17 shows the  $z$ -axial distribution of (a) electron temperature, (b) ion temperature and (c) plasma density obtained from the simulation. In all cases, the electron temperatures decrease toward the target plate. In the cases of (C) and (D) of higher additional neutral particle density, the electron temperatures decrease more strongly compared with the cases with lower  $\Delta n_{0in}$  (case (A) and (B)). The electron temperature reduces to about 9 eV in the case of (D). The ion temperatures decrease toward target plate similarly as electron temperature in all cases. However, decreasing the amount of ion temperature is small ( $\sim 10$  eV). As shown in Fig. 17 (c), plasma density decreases along with the expansion of the magnetic flux tube in all cases. As increasing additional neutral hydrogen particle density, the plasma density builds up and the peak of plasma density moves from the entrance toward the target plate. The plasma density peaks at 10.1 m and reaches about  $1.12 \times 10^{19} \text{ m}^{-3}$  in the case of (D).

In Fig. 18, calculation results in front of the target ( $z = 10.7$  m) are plotted as a function of the peak plasma density on the  $z$ -axis. As shown in Fig. 18 (a), the decrease in electron temperature by about 10 eV is observed, with increasing in the peak plasma density. However, it should be noted that the reduction of  $T_e$  is not so drastic and almost saturated for higher peak density case ( $n_i > 1.06 \times 10^{19} \text{ m}^{-3}$ ). In Figs. 18 (b) and (c), on the other hand, particle and heat fluxes increase with

building up plasma density. The particle flux in front of target plate is increasing from  $6.0 \times 10^{22}$  to  $1.8 \times 10^{23}$  particle/m<sup>2</sup> s. Heat flux on the target also increases with the peak plasma density from 3 to 7 MW/m<sup>2</sup>.

From above results, under the relatively simple model in this section, the effect of neutral injection on the reduction of the electron temperature  $T_e$  is not large and  $T_e$  is almost saturated at  $T_e \sim 10$  eV. For this relatively large  $T_e$  regime, ionization rate coefficient is still high and the end-cell plasma cannot reach the detachment state and it is still in the high recycling state. Therefore, the ion flux towards the target plate enhances due to high neutral recycling. It might be also worth noting that the large temperature difference between  $T_e$  and  $T_i$  ( $T_i \gg T_e$ ), and the resultant energy transfer from the ion channel to the electron channel prevents the electron temperatures from decreasing to such low temperature. Although, the simple model consideration given in this section is useful for obtaining the basic understanding of the effects of neutral injection, more self-consistent modeling of neutrals including neutral transport effect will be needed. The effect will be discussed in Chap. 5.

Table 1 Condition of numerical simulation

Case	(A)	(B)	(C)	(D)
$T_{i0}$ (eV)	100	100	100	100
$T_{e0}$ (eV)	30	30	30	30
$\Delta n_{0in}$ (m <sup>-3</sup> )	$1.0 \times 10^{17}$	$1.0 \times 10^{18}$	$4.0 \times 10^{18}$	$6.0 \times 10^{18}$

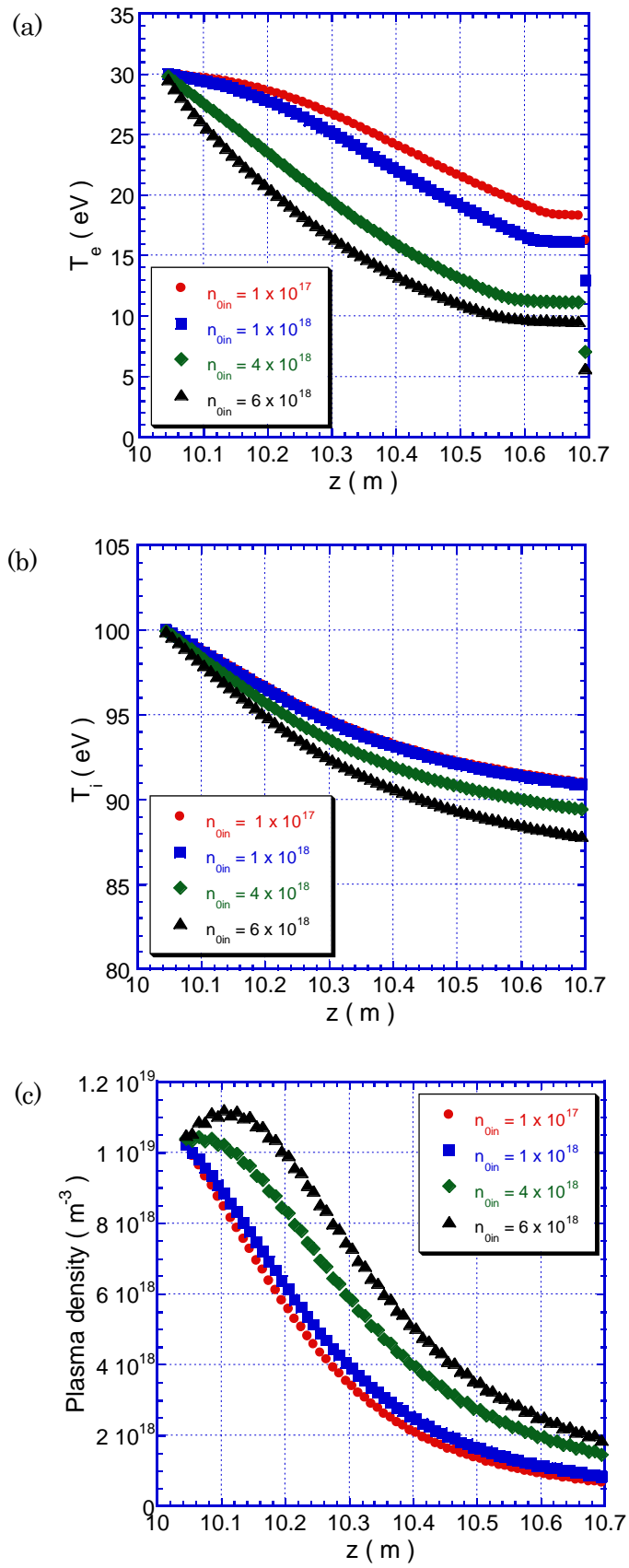


Fig. 17 Axial profile of the plasma parameters on the  $z$ -axis ( $r = 0$ ) in the case of hydrogen neutral injection. (a)  $T_e$ , (b)  $T_i$  and (c)  $n_i$ .

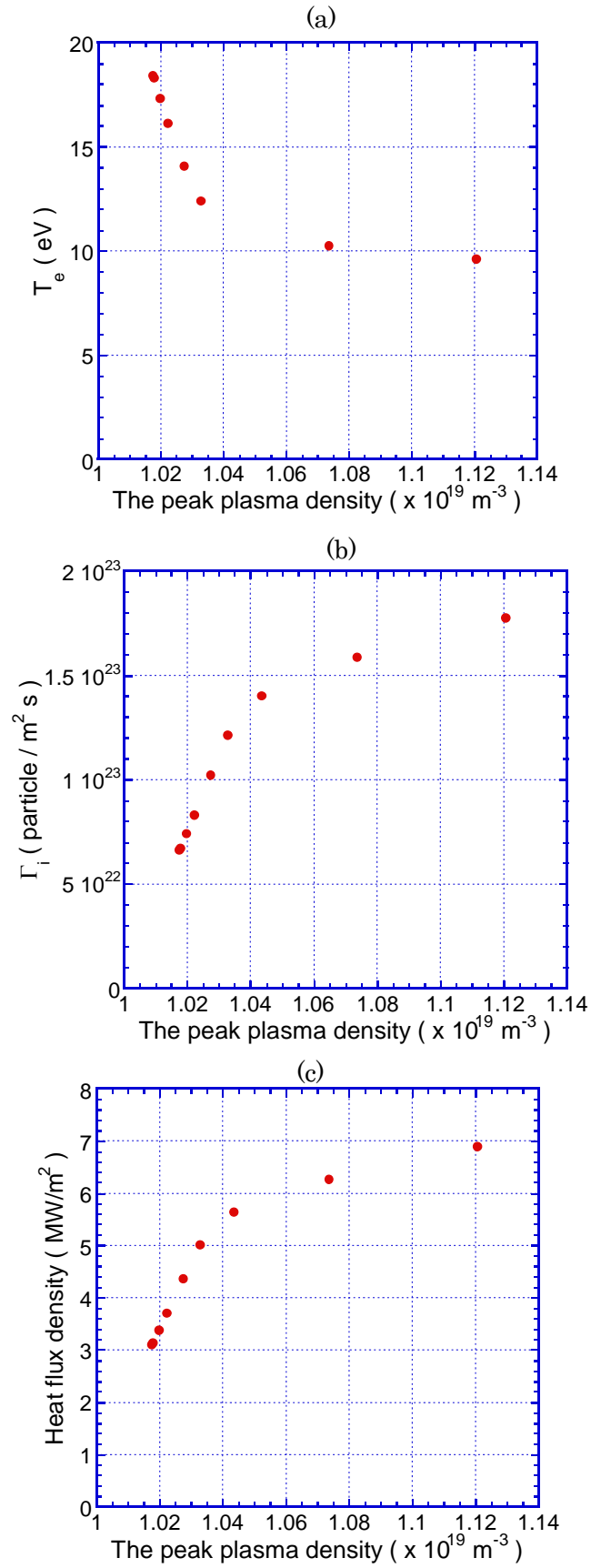


Fig. 18 Dependence of calculated plasma parameters on the upstream ion density. (a) electron temperature  $T_e$ , (b) ion temperature  $T_i$  and (c) heat flux density.

### 3.3.3 Effects of additional neutral hydrogen in low temperature condition.

Figure 19 shows the dependence of electron temperature and the upstream plasma density on additional neutral density in different ion temperature. The conditions of ion and electron temperatures and additional hydrogen neutrals are defined shown in Table 2. Ion temperature is changed at 10 eV, 30 eV and 100 eV. Circle symbols represent the case of 10 eV. Square symbols show 30 eV and diamond shape symbols are corresponding to the case with 100 eV. As decreasing ion temperature, electron temperature reaches lower temperature region and peak plasma density begins to increase at low additional neutral density. Especially, in the case of ion temperature with 10 eV, electron temperature is reduced to nearly 3 eV and the upstream plasma density increases to  $1.1 \times 10^{20} \text{ m}^{-3}$ . It is possible for the ions to lose their momentum by the collisions with neutrals, e.g., charge exchange and/or to dissipate their momentum by viscosity. Therefore, if ion flow velocity becomes small due to above mechanisms, then it seems that plasma density can become large in the calculation for satisfying continuity equation. Heat flux decreases with the increasing upstream plasma density. This tendency is different from the case where the ion temperature is relatively high ( $T_i > 30 \text{ eV}$ ). Under the high ion temperature condition, the collisional energy transfers from the ion to the electron becomes dominant. However, the direction of energy transfer between ion and electron becomes opposite. In addition, the effect of charge-exchange reaction seems to be small because the rate of charge exchange reaction does not large change in the range from ion temperature  $T_i$  100 eV to 10 eV. It seemed that the reduction of heat load on the target plate is enhanced by increasing the energy loss of electron and ion under the low  $T_i$  condition.

Table 2. The conditions of initial  $T_i$ ,  $T_e$  and additional hydrogen neutral density in the simultaneous domain.

Case	(A)	(B)	(C)
$T_i$ (eV)	100	30	10
$T_e$ (eV)	30	30	30
$\Delta n_{0in}$ ( $m^{-3}$ )	$\sim 5.0 \times 10^{18}$	$\sim 3.0 \times 10^{18}$	$\sim 4.0 \times 10^{18}$

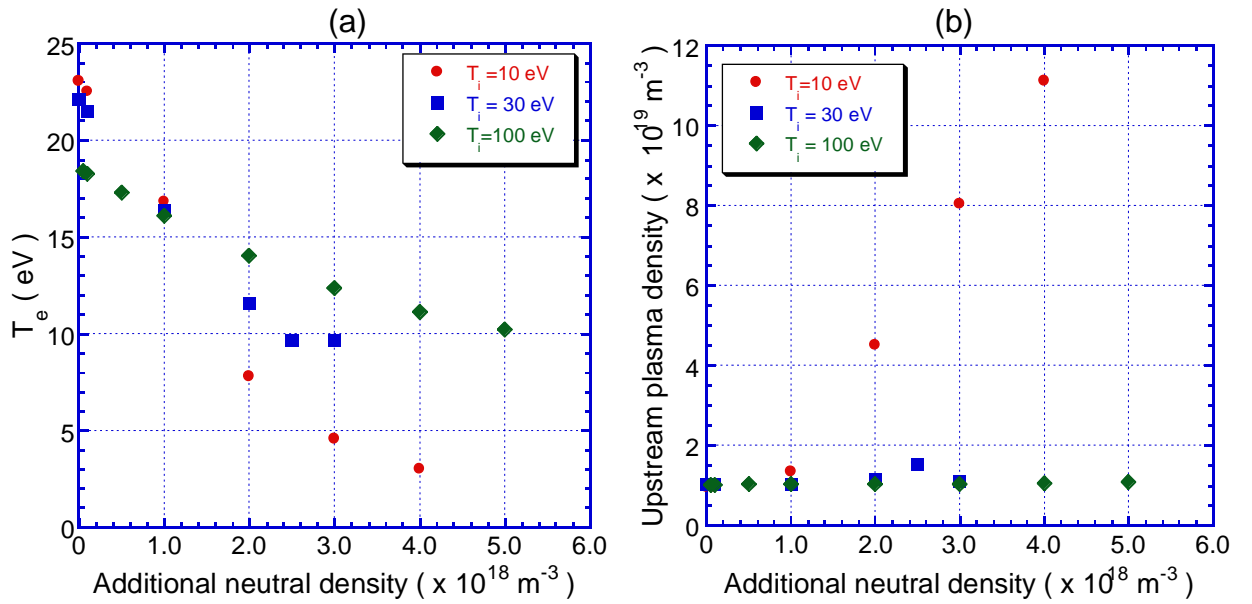


Fig. 19  $T_e$  (a) and upstream plasma density (b) dependence on additional neutral density.

### 3.3.4 Effects of impurity gas

Heat flux and electron temperature dependences on the upstream density are shown in Fig. 20. Heat flux on the target plate has the large value at the upstream density of  $\sim 1.3 \times 10^{19} \text{ m}^{-3}$  and gradually decreases with the density. Square and triangle symbols represent the results of Ar gas injection. Encircled symbols with solid circle correspond to the result that Ar atoms are uniformly filled in the numerical domain with the same density of additional neutral hydrogen density ( $3.0 \times 10^{18} \text{ m}^{-3}$ ). On the other hand, the symbols surrounded by dashed circle represent the results under the condition of Ar atoms supplied with the density of  $5.0 \times 10^{18} \text{ m}^{-3}$  together with the background neutral hydrogen density of  $2.0 \times 10^{18} \text{ m}^{-3}$ . In the case of Ar gas injection, heat flux and electron temperature are obviously reduced. However, it is shown that the upstream plasma density is also reduced. The degree of heat flux reduction almost corresponds to the reduction rate of the upstream plasma density. The above results imply that the electron temperature reduction due to the enhancement of radiation cooling induces suppression of ionization in upstream region. More detailed plasma parameter survey is needed for obtaining the optimum condition of radiation cooling toward the realization of steady detachment plasma condition.

Behavior of background plasma of divertor simulation experiments in the GAMMA 10/PDX west end-cell is calculated by using a fluid code. In the condition of high ion temperature and without Ar gas, plasma parameters do not decrease sufficiently. However, in low ion temperature circumstance, remarkable increase of upstream plasma density and reduction of the electron temperature on the target is clearly observed. In the case of Ar gas injection, significant reduction of both electron temperature and heat flux onto the target is achieved, which indicates the enhancement of radiation cooling.

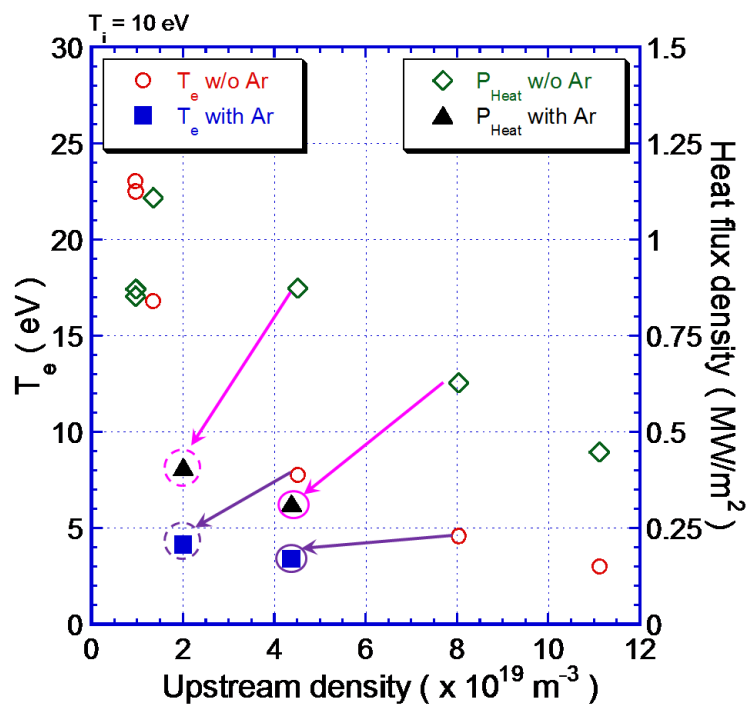


Fig. 20 Electron temperature and heat flux dependences on the upstream plasma density.

# Chapter 4

## Simulation results with the extended numerical domain and multi-fluids modeling

In the previous chapter 3, the effects of impurity or neutral injection are estimated by using single fluid code. However, The following four important points are not included in the model:

- (1) In the previous section, the numerical domain was limited in the end cell. This makes it difficult to set the upstream boundary condition at the entrance of the cell, because i) in GAMMA 10/PDX, the plasma flows from central cell through plug/barrier cell to the end cell and ii) some amount of neutral and/or impurity gas injected into the end-cell region possibly flow out of the end-cell region.
- (2) The variation of electron density due to ionization of impurity gas is not considered in this model.
- (3) Impurity density profile was fixed and effects of the impurity transport towards the upstream region was not included in the model.
- (4) Finally, the effects of impurity ion such as friction and energy transport between another species ions are ignored.

It is important for end-loss plasma in GAMMA 10/PDX to include these effects into the fluid model because these effects are important for more self-consistent simulation and also archiving reduction of heat load or particle flux by reducing ion temperature from the results of previous section. Therefore, above effects are included for elucidating the more detail plasma behaviors. In section 4.1.1, the mesh extended from plug/barrier cell to end cell is explained. In next section 4.1.2, the detail of additional terms and assumptions in multi-fluid code are indicated.

### 4.1 The extension of the mesh structure and multi-fluid code

#### *4.1.1 The expansion of mesh from plug/barrier cell to end cell*

As mentioned above, in GAMMA 10/PDX, the plasma flows from central cell through plug/barrier cell to the end cell. On the other hand, recycling hydrogen neutrals and also injected neutral hydrogen and impurity gas are transported toward the central region through the plug/barrier cell region. Therefore, it is better to extend the computational domain towards the upstream and this

would make it possible to impose more reasonable boundary condition on the upstream boundary.

In Fig. 4.1, the numerical meshes for the extended domain is shown. As seen from Fig. 4.1, the extended numerical domain includes the plug/barrier cell. It is extended toward the central cell up to the  $z$ -coordinate  $z = 2.4$  m. By this extension, the back-flow of impurity ion can be traced and the variations of the influx plasma parameter around the entrance of end-cell can be reasonably modeled.

In Figs. 21 (a), (b), (c) and (d), the typical distributions of end-loss plasma are shown. Figure. 21 (a) shows the distribution of hydrogen ion density as (a), the distribution ion and electron temperate are shown, respectively, in (b) and (c). Finally the Mach number. in the calculation domain is shown in (d). Also, the  $z$ -axial profiles of hydrogen ion density (a),  $T_i$  and  $T_e$  (b) and ion Mach number (c) are shown in Figs. 22 (a), (b) and (c).

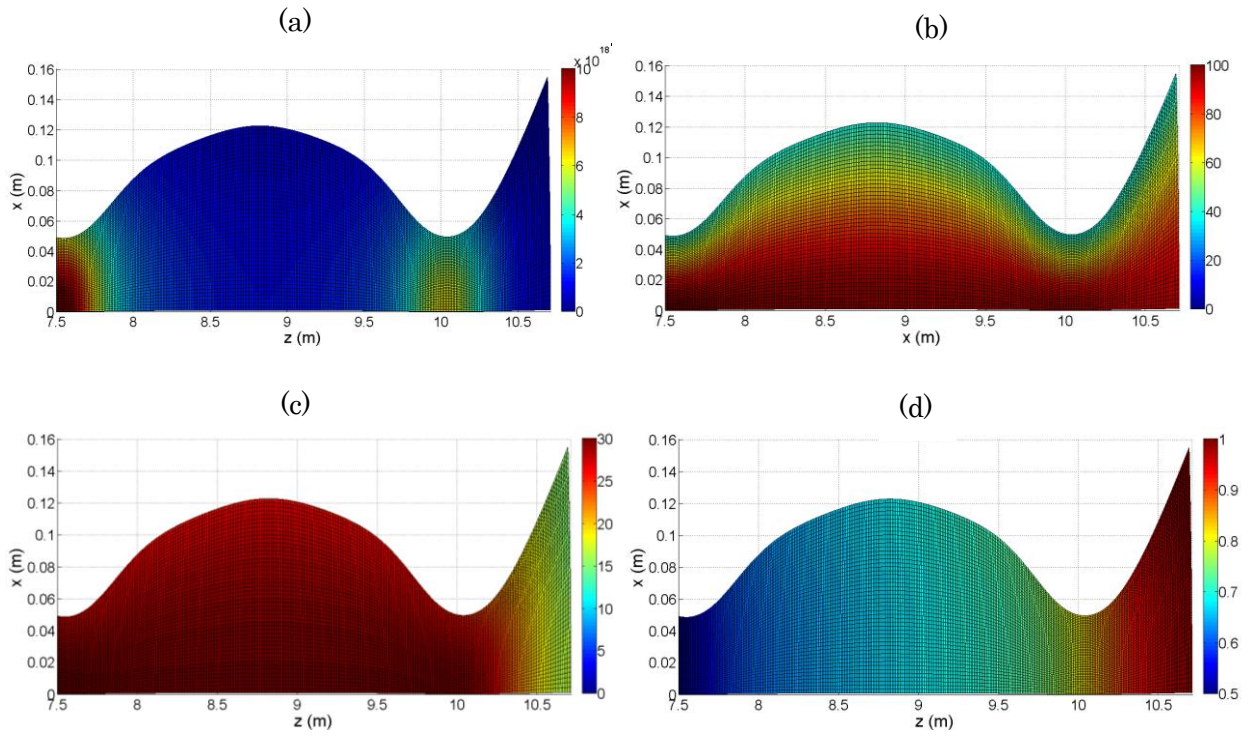


Fig. 21. The distribution of the end-loss plasma parameters, (a): hydrogen ion density, (b): ion temperature, (c): electron temperature, and (d): Ion Mach No. .

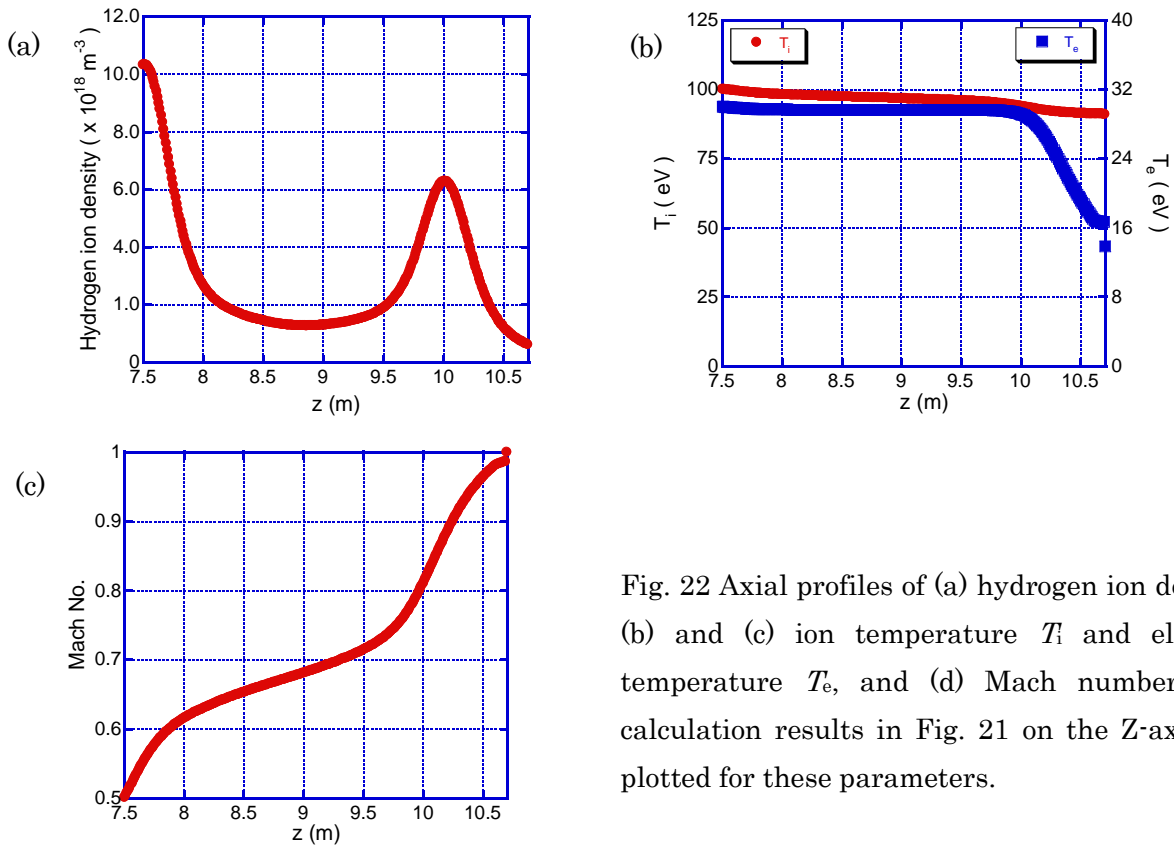


Fig. 22 Axial profiles of (a) hydrogen ion density, (b) and (c) ion temperature  $T_i$  and electron temperature  $T_e$ , and (d) Mach number. The calculation results in Fig. 21 on the Z-axis are plotted for these parameters.

In Figs. 21 (a), hydrogen ion density has two peaks. Each peak is located in the upstream region in the end-cell and west mirror-throat region, respectively. It is natural to form the distribution like Fig. 21 (a) because the magnetic configuration of the plug/barrier cell is mirror magnetic field. In Fig. 22 (a), the amount of hydrogen ion density at mid-plane in the plug/barrier cell becomes as same as that near the target plate. The distributions of ion and electron temperature shown in Figs. 21 (b) and (c) seem to indicate same behavior in the plug/barrier cell. On the other hand, They are different in the end-cell. The electron temperature decreases in the end-cell region toward the target plate, while decrease in the ion temperature  $T_i$  in the end-cell region obtained from the present extended model is not so significant as that in the electron temperature  $T_e$ . In Figs. 21 (d), the behavior of ion Mach number shows axial profile of the ion Mach number is almost the same as that obtained from the previous numerical domain with only the end-cell. However, it is shown that Mach number at the entrance of the end-cell is higher than that in the previous results without using the extended numerical domain. For this reason, the ion velocity could be accelerated by ion and electron pressures near the end-mirror throat coil.

By extending the numerical domain to the upstream region from the end-cell, the basic characteristics at the west mirror throat have been reasonably reproduced. In plug/barrier region, the plasma parameters does not change largely. On the other hand, Mach number is influenced due to expanding the numerical domain.

#### 4.1.2 Extending multi-fluid code

The impurity ions play important roles for the plasma characteristics in the divertor region such as degradation of plasma energy cooling or plasma confinement. Being based on the simplified models for the system of the basic equations given in Chap. 2, the basic analyses have been done so far. Full version of the basic equations in Chap. 2, i.e., multi-fluids model for multi species including the impurity ions with each charge state is used in the following analyses. Impurity ion with a different charge state is treated as a different ion species.

The residence time of the impurity ion in case of the divertor simulation experiments in GAMMA 10/PDX is shorter than the energy relaxation time between hydrogen ion and impurity ion. Therefore, impurity ions are assumed to have a constant temperature which is the room temperature in this thesis. In other word, the ion energy balance equation is not solved for impurity ion and is added the term which is the work done by friction force between different ion species. In addition, the term which represents the energy-exchange reaction between impurity ion and electron by collision is introduced in the electron energy balance equation. By including these effects, ion and electron energy equations, i.e., Eqs. (2.4) and (2.5) have been modified as follows [18];

The new ion energy balance equation:

$$\begin{aligned}
& \frac{\partial}{\partial t} \left( \frac{3}{2} n_i T_i + \sum_{\alpha} \frac{1}{2} \rho_{\alpha} u_{\parallel \alpha}^2 \right) \\
& + \frac{\partial}{\partial x} \left[ \left( \sum_{\alpha} \frac{5}{2} n_{\alpha} u_{\alpha} T_i + \sum_{\alpha} \frac{1}{2} m_{\alpha} n_{\alpha} u_{\alpha} u_{\parallel \alpha}^2 \right) - \left( \kappa_x^i \frac{\partial T_i}{\partial x} + \sum_{\alpha} \frac{1}{2} \eta_x^{\alpha} \frac{\partial u_{\parallel \alpha}^2}{\partial x} \right) \right] \\
& + \frac{\partial}{\partial y} \left[ \left( \sum_{\alpha} \frac{5}{2} n_{\alpha} v_{\alpha} T_i + \sum_{\alpha} \frac{1}{2} m_{\alpha} n_{\alpha} v_{\alpha} u_{\parallel \alpha}^2 \right) - \left( \kappa_y^i \frac{\partial T_i}{\partial y} + \sum_{\alpha} \frac{1}{2} \eta_y^{\alpha} \frac{\partial u_{\parallel \alpha}^2}{\partial y} \right) \right] \\
& = -u_e \frac{\partial p_e}{\partial x} - v_e \frac{\partial p_e}{\partial y} + k(T_e - T_i) + S_E^i + \sum_{\alpha\beta} F_{\alpha\beta} (u_{\parallel b} - u_{\parallel a})
\end{aligned} \tag{4.1}$$

The new electron energy balance equation:

$$\begin{aligned}
& \frac{\partial}{\partial t} \left( \frac{3}{2} n_e T_e \right) + \frac{\partial}{\partial x} \left( \frac{5}{2} n_e u_e T_e - \kappa_x^e \frac{\partial T_e}{\partial x} \right) + \frac{\partial}{\partial y} \left( \frac{5}{2} n_e v_e T_e - \kappa_y^e \frac{\partial T_e}{\partial y} \right) \\
& = u_e \frac{\partial p_e}{\partial x} + v_e \frac{\partial p_e}{\partial y} - k(T_e - T_i) + S_E^e + k_z(T_e - T_z)
\end{aligned} \tag{4.2}$$

The term newly added are introduced as the last term on the right hand side of each energy equations.

One of the characteristics of end-loss plasma in GAMMA 10/PDX is  $T_i \gg T_e$ . The energy transfer coefficients through sheath is expected to be influenced largely. Therefore, the heat transmission coefficients are redefined [39,40].

The ion heat transfer coefficient:

$$\alpha_i \equiv \frac{Q_i}{T_e (j^+ / e)} = \frac{2T_i}{T_e} \tag{4.3}$$

The electron heat transfer coefficient:

$$\alpha_e \equiv \frac{Q_e}{T_e (j^+ / e)} = \frac{2}{1 - \gamma_e} - \frac{1}{2} \ln \left\{ \left( 2\pi \frac{m_e}{m_i} \right) \left( 1 + \frac{T_i}{T_e} \right) (1 - \gamma_e)^{-2} \right\}, \tag{4.4}$$

where the symbol  $\gamma_e$  is the coefficient of secondary electron emission.

## 4.2 Injection of neutral and/or impurity gases into edge plasma by using multi-fluid code

### 4.2.1 Only neutral hydrogen gases injection

By analyzing the effects of neutral hydrogen, the end-loss plasma is calculated under the same conditions of section 3.2.1 in Chapter 3. It is assumed that the injected gas distributes uniformly in the end region and decreases exponentially in the plug/barrier region. Injected neutral gas distribution on the z-axis is shown in Fig. 23.

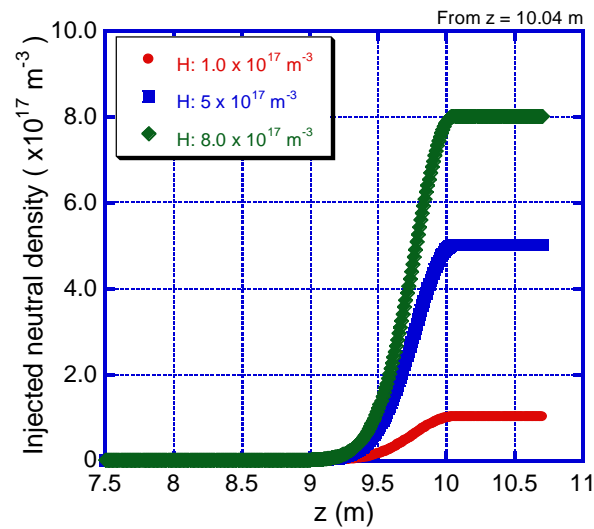
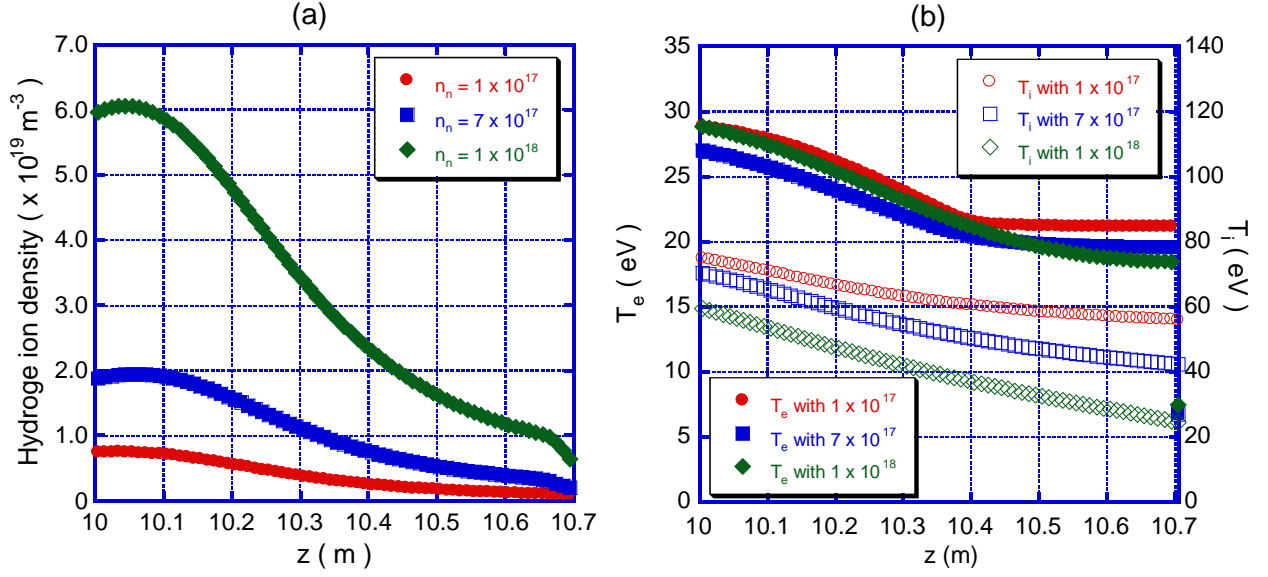


Fig. 23 Distribution of injected neutral density on the z axis.

The amount of injected neutral hydrogen density is  $1.0 \times 10^{17}$ ,  $5.0 \times 10^{17}$ ,  $7.0 \times 10^{17}$  and  $1.0 \times 10^{18}$   $\text{m}^{-3}$ . The axial profiles of ion density, ion and electron temperature on the z-axis under the conditions of neutral hydrogen injection are shown in Figs. 24 (a) and (b).



Figs. 24 The  $z$ -axial profile of (a) ion density and (b) ion and electron temperatures.

In Fig. 24 (a), the green line indicates the ion density on the  $z$  axis under the condition of the injected hydrogen at  $1.0 \times 10^{17} \text{ m}^{-3}$ , the blue line corresponds to the condition of  $5.0 \times 10^{17} \text{ m}^{-3}$  and the red line represents in case of injected amount of the  $1.0 \times 10^{18} \text{ m}^{-3}$ . The hydrogen ion density building up at  $z = 10.04$  m which is situated beside the west end-mirror throat with increasing injected neutral hydrogen. In case of injecting neutral at  $1.0 \times 10^{18} \text{ m}^{-3}$ , it is observed that the hydrogen ion density at mirror throat is 6 times as large as under the condition of injecting neutral at  $1.0 \times 10^{17} \text{ m}^{-3}$ . The peak point of hydrogen density keeps at the mirror throat differently from the result of single fluid code. In Fig. 24 (b), the line color same corresponding to Fig. 24 (a). The solid symbols indicates ion temperature and the open symbols represents electron temperature. As seen from Fig. 24, the dependence of  $T_i$  on injected neutral density  $\underline{n}_n$  is almost similar to that of  $T_e$  in the region  $10.4 \text{ m} < z < 10.7 \text{ m}$  near the target plate. The dependence, however, becomes different in the region  $10 \text{ m} < z < 10.4 \text{ m}$ . It is shown that at the west mirror throat, ion and electron temperature are influenced by the amount of the injected neutral hydrogen.

In Fig. 25, ion and electron temperature and hydrogen ion density at the target plate are shown. The increasing rate of hydrogen ion density with neutral hydrogen injected is similar to the increase rate of hydrogen ion density at west mirror-throat. Ion temperature decreases obviously with increasing neutral injection. Ion temperature is reduced to nearly 50 % for the case with  $1.0 \times 10^{18} \text{ m}^{-3}$  compared with the case of  $1.0 \times 10^{17} \text{ m}^{-3}$ . On the other hand, electron temperature changes slightly.

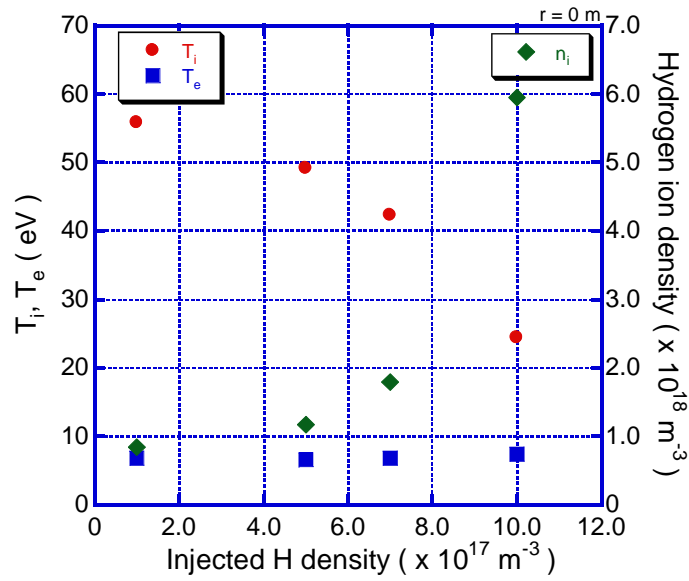
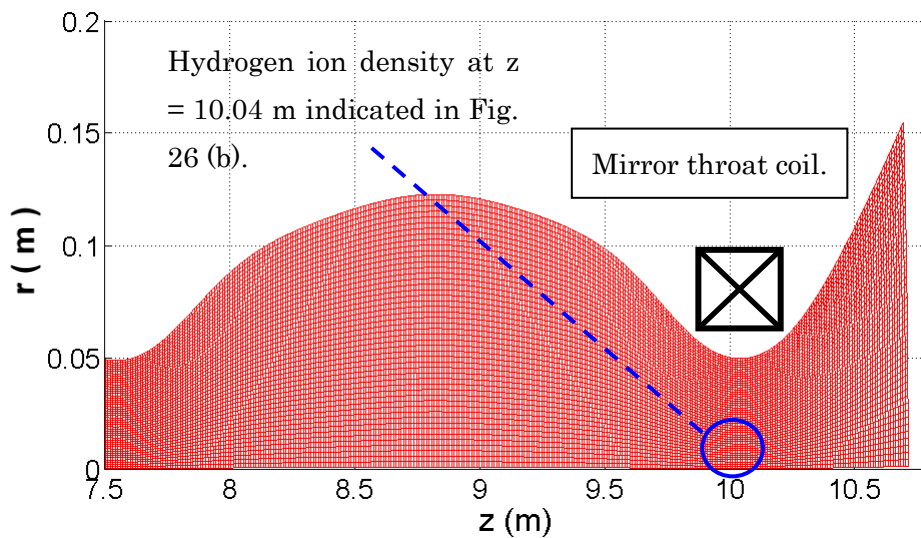
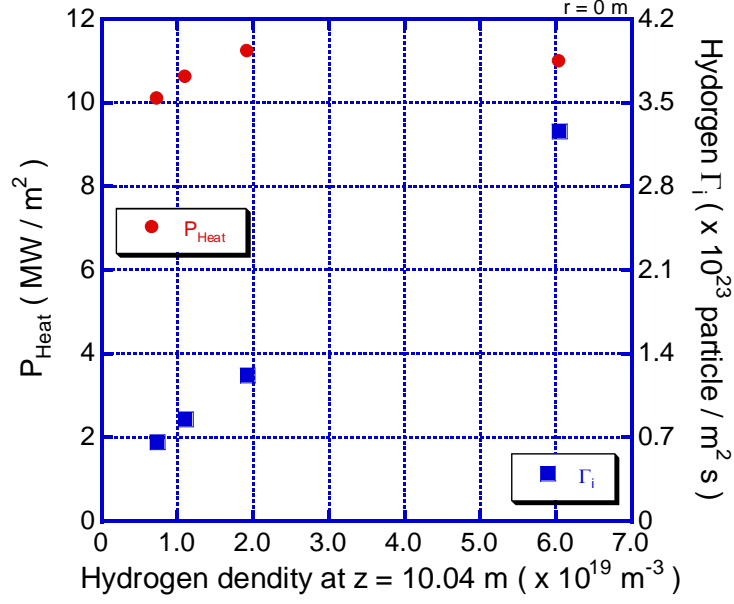


Fig. 25 ion and electron temperature and hydrogen ion density at the target plate.

In Fig. 26 (b), heat and particle fluxes on the target plate is shown as a function of the hydrogen ion density at the west mirror throat shown in Fig. 26 (a). Heat load tends to decrease with increasing incident hydrogen neutral density into the plasma due to the reduction of ion temperature and sheath transfer coefficient for ion. On the other hand, particle flux tends to keep increasing. That is because the increase of ion density keeps with injected neutral hydrogen shown in Fig. 25. Plasma behavior in the plug/barrier cell should not be ignored for the understanding the phenomena near the target plate because the influx plasma parameters are changed with neutral hydrogen injection.



Figs. 26 (a) The positions of the west mirror throat coil.



Figs. 26 (b) Heat and particle fluxes on the target plate as a function of the hydrogen ion density at the west mirror-throat.

#### 4.2.2 Evaluation of Ar injection effects by using multi-fluid code

The neutral Ar density produces the reduction of heat load and particle flux on the target plate as shown in the previous chapter. Therefore, the calculation under the condition of only neutral Ar injection is performed for evaluating the effects of impurity neutrals and ions. The neutral Ar is injected into the plasma at the amount from  $5.0 \times 10^{17} \text{ m}^{-3}$  to  $1.6 \times 10^{19} \text{ m}^{-3}$ . Figure 27 shows ion and electron temperatures and hydrogen ion and argon ion density at the target plate on the z-axis.

In Fig. 27 (a), the circle symbols show hydrogen ion density, the square symbols indicate Ar ion density.  $\text{H}^+$  density decrease nearly 0.5 times with increasing injected Ar density. However, the injected neutral Ar more than  $4.0 \times 10^{18} \text{ m}^{-3}$ , the decrease of  $\text{H}^+$  density is saturated. The amount of  $\text{Ar}^+$  density rises abruptly at injected Ar density of  $1.0 \times 10^{18} \text{ m}^{-3}$ . After that,  $\text{Ar}^+$  density decreases from about  $3.5 \times 10^{18} \text{ m}^{-3}$  to about  $1.5 \times 10^{18} \text{ m}^{-3}$ . This reduction rate is larger than the in the case of  $\text{H}^+$  density and the decreasing trend of reducing  $\text{Ar}^+$  density tends to keep under the condition of high injected neutral Ar density. Therefore, it is expected that electron density has a peak in the case of focus on the electron density.

In Figs. 27 (b),  $\text{H}^+$  and electron temperature with increasing injected neutral Ar density are shown. The circle symbols show  $\text{H}^+$  temperature and the square symbols indicate electron temperature. Both the temperature dependences are similar to each other.  $\text{H}^+$  ion temperature decrease from about 90 eV to 30 eV. The reduction of electron temperature reaches from about 24 eV

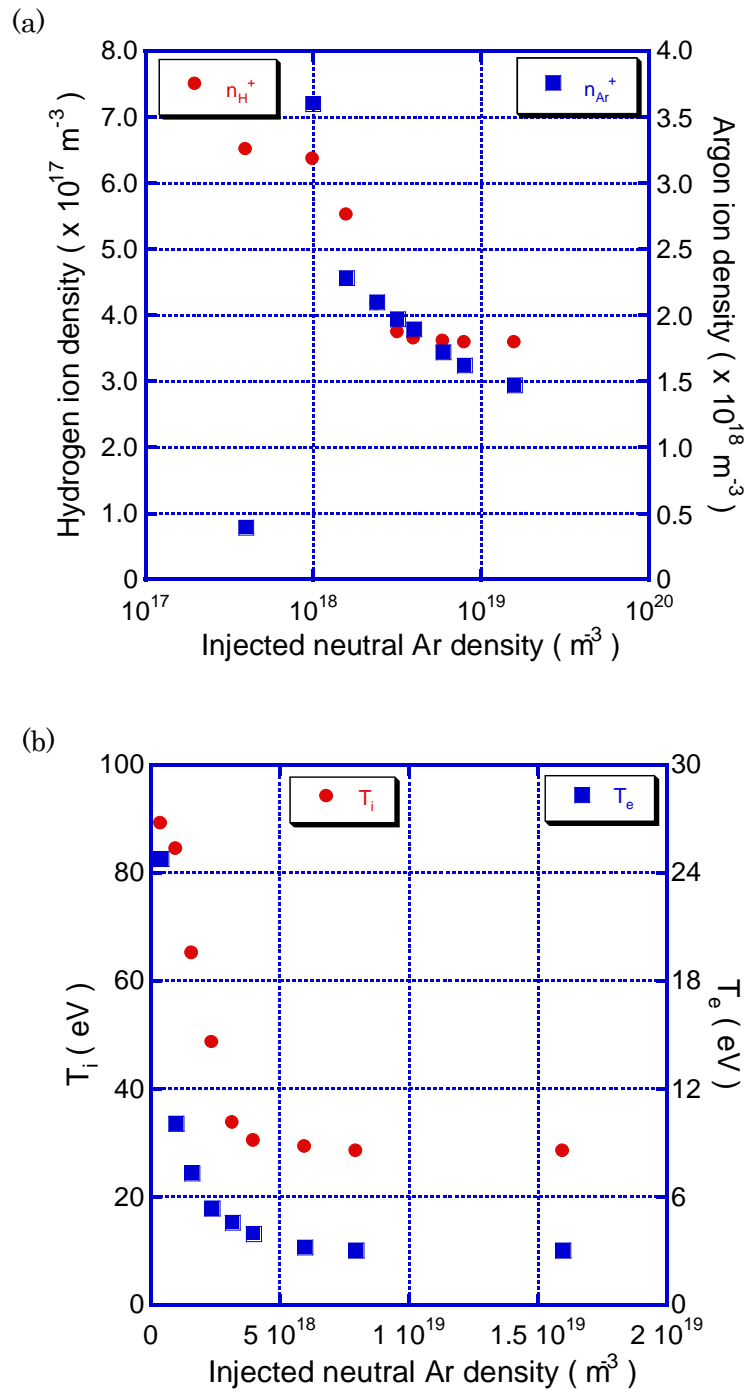
to about 3 eV. However, the reduction of both temperatures does not occur more than injected Ar density :  $4.0 \times 10^{18} \text{ m}^{-3}$ . In addition, the energy relaxation between  $\text{H}^+$  and electron temperatures are not observed though neutral Ar is injected up to  $1.6 \times 10^{19} \text{ m}^{-3}$ .

The work done by the friction force between hydrogen and argon ion does not become the effective factor of decreasing ion energy in all cases as shown in Fig. 28 (a). In case of only neutral Ar injection, the ion energy loss processes consist of the electron drag and atomic molecular interactions, however the percentage of the all energy loss or gain processes of these effective loss processes reaches only to nearly the 40 %. Therefore, it is seemed that there is weak influences of neutral Ar injection for reducing hydrogen ion temperature. This event is indicated in the atomic molecular interaction as shown in Fig. 28 (b). The process of charge exchange reaction between hydrogen ion and neutral Ar becomes the very low reaction rate. Charge exchange loss with Ar is not observed under the condition of only Ar  $1.6 \times 10^{19} \text{ m}^{-3}$ .

On the other hand, the effective electron energy loss factor is the atomic molecular interactions as shown in Fig. 29 (a). In Fig. 29 (b), the radiation cooling by inelastic collision with neutral Ar particles strongly influences the reduction of electron energy in the all cases. However, in the case of neutral Ar injection  $1.6 \times 10^{19} \text{ m}^{-3}$ , the percentage of radiation cooling effect decreases and electron drag effect increases. The radiation cooling effects of neutral Ar is low in the case of the electron temperature less than about 3 eV from the radiation function of Ar defined as Fig. 16 in the section 3.2. From that reason, it is considered that the  $T_e$  tends to keep constant under the condition of injected neutral Ar more than  $4.0 \times 10^{18} \text{ m}^{-3}$ . Therefore, the decrease of decrease  $\text{Ar}^+$  density is occurred because of not the recombination of  $\text{Ar}^+$  but inhibiting the electron-impact ionization as shown by Fig. 29.

In Fig. 30, heat flux and particle flux of  $\text{H}^+$  and  $\text{Ar}^+$  on the target plate at z axis are shown. Heat load on the target plate keeps the same value with increasing injected neutral Ar density. In the injected high neutral Ar density region, the hydrogen ion temperature  $T_i$  and density  $n_i$  tend to hardly decrease. However, it seems that the heat load is difficult to reduce because the ion and electron heat transfer coefficient defined by the Eqs. (4.3) and (4.4) increase slightly. The small reduction of the  $\text{H}^+$  particle flux density is observed. On the other hand, the particle flux of  $\text{Ar}^+$  has a peak at the injected neutral Ar density of  $3.2 \times 10^{18} \text{ m}^{-3}$  and then decreases obviously. It seems that this behavior of  $\text{Ar}^+$  particle flux is occurred by the reduction of  $\text{Ar}^+$  density due to controlling the electron-impact ionization by low  $T_e$  as shown in Fig. 28.

From these results, it is found that the only Ar gas injection into the plasma is useful to decrease  $T_e$  and charged particles density however, the effect of the reduction of  $\text{H}^+$  energy is expected not to become main presence. Therefore, it is considered that it is needed to decrease  $\text{H}^+$  energy obviously for the reduction of heat load.



Figs. 27 The dependence of hydrogen and argon ion densities on the injected neutral Ar density. (a); the dependence of the hydrogen ion and (b); electron temperature on the neutral Ar injection.

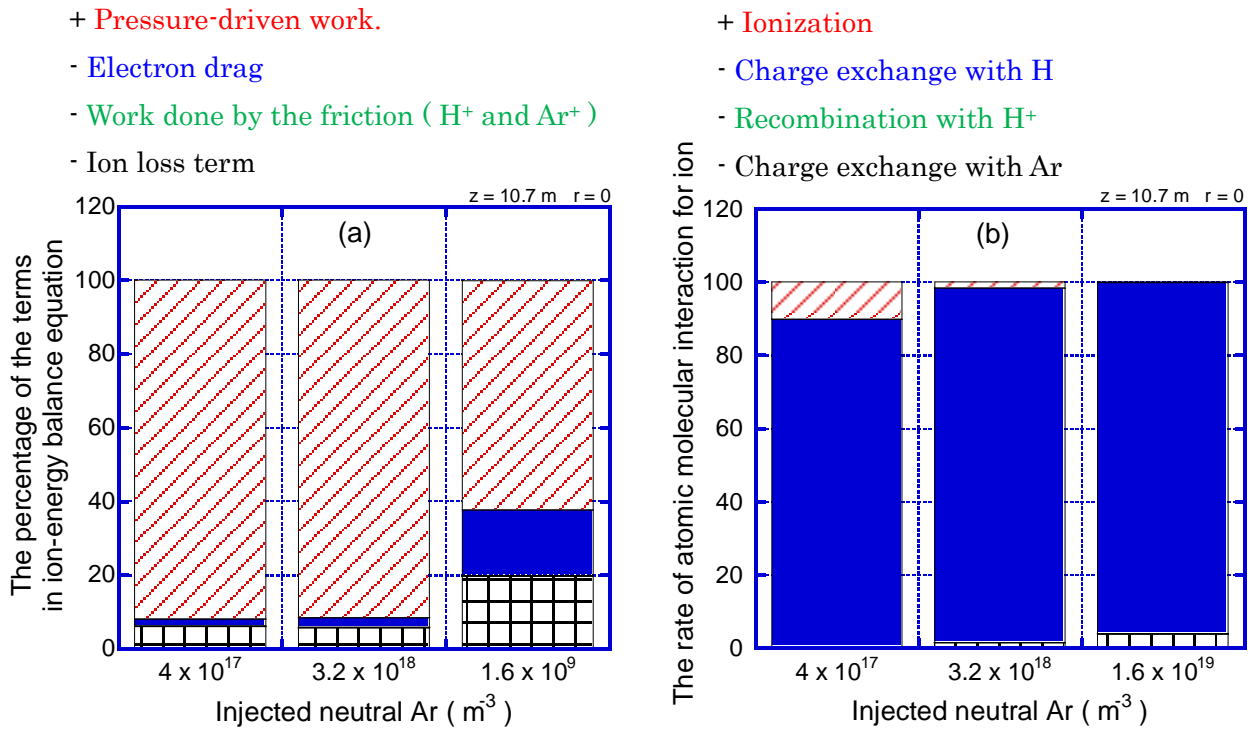


Fig. 27 The percentage of ion energy balance equation. (a) the percentage of the terms in ion-energy balance equation and (b) the rate of atomic molecular interaction for ion.

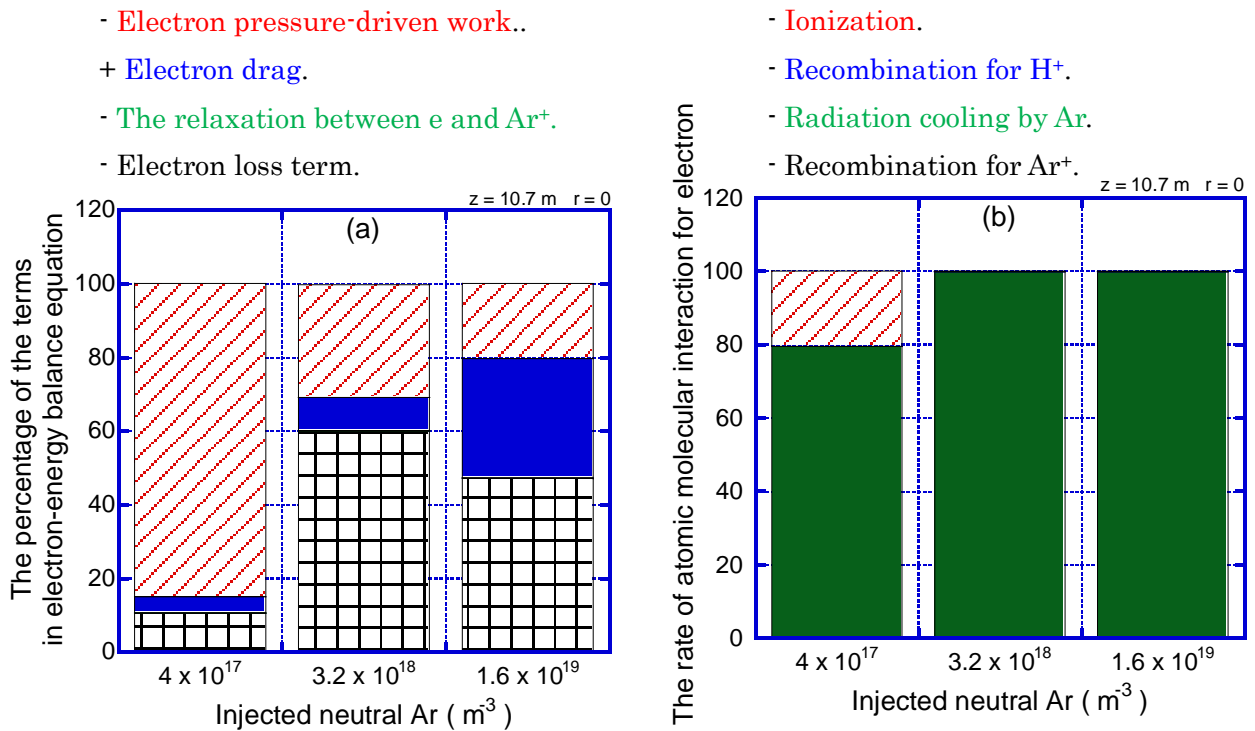


Fig. 28 The percentage of electron balance equation. (a) the percentage of the terms in electron-balance equation and (b) the rate of atomic molecular interaction for electron.

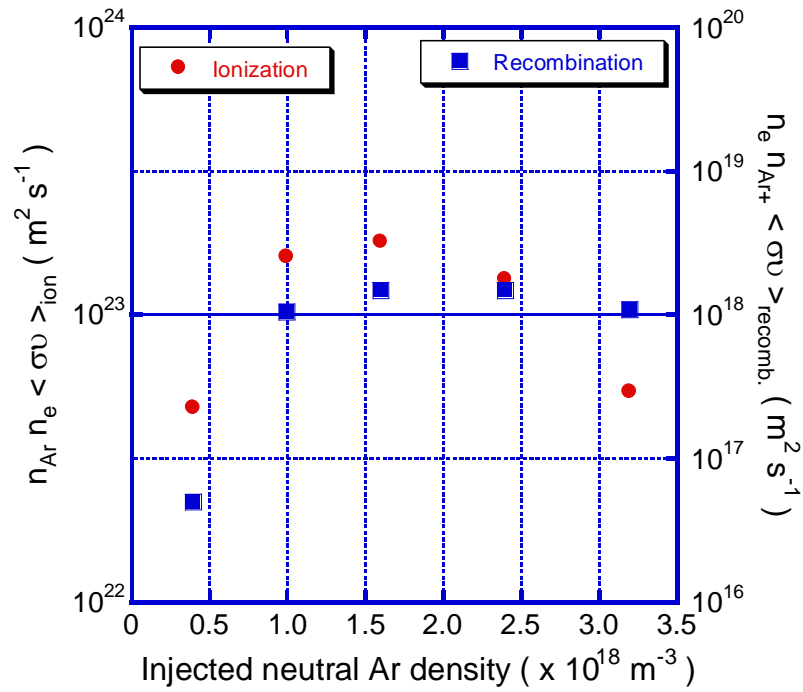


Fig. 29 The rate coefficients of  $H^+$  electron-impact ionization and recombination.

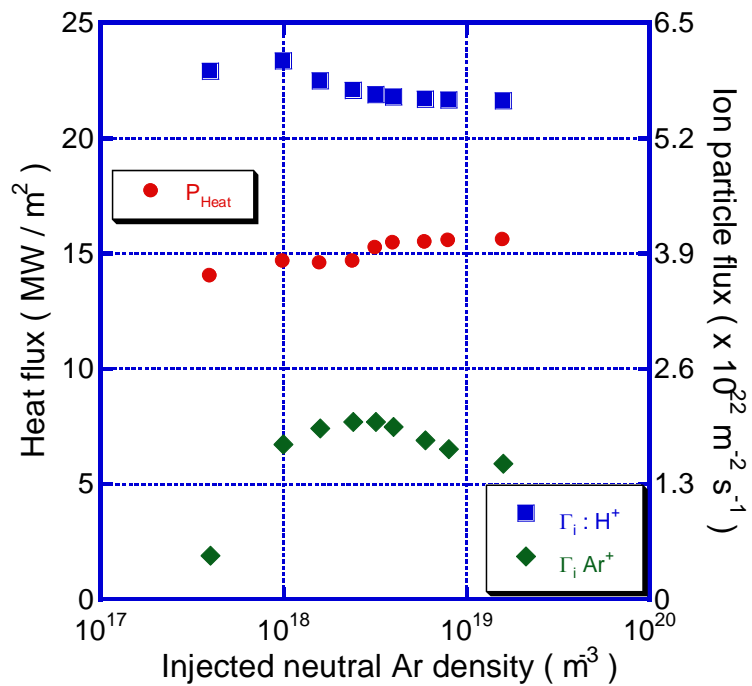
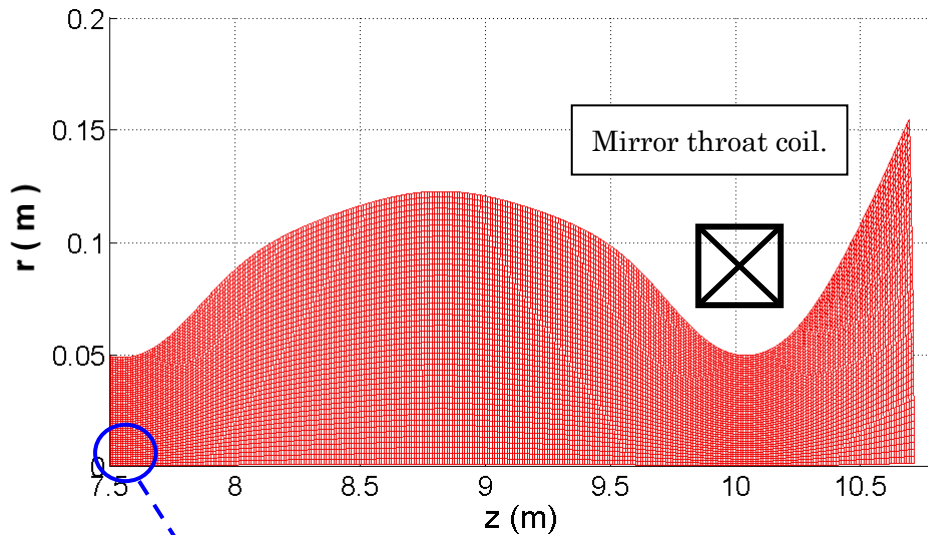


Fig. 30 Heat load and particle flux of  $H^+$  and  $Ar^+$  on the target plate dependence on injected Ar density.

In Fig. 32, the dependence of  $\text{Ar}^+$  particle flux density toward the central cell on the injected neutral Ar density is shown on the  $z$ -axis at the plasma inlet region indicated as shown in Fig. 31. The particle flux of  $\text{Ar}^+$  toward the central cell keeps to increase from  $4.0 \times 10^{17} \text{ m}^{-3}$  to  $3.2 \times 10^{18} \text{ m}^{-3}$  and has a peak at  $\text{Ar} = 3.2 \times 10^{18} \text{ m}^{-3}$ . In the region of more than  $\text{Ar} 3.2 \times 10^{18} \text{ m}^{-3}$ , the amount of  $\text{Ar}^+$  particle flux flowing out toward the central cell increases gently.

Fig. 33, the dependence of Ar ion density and velocity on the  $z$ -axis at the upstream region ( $z = 7.5 \text{ m}$ ) is indicated. From Fig. 32, the dependence of  $\text{Ar}^+$  particle flux is similar to the dependence of  $\text{Ar}^+$  ion density compared with  $\text{Ar}^+$  ion velocity. Therefore, it is thought that the amount of the  $\text{Ar}^+$  density is the most important factor for deciding the amount of backflow of  $\text{Ar}^+$  particle flux.



Argon ion particle flux toward the central cell and Argon ion density and velocity are shown in Fig. 32 and 33 at the position.

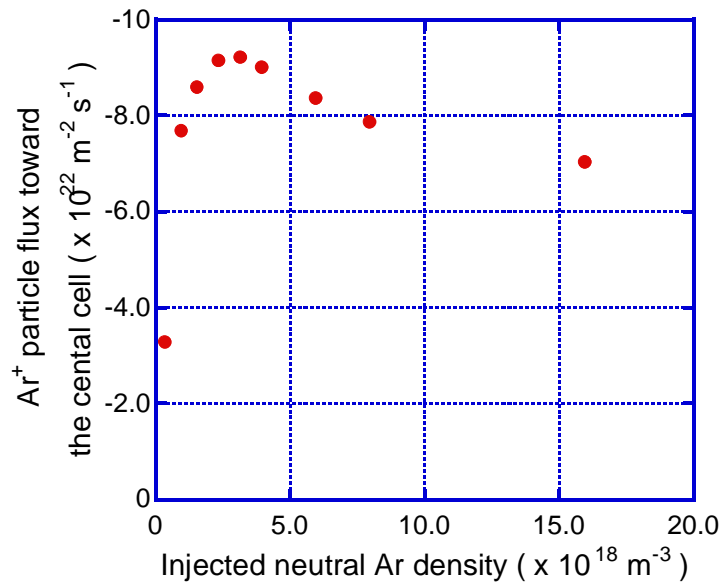


Fig. 32. The dependence of  $\text{Ar}^+$  particle flux with plasma inlet region on the z-axis at the plasma inlet region.

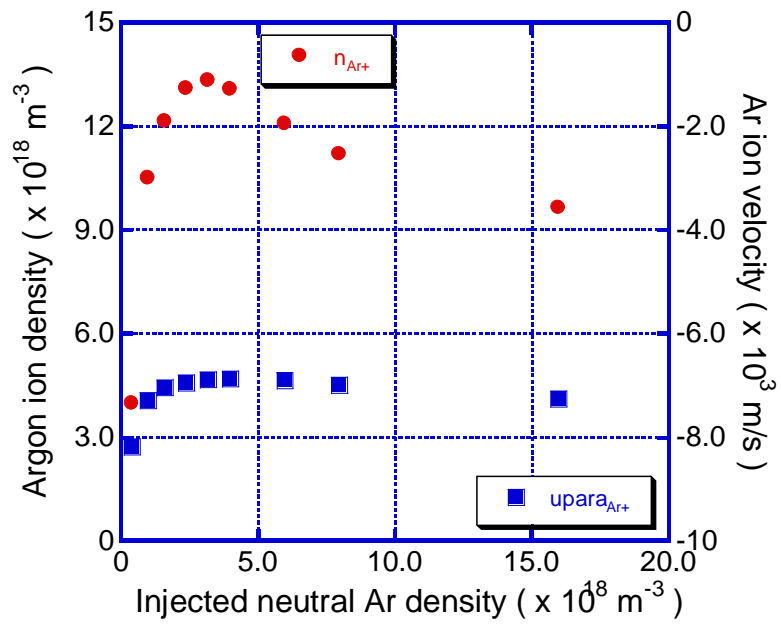
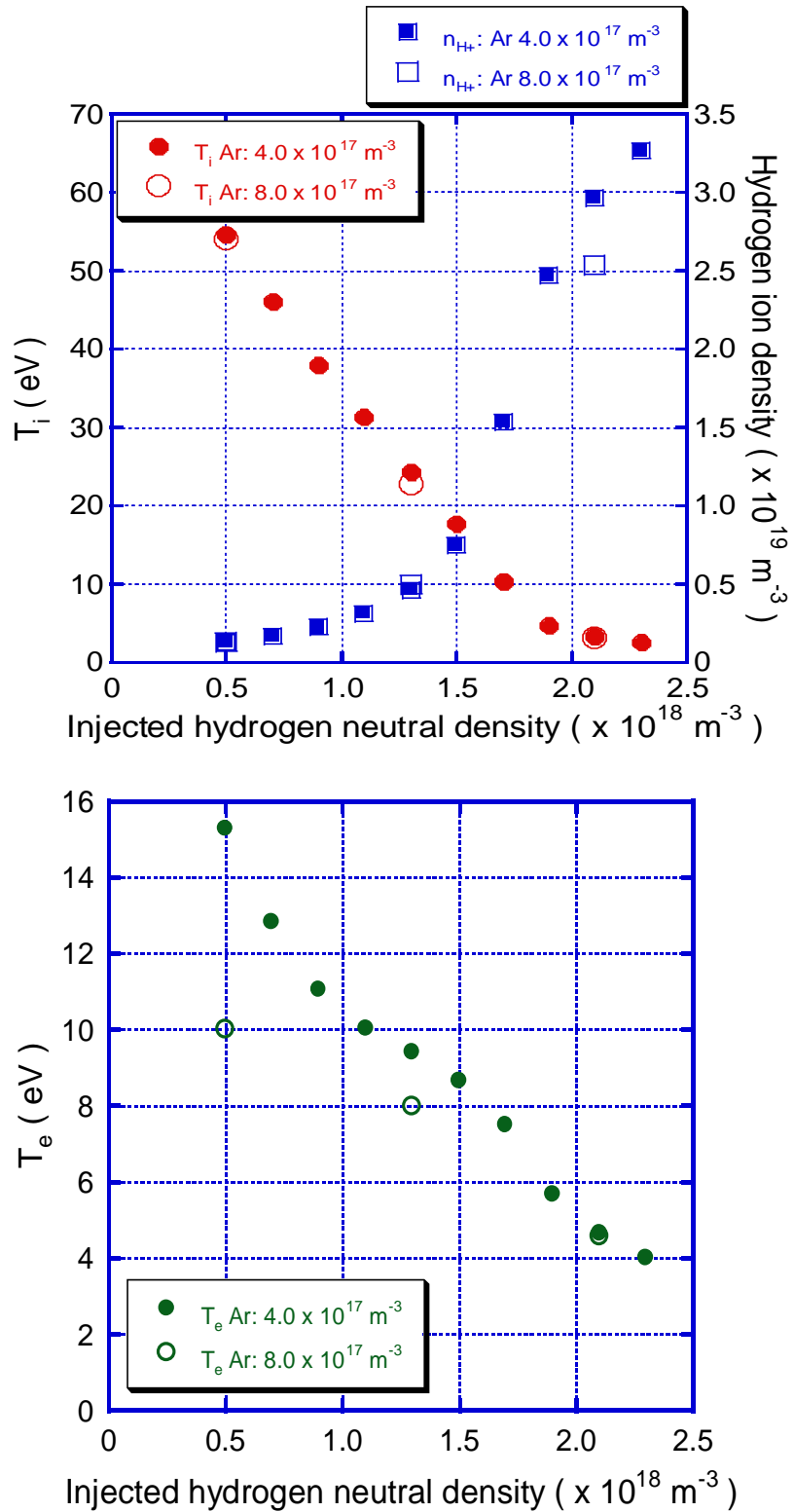


Fig. 33 The dependence of  $\text{Ar}^+$  density and velocity with neutral Ar injection on the z-axis in the inlet plasma region.

### 4.2.3 Simultaneous injection of Hydrogen and Argon gases

In the case of only neutral hydrogen injection,  $H^+$  temperature tends to decrease obviously by the charge-exchange loss and increase in the  $H^+$  density as seen in Fig. 25. In the case of only neutral argon injection, on the other hand, electron temperature decreases actively and the increase in the  $H^+$  density is lower than under the condition of only neutral hydrogen injection. It is expected that the simultaneous injecting neutral hydrogen and argon leads to the detached plasma state more easily than the case with only the neutral or Ar injection. In this section, the Ar gas density is fixed at  $5.0 \times 10^{17} \text{ m}^{-3}$ , while the neutral hydrogen density is changed from  $5.0 \times 10^{17} \text{ m}^{-3}$  to  $2.3 \times 10^{18} \text{ m}^{-3}$ . In addition, higher Ar density case with  $8.0 \times 10^{17} \text{ m}^{-3}$  is examined with varying injected neutral hydrogen density at  $5.0 \times 10^{17}$ ,  $1.3 \times 10^{18}$ ,  $2.1 \times 10^{18} \text{ m}^{-3}$ .

The results are summarized in Fig. 30. The ion temperature and hydrogen ion density are shown as a function of the injected hydrogen density in Fig. 34 (a). The dependence of the electron temperature on the injected hydrogen density is shown in Fig. 34 (b).  $H^+$  temperature with Ar :  $5.0 \times 10^{17} \text{ m}^{-3}$  decreases to nearly 0.05 times of ion temperature with increase of injected neutral hydrogen density like the condition of only neutral hydrogen injection. In the low hydrogen density, it is shown that  $H^+$  temperature decreases almost linearly with the injected neutral hydrogen density. On the other hand, in high hydrogen density region after  $1.9 \times 10^{18} \text{ m}^{-3}$ , it is difficult for  $H^+$  temperature to decrease. In the case of Ar :  $8.0 \times 10^{17} \text{ m}^{-3}$ ,  $H^+$  temperatures are almost the same as those for the case of Ar :  $5.0 \times 10^{17} \text{ m}^{-3}$ .  $H^+$  density with Ar :  $5.0 \times 10^{17} \text{ m}^{-3}$  increases from nearly  $1.0 \times 10^{18} \text{ m}^{-3}$  to  $3.3 \times 10^{19} \text{ m}^{-3}$  with increasing injected neutral hydrogen density. In case of Ar :  $8.0 \times 10^{17} \text{ m}^{-3}$ ,  $H^+$  density does not make a difference compared with the condition of Ar :  $4.0 \times 10^{17} \text{ m}^{-3}$ . However, the hydrogen ion  $H^+$  density observed at high injected neutral hydrogen density range is lower than in the case of the amount of injected Ar gas :  $4.0 \times 10^{17} \text{ m}^{-3}$ . The electron temperature shown in Fig. 30 (b) decrease from 16 eV to 4 eV as well as  $H^+$  temperature with increasing injected hydrogen neutral. However, electron temperature is kept decreasing regardless of low or high injected neutral hydrogen range. In addition, Ion and electron temperature relaxation has been observed under the relatively high density range of the injected hydrogen ( $> 1.9 \times 10^{18} \text{ m}^{-3}$ ). In the case of injecting Ar :  $8.0 \times 10^{17} \text{ m}^{-3}$ , the decrease ratio of electron temperature with increase in the injected neutral hydrogen tends to be smaller than in the condition of Ar injection :  $4.0 \times 10^{17} \text{ m}^{-3}$ .



Figs. 34 The plasma parameters on the target plate at the z-axis dependence on injected neutral hydrogen density. The closed symbols are indicated as the condition of Ar :  $4.0 \times 10^{17} \text{ m}^{-3}$  and the open symbols show in case of Ar :  $8.0 \times 10^{17} \text{ m}^{-3}$ . (a) : Ion temperatures and  $\text{H}^+$  densities and (b) : Electron temperatures.

In Fig. 35, the dependence of the heat and particle fluxes on injected hydrogen density are shown. The closed symbols of red cycle and blue square show the results under the condition of  $4.0 \times 10^{17} \text{ m}^{-3}$ . On the other hand, the open symbols of red cycle and blue square indicate those with Ar :  $8.0 \times 10^{17} \text{ m}^{-3}$ . The heat load on the target plate decreases with injected hydrogen gas density. The decrease in the heat flux becomes 0.2 times compared with the conditions of injected neutral hydrogen gas  $5.0 \times 10^{17} \text{ m}^{-3}$  and  $2.3 \times 10^{18} \text{ m}^{-3}$ .

In addition, the degree of decreasing heat load varies. It is considered that the energy loss, which is caused by the charge exchange between  $\text{H}^+$  and hydrogen neutral under the large amount of injected hydrogen neutral gas, tends to become small due to low  $\text{H}^+$  temperature. Particle flux at the target plate become almost 10 times larger with increasing injected neutral hydrogen density from  $9.1 \times 10^{22} \text{ m}^{-3}$  to  $9.9 \times 10^{23} \text{ m}^{-3}$ . However, it is observed that particle flux with injected neutral hydrogen more than  $2.1 \times 10^{18} \text{ m}^{-3}$  tends to become saturating. Therefore, it is seemed that upstream plasma is approaching to the plasma detachment state because the increase of particle flux toward the target plate begins to be settled. In the condition of Ar :  $8.0 \times 10^{17} \text{ m}^{-3}$ , Heat load and particle flux decrease, however, the reduction of heat load and particle flux is small compared with neutral Ar injection :  $4.0 \times 10^{17} \text{ m}^{-3}$ . It is needed that the amount of the injected Ar neutral gas is larger for making the impurity injection more effective for reducing the heat and particle loads.

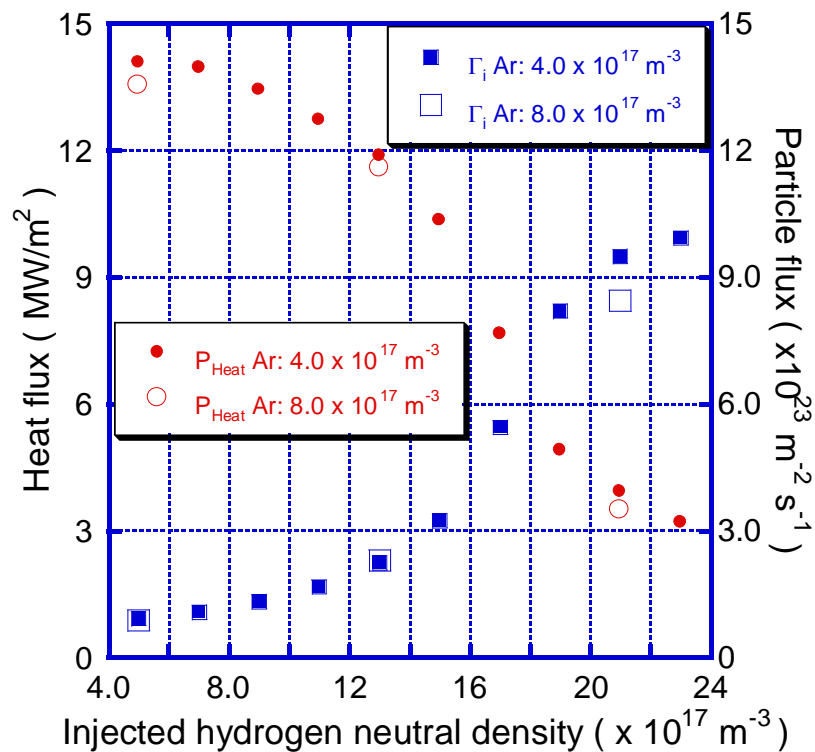


Fig. 35 Dependence of heat load and particle flux on the target plate on injected hydrogen density.

The reduction of  $T_i$  and  $T_e$  causing decrease of heat load on the target plate is produced through the several phenomena. Figure 36 shows that the rate of the physical processes acting as variation of  $H^+$  ion and electron energy under the conditions of the amount of injected hydrogen as  $5.0 \times 10^{17} \text{ m}^{-3}$ ,  $1.7 \times 10^{18} \text{ m}^{-3}$  and  $2.3 \times 10^{18} \text{ m}^{-3}$ . Figure 36 (a) indicates the pressure work, electron drag, the work of friction force between  $H^+$  and  $Ar^+$  and the interaction between  $H^+$  ion and neutrals defined at energy balance equation in case of ion and Fig. (b) represents the phenomena which are electron pressure work, electron drag, the energy relaxation between electron and  $Ar^+$  and interaction between electron and neutrals in case of electron.

In all conditions, the influence of interaction with Ar ion is very low such as the work done by the friction force between  $H^+$  and  $Ar^+$  for ion energy and the relaxation between electron and  $Ar^+$  energy. In Fig. 36 (a), the interactions between  $H^+$  and neural particles increase constantly with increasing injected neutral hydrogen density. Energy transfer from ion to electron by the collision increases under the condition of injected hydrogen density  $1.7 \times 10^{18} \text{ m}^{-3}$  due to building up the electron density in this condition by ionization of neutral hydrogen particles. However, in the case of injected hydrogen density of  $2.3 \times 10^{18} \text{ m}^{-3}$ , the influence of electron drag decreases because the energy relaxation between  $T_i$  and  $T_e$  almost has occurred. The pressure-driven effects which gives energy to the ions does not depend on the amount of injected neutral particle density. The pressure work tends to become the most effective factor in all processes. However, the pressure generated by injected neutral particle largely depends on the density of injected neutral density. Therefore, it is seemed that the physical processes which should be focused are electron drag and the interaction between charged and neutral particles. In case of  $T_i$ , it is considered that the increasing of electron drag and the interaction of charge and neutral particle is important for decreasing  $T_i$ . On the other hand, the variation of the electron drag and electron pressure work is similar to the case of  $H^+$  energy in Fig. 36 (b). The rate of the interaction between electron and neutral particles increases than the case of hydrogen ion energy and accounts for the greatest proportion of the electron energy loss processes.

The interaction of charge and neutral particles for ions or electron includes several processes. For  $H^+$ , ionization, charge exchange loss between hydrogen ion and neutrals, recombination and charge exchange loss between hydrogen ion and Ar neutrals are considered. For electron, collisional ionization, recombination for  $H^+$  and  $Ar^+$  and the radiation cooling by Ar are considered. In Fig. 37 (a) and (b) show the rate of atomic molecular interaction for ion or electron. In Fig. 37 (a), it is found that the most effective process is charge exchange loss between hydrogen ion and neutral particles. The charge exchange loss between hydrogen ions and neutrals reaches to about 96 %. Therefore, other processes such as recombination for  $H^+$  and charge exchange loss with Ar are very little existent. In Fig. 37 (b), the recombination of  $H^+$  or  $Ar^+$  is not hardly any influence for electron energy loss. The effective processes are the effect of the coalitional ionization for  $H^+$  and inelastic collision with neutral Ar particles. Especially, the radiation loss by inelastic collision with neutral Ar keeps to be large influence despite the amount of neutral Ar injected into plasma which is lower

than the injected neutral hydrogen. Therefore, the effects of radiation loss by injecting impurity gas is important to achieve the reduction of electron energy.

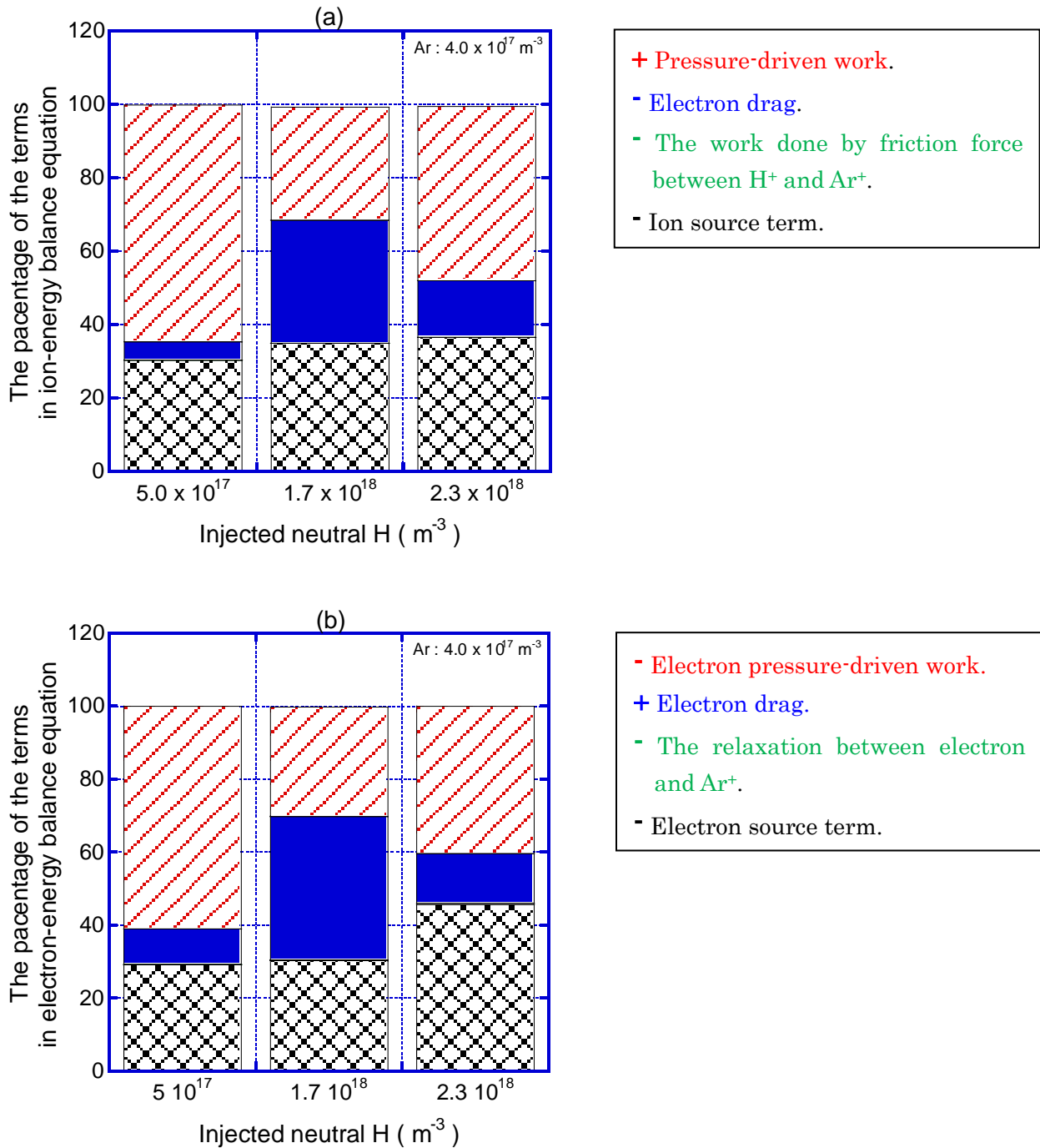
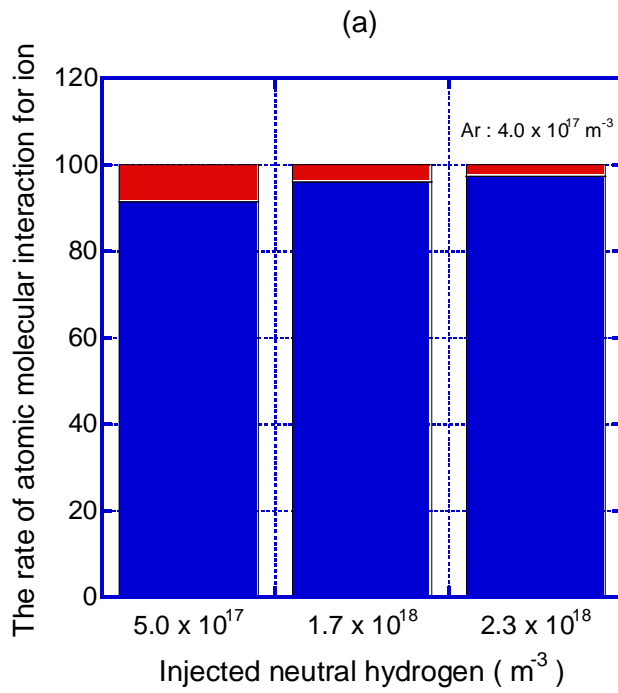
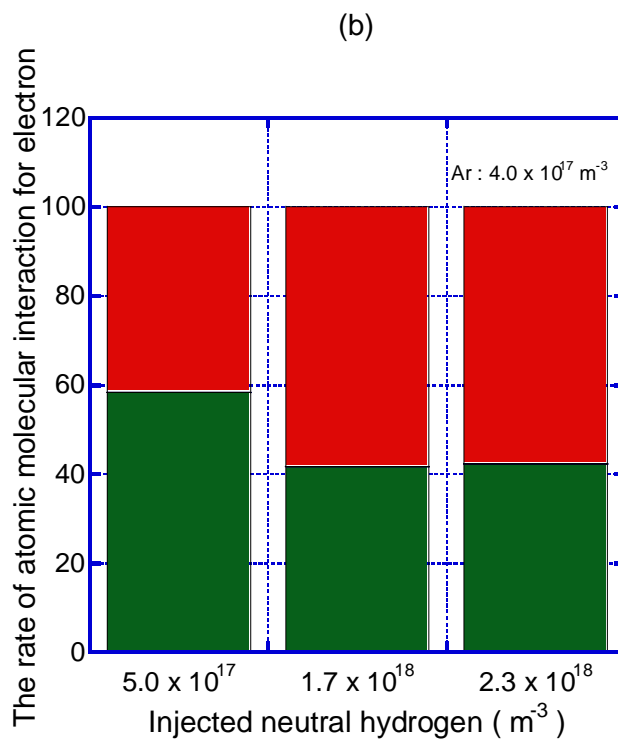


Fig. 36 The rate of the physical processes acting as variation of  $\text{H}^+$  ion and electron energy under the conditions of the amount of injected hydrogen as  $5.0 \times 10^{17} \text{ m}^{-3}$ ,  $1.7 \times 10^{18} \text{ m}^{-3}$  and  $2.3 \times 10^{18} \text{ m}^{-3}$ . (a) :  $\text{H}^+$  ion energy and (b) : electron energy.



- + Ionization.
- Charge exchange loss between hydrogen neutrals and ions.
- Recombination for  $\text{H}^+$ .
- Charge exchange loss between  $\text{H}^+$  and neutral Ar.



- Ionization.
- Recombination for  $\text{H}^+$ .
- Radiation cooling by inelastic collision with neutral Ar.
- Recombination for  $\text{Ar}^+$ .

Fig. 37 The rate of atomic molecular interaction in the energy source terms. (a) : ion and (b) : electron.

In Fig. 38 shows  $\text{Ar}^+$  particle flux flowing out toward the central-cell as a function of the density for the injected neutral hydrogen. The red circles symbols indicate the results in the case of  $\text{Ar } 4.0 \times 10^{17} \text{ m}^{-3}$ . The square symbols show those with  $8.0 \times 10^{17} \text{ m}^{-3}$ . Under the condition of  $\text{Ar} : 4.0 \times 10^{17} \text{ m}^{-3}$ ,  $\text{Ar}^+$  particle flux ( $z = 7.5 \text{ m}$ ) toward the central-cell first almost is unchanged for the density range of the hydrogen neutral density  $0.5 \times 10^{18} \text{ m}^{-3} < n_{\text{H}} < 1.0 \times 10^{18} \text{ m}^{-3}$ . Secondly, it starts increasing up to the case with  $n_{\text{H}} = 1.0 \times 10^{18} \text{ m}^{-3}$ . Finally, the  $\text{Ar}^+$  flux starts decreasing for higher neutral density. In all the range of the  $n_{\text{H}}$ , the flow velocity of  $\text{Ar}^+$  ions is decelerated by the friction force by  $\text{H}^+$ . However,  $\text{Ar}^+$  density increases till neutral hydrogen density reaches  $1.7 \times 10^{18} \text{ m}^{-3}$  due to relatively high electron temperature ( see Fig. 34 ) and the resulting high ionization rate of Ar. Thus, the particle flux of  $\text{Ar}^+$  possibly increases. On the other hand,  $\text{Ar}^+$  particle flux declines after increasing injected neutral hydrogen gas at  $1.7 \times 10^{18} \text{ m}^{-3}$  as mentioned above. This is because  $\text{Ar}^+$  density decreases due to low electron temperature state in the range of the injected neutral hydrogen larger than  $1.7 \times 10^{18} \text{ m}^{-3}$ .

The  $\text{Ar}^+$  particle flux under the condition of injected Ar gas  $8.0 \times 10^{17} \text{ m}^{-3}$  shows the similar dependence to the case of neutral Ar gas density  $4.0 \times 10^{17} \text{ m}^{-3}$ . The amount of backflow  $\text{Ar}^+$  particle flux is larger than the result under the condition of injected Ar gas  $4.0 \times 10^{17} \text{ m}^{-3}$ .

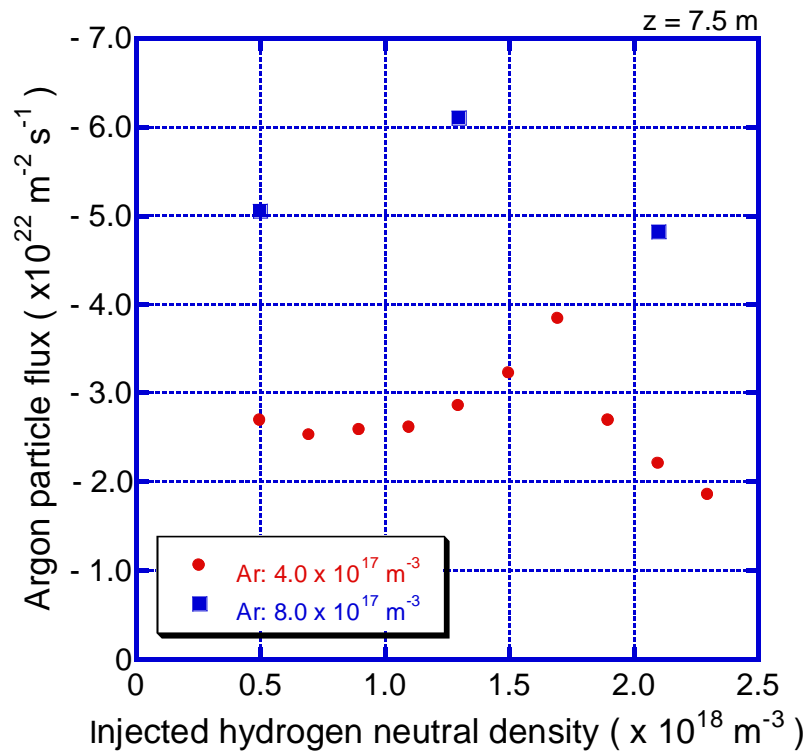


Fig. 38  $\text{Ar}^+$  particle flux toward central-cell on the  $z$ -axis. The red circles indicate the results for the case of  $\text{Ar} : 4.0 \times 10^{17} \text{ m}^{-3}$ . The square symbols show those in case of  $\text{Ar} : 8.0 \times 10^{17} \text{ m}^{-3}$ .

Figure 39 shows 2-D distributions of Argon ion velocity under the condition of injected neutral Ar =  $5.0 \times 10^{17} \text{ m}^{-3}$ ,  $1.7 \times 10^{18} \text{ m}^{-3}$  and  $2.3 \times 10^{18} \text{ m}^{-3}$ . Ar ion velocity flowing toward the central cell near the inlet of plasma region (  $z = 7.5 \text{ m}$  ) is reduced with increasing neutral hydrogen injection. In addition, Ar<sup>+</sup> density at the plasma inlet region decreases shown in Fig. 40. Therefore, the decrease of Ar<sup>+</sup> density and velocity is caused by the reduction of argon ion backflow toward the central cell. The increasing friction force working between hydrogen and argon ions is considered as the factor of reducing Ar<sup>+</sup> velocity shown in Fig. 36.

As mentioned above, Ar<sup>+</sup> density decrease with increase of hydrogen density, however it is seemed that the friction force increases because H<sup>+</sup> density builds up largely shown in Fig. 34. Low  $T_e$  condition introduces the suppression of the electron-impact ionization of Ar.

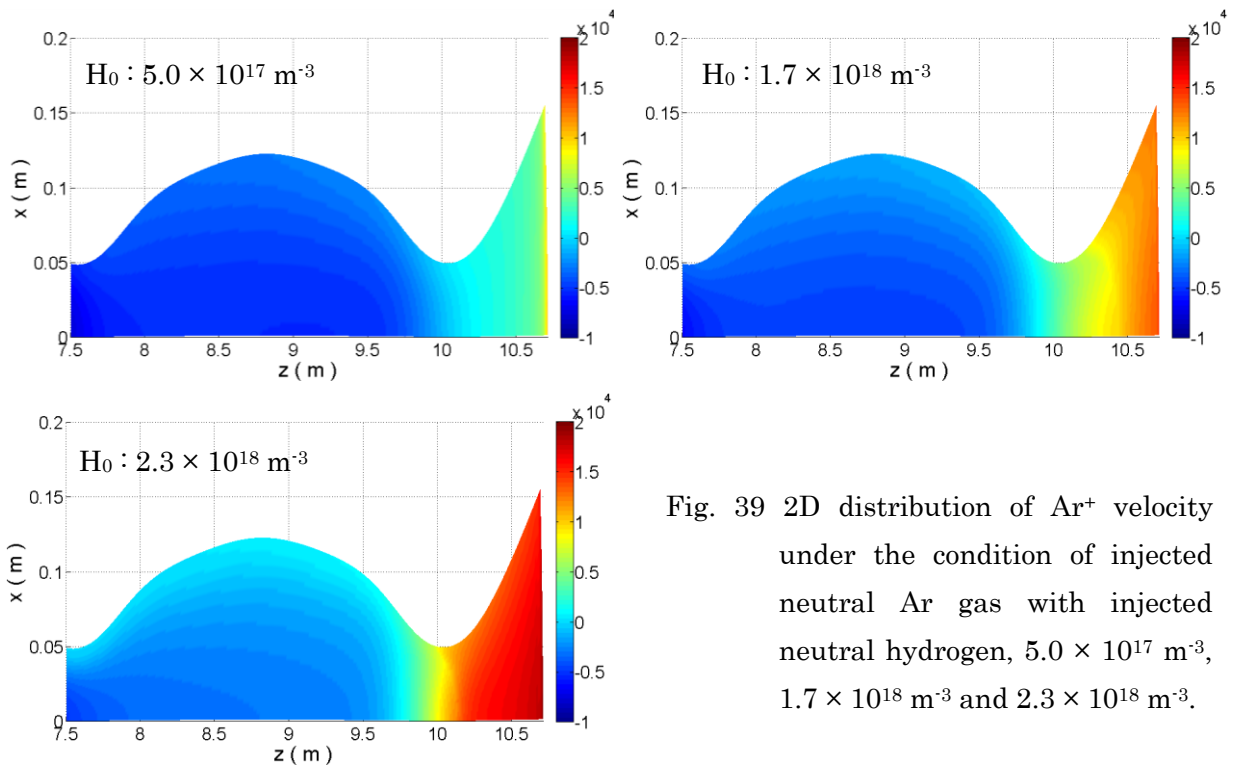


Fig. 39 2D distribution of  $\text{Ar}^+$  velocity under the condition of injected neutral Ar gas with injected neutral hydrogen,  $5.0 \times 10^{17} \text{ m}^{-3}$ ,  $1.7 \times 10^{18} \text{ m}^{-3}$  and  $2.3 \times 10^{18} \text{ m}^{-3}$ .

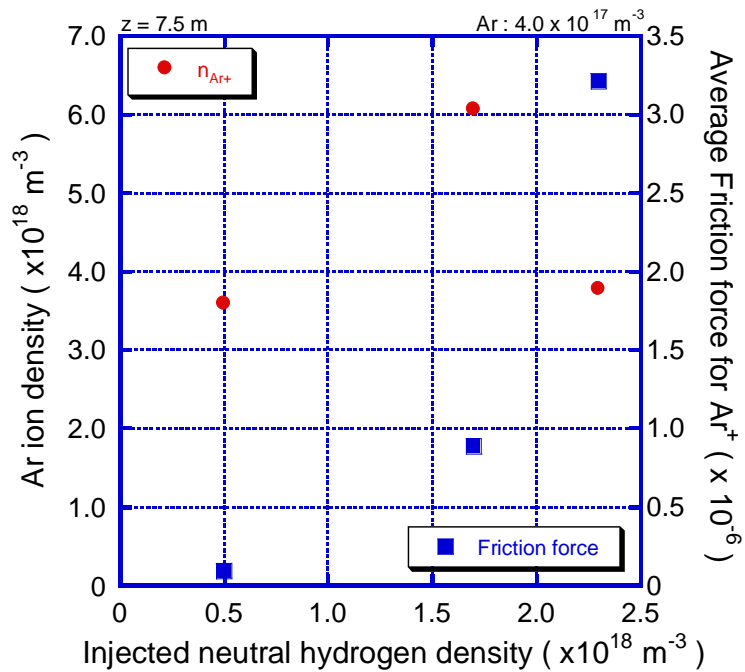


Fig. 40 Dependence of Argon ion density and average friction force worked on the Ar ion.

From above results, the summarization is following below;

(1) Only neutral hydrogen injection;

By the charge exchange loss, ion temperature is reduced. On the other hand, the reduction of electron temperature is produced by electron-impact ionization. However, the reduction of heat load is low and particle flux on the target plate is not decreased.

(2) Only Ar gas injection;

With injecting Ar gas, the decrease of not only hydrogen ion and electron temperatures but also hydrogen ion and argon ion density is observed. However, the electron temperature and hydrogen ion temperature and hydrogen ion density are saturated ( Ar gas =>  $4.0 \times 10^{18} \text{ m}^{-3}$ ) and sheath transfer coefficient tends to be larger. Therefore, heat and particle loads has kept to the constant value.

(3) Simultaneous injection of Hydrogen and Argon gases;

Charge exchange is dominant process for the reduction hydrogen ion temperature. On the other hand, the effective process of the reducing electron temperature is the radiation cooling by Ar gas and loss energy for electron-impact ionization of hydrogen. In this case, heat load on the target plate decreases and saturating particle flux on the target plate is observed. It is shown that the backflow of  $\text{Ar}^+$  velocity is decreased in the high range of the  $n_{\text{Ar}}$ .

(4) Possibility of impurity backflow

The backflow of  $\text{Ar}^+$  tends to increase with building up injected Ar gas density due to the effect of pressure. However,  $\text{Ar}^+$  particle flux toward the central-cell is reduced more than a certain amount of injected neutral hydrogen because of decrease of ionization rate by reduction of electron temperature and increase of friction force by hydrogen ion. However, the effects of the mirror magnetic confinement is not considered by the behavior of impurity. Therefore, it is seemed that the impurity transport analyses using kinetic code such as IMPMC [41] and IMPGYRO [42] is useful for the more accurate understanding of the behavior of impurity.

# Chapter 5

## The combining test the DEGAS code with fluid code

### 5.1 The DEGAS code

Transport of charged particles is constrained by the magnetic field line and for this reason ions and electrons approximately moves along the magnetic field line. In addition, it is easy to satisfy the Knudsen number which does not exceed unity because the SOL plasma tends to become high density and low charge particle temperature. Therefore, plasma transport is often tracked by using fluid code which is low computational load and useful to calculate in the large area. On the other hand, neutral particles are free from magnetic field line. The transportation of neutral particles largely depend on atomic-molecular interaction between charged and neutral particles. It is also important to affect the neutral transport from the effects of geometry because the neutrals transit to various states with transporting between plasma and divertor plate. The mean free path of neutrals is long compared with charge particles. From the above reason, it is considered that the behavior of neutral calculated by kinematic simulation code is accuracy than using the fluid code in the SOL region.

The Monte-Carlo method is employed on the kinematic simulation codes for calculating the neutral transport. In these simulation codes, the Boltzmann equation is directly solved with using pseudo-collision method for particle tracking. These numerical codes which are EIRENE [22, 23, 24], DEGAS [25, 26] and NEUT2D [27] have been developed in everywhere. In this paper, the DEGAS code developed by Heifetz is used for calculating neutral transportation because the DEGAS code has been already applied to the some parts of GAMMA 10/PDX [43, 44, 45, 45]. The DEGAS code calculates the transport of multiple species neutral particles in three-dimensional plasma by using Monte Carlo method and its version is ver. 63. This version 63 of DEGAS has been adapted due to the non-axisymmetric structure of the wall geometry, plasma parameters and non-uniform distribution of the sources of neutral particles [46]. The outline of schematic view is shown in Fig. 41.

In the DEGAS code, the collision between neutral particles and neutral particles except for hydrogen atoms and molecules are ignored. The steady-state solutions are derived from DEGAS code by using below equation.

$$\vec{v} \cdot \nabla f(\vec{x}, \vec{v}) = C(f)(\vec{x}, \vec{v})$$

$\because C(f)$  is neutral-plasma collision term.

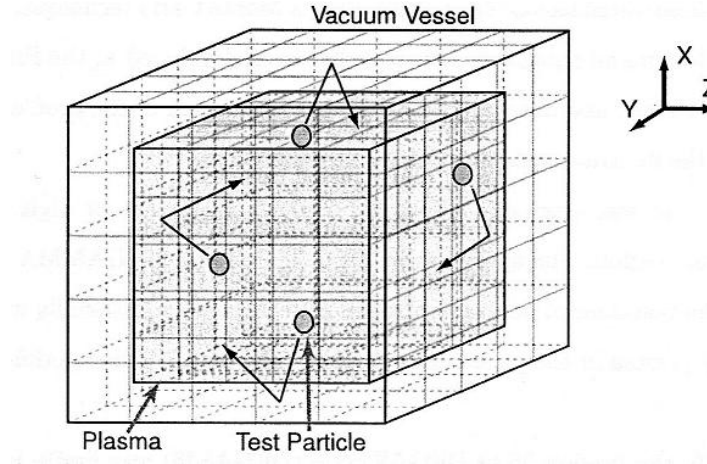


Fig. 41 The outline of schematic view of DEGAS 63.

## 5.2 The method of coupling DEGAS code with fluid code

For the coupling of fluid code and DEGAS code,

- I. First time, the background plasma is calculated by using fluid code.
- II. The plasma parameters such as  $n_i$  : plasma density,  $n_e$  : electron density,  $T_i$  : ion temperature,  $T_e$  : electron temperature,  $u_i, v_i$  : ion velocity that is parallel and perpendicular magnetic field line are handed off to DEGAS code from fluid code.
- III. By using DEGAS code, the distribution of neutral particle is calculated.
- IV. The distribution of neutral hydrogen atom and molecular are introduced to fluid code. At the same time, the volume source terms that are  $S_n, S^{E_i}, S^{E_e}$  and  $S_{mu}$  are delivered to the fluid code.
- V. The plasma parameters are calculated by using fluid code again.
- VI. I ~ V steps is kept to run before giving the corresponding results of the both code.

However, the volume source terms represented in step IV are not delivered to fluid code from DEGAS code in this paper unfortunately. Only the distribution of neutral particle is given in the fluid code.

Figure 42 shows the geometry of the DEGAS mesh for coupling of the fluid code. In GAMMA 10/PDX, the target plate is installed in the divertor simulation module at end-cell. Therefore, the

target plate in the divertor simulation module and the circle shape of target plate are assumed for numerical calculation.

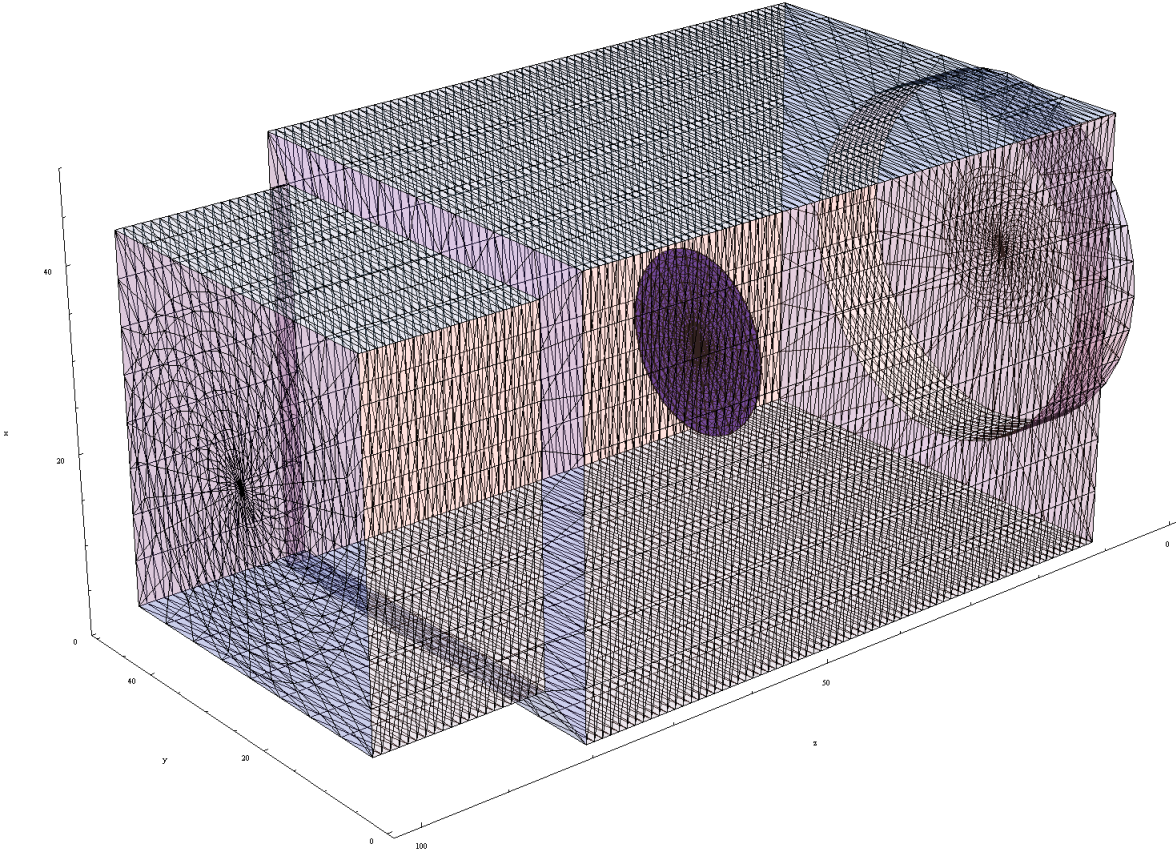


Fig. 42 The schematic view of divertor simulation module with circle target.

In the DEGAS code, atomic molecular processes shown in Table 2 are introduced for hydrogen.

The neutral calculated by DEGAS code is considered only recycling neutral particles from the target plate. The recycling neutral flowing from the target plate has the distribution is given relatively by commensurate ion particle flux reached to the target plate. In addition, recycling coefficient is defined as unity and the velocity of neutral particle generated on the target plate is given as the cosign distribution. The condition of plasma is same with chap. 3. In Fig. 23, the comparison the distribution of neutral particle and  $T_e$  between using analytical model and DEGAS code. Figure 33 (a) indicates the comparison of the distribution of neutral and Fig. 33 (b) represents the comparison of  $T_e$  under the these difference two conditions.

Table 2 Atomic molecular processes in DEGAS code

Charge exchange	$H^+ + H \rightarrow H + H^+$
	$H_2^+ + H_2 \rightarrow H_2 + H_2^+$
	$H^+ + H_2 \rightarrow H_2^+ + H$
Electron impact ionization	$e + H \rightarrow e + H^+ + e$
	$e + H_2 \rightarrow e + H_2^+ + e$
Ion impact ionization	$H^+ + H \rightarrow H^+ + H^+ + e$
	$H^+ + H_2 \rightarrow H^+ + H_2^+ + e$
Electron dissociation	$e + H_2 \rightarrow e + H + H$
	$e + H_2 \rightarrow e + H + H^+ + e$
	$e + H_2^+ \rightarrow H + H$
	$e + H_2^+ \rightarrow e + H^+ + H$
	$e + H_2^+ \rightarrow e + H^+ + H^+ + e$
Recombination	$e + H^+ \rightarrow H$

In Fig. 43 (a.1) and (a.2), the difference of the distribution of neutral density between two conditions is observed obviously. In Fig. 43 (a.1), the distribution of neutral density calculated by DEGAS code is localized near the target plate more than the distribution of neutral density defined by one-dimension ( 1-D ) analytical model. Near the target plate in the case of Monte-Carlo simulation, the neutral density noticeably changes along the radial axis. The neutral density decrease toward radial direction from nearly  $1 \times 10^{18} \text{ m}^{-3}$  to nearly  $3 \times 10^{17} \text{ m}^{-3}$ . These the behavior of neutral density does not observed in Fig. 43 (a.1) clearly. The attenuation rate of neutral density calculated by the DEGAS code toward z axis is higher than the damping rate in case of 1-D analytical model. Under the condition of using the DEGAS code, the half width becomes about 0.01 m on the z axis. The distribution of neutral density does not necessarily exist the peak value on the z axis. In the area from 10.3 m to 10.5 m, neutral density has the peak around  $r = 0.02 \text{ m}$ . On the other hand, the half maximum full-width indicates nearly 0.5 m under the condition of analytical model.

Figure 43 (b) shows the  $T_e$  distribution in the case of used analytical model; (b.1) and used DEGAS code; (b.2). As shown in Fig. 43 ( b.1 ) and ( b.2 ), slightly decrease in  $T_e$  is observed in the case of 1-D analytical model. However, in the case of DEGAS simulation,  $T_e$  does not decreases due to the low neutral density compared with produced by 1-D analytical model. This temperature difference is observed strongly with toward the target plate. Therefore, it is seemed that the effects of neutrals caused by the particle reflection source is not as significant in the case without additional neutral gas injection.

The distributions of neutral density calculated by the DEGAS code or 1-D analytical model differ greatly. It is considered that the difference is caused by the velocity of neutrals. In the analytical model, the neutral velocity is defined as constant along with magnetic field line and the neutral energy escaping from the target plate is assumed by considering the energy reflection coefficient. In the case of the DEGAS code, the neutral velocity is decided as cosign distribution without no constriction of magnetic field. In addition, the energy is assumed by room temperature. Therefore, it is seemed that the mean free path in case of used DEGAS is shorter than in case of used analytical model because the neutral velocity toward the upstream region slows under the DEGAS calculation. Also, including the disappearance of neutral particle for ionization during transport in the calculation area in the DEGAS code influences the distribution of neural density naturally. It is considered that the distribution of the low neutral particle density in the region from  $z = 10.3 \text{ m}$  to  $z = 10.5 \text{ m}$  is related to the penetration length of hydrogen.

By using DEGAS which is kinetic simulation used Monte-Carlo method, the neutral particle transport is calculated and compared with the results from simplified 1-D analytical model. From more accurately calculation of neutral transport, noticeable difference in the distribution of neutral density is observed. From these results, it is likely to estimate the effects of neutral largely than in reality. The same things are applied to the overestimate of the amount of neutral as well. Therefore, it is needed to evaluate the destitution of neutral density by using kinetic code.

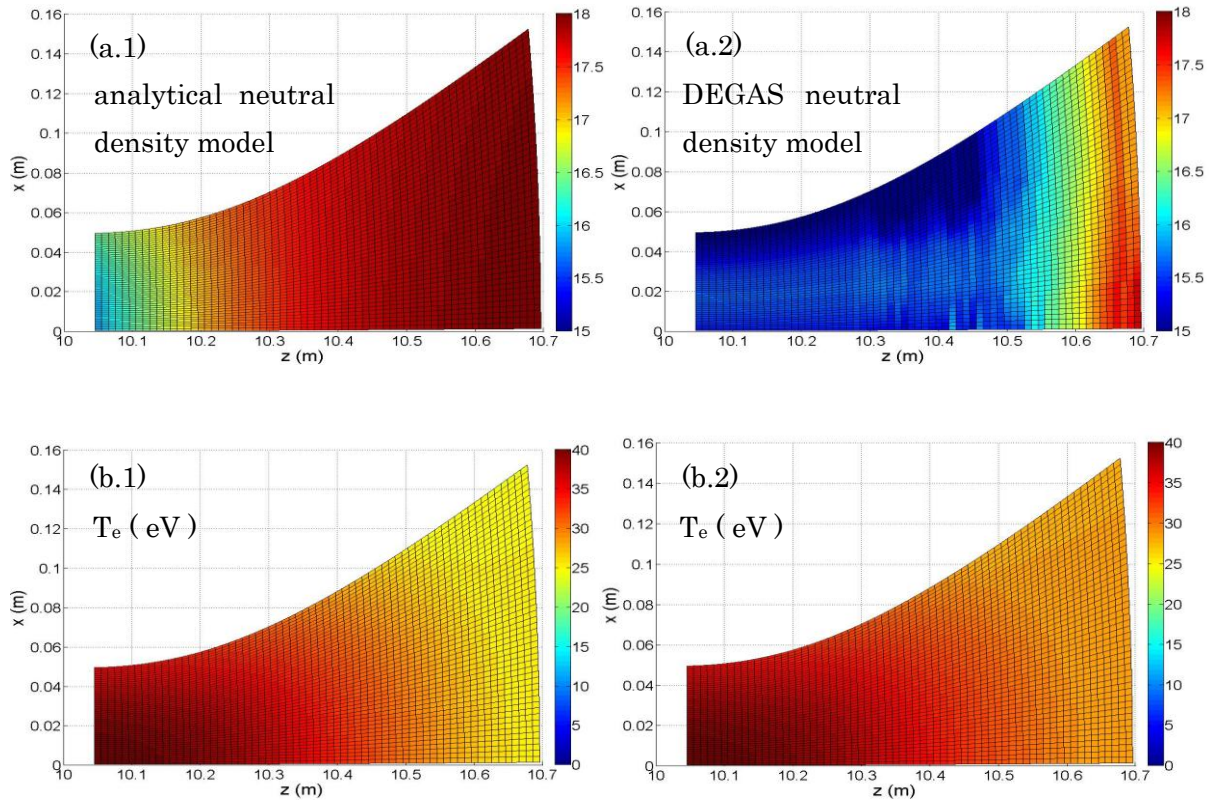


Fig. 43 (a.1) The distribution of neutral density by one dimensional neutral distribution model and (a.2) The distribution of neutral density calculated by DEGAS code. Fig. 23 (b.1) The distribution of  $T_e$  shows under the condition of analytical neutral model and (b.2) the distribution of  $T_e$  is presented in case of using DEGAS code.

# Chapter 6

## Conclusions

In this thesis, we studied the behavior of plasma flow at the end-cell in GAMMA 10/PDX under the various conditions by developing a fluid code for the first time. Adapting the fluid code to the end-cell in the GAMMA 10/PDX is performed by introducing magnetic configuration in the end-cell. For investigating the characteristics of plasma in GAMMA 10/PDX, we made a comparison between the expanded and cylindrical magnetic configuration. In the simulation by using single fluid code under the condition of neutral gas injection into the plasma, the plasma parameters such as electron temperature and plasma density are calculated especially focused on the effects of only neutral particle. The fluid code is improved by introducing the radiation function in the electron energy volume source term. In order to analyze of gas injection effects, we extended single fluid code to multi-fluid code. In addition, the simulation space was extended from end-cell region to the upstream region ( plug/barrier cell ) to evaluate the impurity transport to the upstream. Additional atomic molecular interactions were added in multi-fluid code. Finally, we employed the fully-three dimensional Monte-Carlo simulation code ( DEGAS ver. 63) in order to show more detail neutral particle transportation near the target plate. The behavior of hydrogen neutral particle is compared with one dimensional analytical model and DEGAS result. The finding from the above studies of thesis were summarized as follows.

### 6.1 Adapting fluid code in GAMMA 10/PDX

The fluid code using the fluid model which is based on the same model as B2 code without the effects of drifts and plasma current is developed for analyzing plasma at the end-cell in GAMMA 10/PDX. It is considered that the parameters calculated in the GAMMA 10/PDX mesh structure by using the fluid code becomes convergence successfully. The characteristics of inlet plasma flowing to the end-cell in GAMMA 10/PDX are follows:

- Plasma pressure and density is lower toward the target plate.
- The distribution of ion and electron temperature in the end-cell of the GAMMA 10/PDX has a property similar to the upstream SOL plasma and/or low recycling divertor plasma in tokamaks.
- Ion and electron temperature,  $T_i$  and  $T_e$  are not equilibrating with each other.
- The plasma flow is accelerated at the point of end-cell away from the target plate in the GAMMA 10/PDX.

## 6.2 Comparison between cylindrical and expanded magnetic configuration

The difference between the two meshes is observed obviously. Especially, plasma density has a strong influence from the change of the magnetic field distribution. It is found that the plasma density in the expanded mesh becomes lower than that in the cylindrical mesh and that the effects of particle volume source are easy to be canceled due to the difference of the volume size in the magnetic configuration. Heat load and particle flux reaching the target plate depend on the cross-section area of magnetic flux tube largely. These phenomena are expected to be probable by an analytical solution based on the simple model. The present modeling or code is useful to understand the basic effects of the magnetic flux expansion.

## 6.3 Injection of neutral or impurity gas into the end-cell by using the single fluid code

The influences of neutral or impurity are investigated by using single fluid code. In this simulation, only the effect of Ar atoms are considered as impurity particles.

### *Injection of only hydrogen atoms*

It is shown that  $T_i$  and  $T_e$  decrease due to hydrogen injection. However  $n_i$  increases with injecting neutral hydrogen particles, and hence heat and particle fluxes on the target plate does not decrease by injecting hydrogen gas. It is considered that the energy transport from ion to electron by electron drag interferes with the loss of electron energy. Therefore, the progression of ionization is kept. In the case of low  $T_i$  condition, the decrease of heat and particle fluxes on the target plate are observed. It is clarified that the characteristics of plasma in the end-cell of GAMMA 10/PDX is strongly affected by the condition of plasma parameter with  $T_i \gg T_e$ , that is the electron energy is supported from the energy of ion with the high temperature through e-i collisions. Therefore, it is important to decrease  $T_i$  effectively for the reduction of heat load and particle flux on the target plate.

### *Injection of impurity gas*

Under the condition of low  $T_i$ , the reduction of heat load reached to the target plate are observed, together with the reduction of  $T_e$  with Ar gas injection. By injecting Ar gas, building up of  $n_i$  does not occur because of lower  $T_i$  compared with the condition without Ar gas. It is also found that the degree of heat flux reduction corresponds to the reduction rate of the peak value of the hydrogen

plasma density. In this section, increase of  $n_e$  by the ionization of Ar gas is ignored in single fluid code. Although, the simple model consideration given in this section is useful for obtaining the basic understanding of the effects of neutral injection.

## 6.4 Injection of neutral or impurity gas into the end-cell by using multi-fluid code

In single fluid code, several important effects are neglected and the influence of upstream region is not taken account. Therefore, these effects are included in the fluid code by extending to multi-fluid code and plug/barrier cell.

### *The condition of injection only hydrogen atoms*

With increasing incident hydrogen neutral density into the plasma, heat flux tends to decrease. On the other hand, particle flux tends to keep in increasing. It is observed that the plasma parameters around the west mirror throat change significantly with the amount of injected neutral density. Therefore, it is found that plasma behavior in the plug/barrier cell should not be ignored for understanding the phenomena near the target plate.

### *The only Ar injection effects*

The reduction of ion and electron temperature is observed, however both temperatures are saturated and also the difference of electron and ion temperature remains to be kept with increasing injected Ar gas density. Particle flux of hydrogen and argon ion on the target plate decrease with increasing injected neutral Ar density. On the other hand, heat load on the target plate tends to keep constant value. From these result, it is seemed that Ar particle has the weak effects of reducing hydrogen ion energy although the effect of electron energy reduction is very strong. Therefore, it is needed to decrease hydrogen ion energy for the reduction of heat load.

### *Hydrogen and Argon gases injection at the same time*

In this condition, Ar gas density is fixed as  $4.0 \times 10^{17} \text{ m}^{-3}$  and neutral hydrogen gas density is changed from  $1.0 \times 10^{17} \text{ m}^{-3}$  to  $2.3 \times 10^{18} \text{ m}^{-3}$ . Particle flux on the target plate and hydrogen ion density increase with increasing injected gas density, however the increasing rate of particle flux is lower at the condition of high neutral density injection. On the other hand, Heat flux,  $T_i$  and  $T_e$  decrease at the same conditions. Charge exchange is dominant process for the reduction hydrogen ion temperature. The effective process of the reducing electron temperature is the radiation cooling by Ar gas and loss energy for electron-impact ionization of hydrogen. In this case, the evidence of

passage of detached plasma state is observed.

## 6.5 The test combining with DEGAS code

By using the DEGAS which is kinetic simulation code using Monte Carlo method, the neutral particle transport is calculated and compared with results between using the DEGAS code and an analytical model. The distribution of neutral hydrogen calculated by the DEGAS code localizes near the target plate and does not have the peak value on the z axis. In the case of analytical solution included in the fluid code, neutral distributes in the broaden area and the peak value of the neutral exists on the z axis. The neutral particle transports freely without binding the magnetic field line. However, analytical mode included the fluid code defines neutral velocity as uniform along with magnetic field line. Therefore, it is considered that this differences arises. From results, it is likely to estimate the effects of neutral largely than in reality. In addition, if the adequate amount of neural particles can exist in plug/barrier cell, plasma in the end-cell influences largely. Therefore, it is considered that it is needed to calculate transportation neutral particles to plug/barrier cell from end-cell under the various conditions.

## 6.6 Concluding Remark

In this thesis, by using newly developed fluid code, the behavior of the plasma flow at the end-cell of GAMMA 10/PDX are calculated for divertor simulation experiments under the condition of neutral and/or impurity injection into plasma. In addition, the behavior of recycling neutral particle are evaluated by comparing between using DEGAS code and simple analytical model. These investigations clarified that the characteristic of GAMMA 10/PDX such as circumstances of plasmas  $T_i \ll T_e$  influenced the behavior of end-loss plasma very strongly. The beneficial knowledge obtained from this thesis contributes to the analysis of divertor simulation experiment in the GAMMA 10/PDX under the condition of neutral and/or impurity injections.

# Reference

- [1] K. Ooi, "Technology on the Lithium Recovery from Seawater (1) Adsorbent for Lithium," *Bulletin of the Society of Sea Water Science, Japan*, **51**, 5, pp. 285-288, 1997.
- [2] H. Nobukawa, "Technology on the Lithium Recovery from Seawater (2) Extraction System and Simulation," *Bulletin of the Society of Sea Water Science, Japan*, **51**, 5, pp. 289-292, 1997.
- [3] Y. Miyata, et al., "Research Report," 28, Mar. 1996.
- [4] K. Yoshizuka, and M. Kondo, "Recovery of Lithium from Seawater," *Journal of Plasma and Fusion Research*, **87**, 12, pp. 795-800, 2011.
- [5] The Japan Society of Plasma Science and Nuclear Fusion Research, "Text-Fusion Reactors -Tokamak Reactor Designs and their Basis on Plasma Physics and Reactor Technology-," *Journal of Plasma and Fusion Research*, **87**, Feb. 2011.
- [6] J. Wesson, *Tokamaks* Fourth edition, OXFORD UNIVERSITY PRESS, 2011.
- [7] Y. Shimomura, M. Keilhacker, K. Lackner, H. Murmann, "CHARACTERISTICS OF THE DIVERTOR PLASMA IN NEUTRAL-BEAM-HEATED ASDEX DISCHARGES," *Nuclear Fusion*, **23**, 7, pp. 869-879, 1983.
- [8] B. LaBombard, J. Goetz, C. Kurz, D. Jablonski, B. Lipschultz, G. McCracken, A. Niemczewski, R. L. Boivin, F. Bombarda, C. Christensen, S. Fairfax, C. Fiore, D. Garnier, M. Graf, S. Golovato, R. Granetz, M. Greenwald, S. Horne, A. Hubbard, et al., "Scaling and transport analysis of divertor conditions on the Alcator C - Mod tokamak," *Physics of Plasmas*, **2**, 6, pp. 2242-2248, 1995.
- [9] B. LaBombard, J.A. Goetz, I. Hutchinson, D. Jablonski, j. Kesner, C. Kurz, B. Lipschultz, G.M. McCracken, A. Niemczewski, J. Terry, A. Allen, R.L. Boivin, F. Bombarda, P. Bonoli, C. Christensen, C. Fiore, D. Gamier, et al., "Experimental investigation of transport phenomena in the scrape-off layer and divertor," *Journal of Nuclear Materials*, **241-243**, pp. 149-166, 1997.
- [10] T.W. Petrie, D.N. Hill, S.L. Allen, N.H. Brooks, D.A. Buchenauer, J.W. Cuthbertson, T.E. Evans, P. Ghendrih, C.J. Lasnier, A.W. Leonard, R. Maingi, G.D. Porter, D.G. Whyte, R.J. Groebner, R.A. Jong, M.A. Mahdavi, S.J. Thompson, W.P. West and R.D. Wood, "RADIATIVE DIVERTOR EXPERIMENTS IN DIII-D WITH D2 INJECTION," *Nuclear Fusion*, **37**, 3, pp. 321-338, 1997.
- [11] A. Loarte, R.D. Monk, J.R. Martín-Solís, D.J. Campbell, A.V. Chankin, S. Clement, S.J. Davies, J. Ehrenberg, S.K. Erents, H.Y. Guo, et al., "PLASMA DETACHMENT IN JET MARK I DIVERTOR EXPERIMENTS," *Nuclear Fusion*, **38**, 3, pp. 331-371, 1988.

- [12] N. Ezumi, S. Mori, N. Ono, M. Takagi, S. Tkamura, H. Suzuki and J. Park, "Density threshold for plasma detachment in gas target," *Journal of Nuclear Materials*, **241-243**, pp. 349-352, 1997.
- [13] H. TAKEDA, Y. NAKASHIMA, K. HOSOI, K. ICHIMURA, T. FURUTA, K. HIGASHIYAMA, M. TOMA, A. HATAYAMA, T. ISHII, H. UEDA, M. SAKAMOTO, M. ICHIMURA, M. YOSHIKAWA, J. KOHAGURA and T. IMAI, "Divertor Simulation Study Using the GAMMA 10 End-Mirror Cell," *Plasma and Fusion Research*, **7**, 2405151, 2012.
- [14] R. Behrisch and W. Eckstein, "Ion Backscattering from Solid Surfaces," *Physics of Plasma-Wall Interactions in Controlled Fusion*, pp. 413-438, 1986.
- [15] T. KUWABARA, T. CHO, and Y. SAKAMOTO, "A new end-loss-ion energy analyzer with obliquely placed multigrids for open-ended plasma diagnostics," *Review of Scientific Instruments*, **65**, 4, pp. 936-942, 1994.
- [16] Arthur W. Molvik, "Large acceptance angle retarding - potential analyzers," *Review of Scientific Instruments*, **52**, 5, pp. 704-711, 1981.
- [17] A. Hatayama, H. Segawa, R. Schneider, D.P. Coster, N. Hayashi, S. Sakurai, N. Asakura and M. Ogasawara, "High Mach flow associated with X point MARFE and plasma detachment," *Nuclear Fusion*, **40**, 12, pp. 2009-2021, 2000.
- [18] B.J. Braams, "A Multi-Fluid Code for Simulation of the Edge Plasma in Tokamaks," vol. NET Rep. 68, no. EURFU/XII-80/87/87/68, CEC, Brussels, 1987.
- [19] V.A. Rozhansky, S.P. Voskoboinikov, E.G. Kaveeva, D.P. Coster and R. Schneider, "Simulation of tokamak edge plasma including self-consistent electric fields," *Nuclear Fusion*, **41**, 4, pp. 387-401, 2001.
- [20] R. Schneider, X. Bonnin, K. Borrass, D. P. Coster, H. Kastelewicz, D. Reiter, V. A. Rozhansky, and B.J. Braams, "Plasma Edge Physics with B2-Eirene," *Contributions to Plasma Physics*, **46**, 1-2, pp. 3-191, 2006.
- [21] T.D. Rognlien, J.L. Milovich, M.E. Rensink and G.D. Porter, "A fully implicit, time dependent 2-D fluid code for modeling tokamak edge plasmas," *Journal of Nuclear Materials*, **196-198**, 1, pp. 347-351, 1992.
- [22] D. Reiter, H. Kever, G.H. Wolf, M. Baelmans, R. Behrisch, R. Schneider, "Helium removal from tokamaks," *Plasma Physics and Controlled Fusion*, **33**, 13, pp. 1579-1600, 1991.
- [23] D. Reiter, "Progress in two-dimensional plasma edge modelling," *Journal of Nuclear Materials*, **196-198**, 1, pp. 80-89, 1992.
- [24] D. Reiter, M. Baelmans, P. Börner, "The EIRENE and B2-EIRENE Codes," *Fusion Science and Technology*, **47**, 2, pp. 172-186, 2005.

- [25] D. Heifetz, D. Post, M. Petravic, J. Weisheit, G. Bateman, "A Monte-Carlo Model of Neutral-Particle Transport in Diverted Plasmas," *Journal of Computational Physics*, **46**, 2, pp. 309-327, 1982.
- [26] D.B. Heifetz, "Physics of Plasma-Wall Interactions in Controlled Fusion. Eds. D.E. Post and R. Behrisch," Plenum Press, New York, p. 695, 1986.
- [27] K. Shimizu, T. Takizuka, S. Sakurai, H. Tamai, H. Takenaga, H. Kubo, Y. Miura, "Simulation of divertor detachment characteristics in JT-60 with superconducting coils," *Journal of Nuclear Materials*, **313-316**, pp. 1277-1281, 2003.
- [28] C. Salmange, et al., in 9th International Conference on Open Magnetic System for Plasma Confinement and The 3rd International Workshop on Plasma Material Interaction Facilities for Fusion, Tsukuba, Japan, 2012.
- [29] M. Baeva, W.J. Goedheer, N.J. Lopes Cardozo, D. Reiter, "B2-EIRENE simulation of plasma and neutrals in MAGNUM-PSI," *Journal of Nuclear Materials*, **363-365**, pp. 330-334, 2007.
- [30] B. de Groot, Z. Ahmad, R.P. Dahiya, R. Engeln, W.J. Goedheer, N.J. Lopes Cardozo, V. Veremiyenko, "Magnum-psi, a new linear plasma generator for plasma-surface interaction studies in ITER relevant conditions," *Fusion Engineering and Design*, **66-68**, pp. 413-417, 2003.
- [31] S.I. Braginskii, "Transport Properties in a Plasma, in Review of Plasma Physics, M.A. Leontovich," **1**, pp. 205-311, 1965.
- [32] Vladislav Kotov, Detlev Reiter, Andrey S. Kukushkin, "Numerical study of the ITER divertor plasma with the B2-EIRENE code package," Bericht des Forschungszentrums Julich Jul-4257, November 2007.
- [33] S. V. PATANKAR and D. B. SPALDING, "A CALCULATION PROCEDURE FOR HEAT, MASS AND MOMENTUM TRANSFER IN THREE-DIMENSIONAL PARABOLIC FLOWS," *International Journal of Heat and Mass Transfer*, **15**, pp. 1787-1806, 1971.
- [34] S. V. Patankar, *Numerical Heat Transfer and Fluid Flow*, New York: Hemisphere, 1980.
- [35] H.J. Stone, "Iterative Solution of Implicit Approximations of Multi-Dimensional Partial Differential Equations," *SIAM JOURNAL OF THE SOCIETY FOR INDUSTRIAL AND APPLIED MATHEMATICS*, **5**, pp. 530-558, 1968.
- [36] T. Higashiyama, et. al., Master thesis of Keio University, 2011.
- [37] F.F. Chen, *Introduction to Plasma Physics*, New York: Plenum Press, 1974.
- [38] D.E. Post, "A review of recent developments in atomic processes for divertors and edge plasmas," *Journal of Nuclear Materials*, **220-222**, pp. 143-157, 1995.
- [39] P.C. Stangeby : *The Plasma Sheath, Physics of Plasma-Wall Interactions in Controlled Fusion*, ed. by D.E. Post and R. Behirish, NATO ASI Serise B: Vol. 131, Plenum Press, New York (1986.)
- [40] G.D. Hobbs and J.A. Wesson : *Plasma Phys.* **9** 85 (1967.)

- [41] K. Shimizu et al. *J. Nucl. Mater.* **220-222**, 410 (1995).
- [42] A. Fukano et al. *J. Nucl. Mater.* **363-365**, 211 (2007).
- [43] Y. Nakashima, K. Yatsu, K. Tsuchiya, M. Ichimura, N. Yamaguchi, M. Inutake, M. Shoji, K. Ohtoshi, T. Tamano, S. Miyoshi, "Investigation of recycling in the GAMMA 10 tandem mirror," *Journal of Nuclear Materials*, **196-198**, 1, pp. 493-497, 1992.
- [44] K. Yatsu, Y. Nakashima, T. Cho, M. Ichimura, N. Yamaguchi, K. Tsuchiya, M. Inutake, and S. Miyoshi, "Improvement of plasma confinement by wall conditioning in the tandem mirror GAMMA 10," *Journal of Nuclear Materials*, **176-177**, pp. 404-408, 1990.
- [44] S. Kobayashi, Y. Nakashima, M. Shoji, K. Tsuchiya, Y. Hasegawa, M.K. Islam, N. Yamaguchi, M. Yoshikawa, A. Mase, T. Tamano, and K. Yatsu, "Neutral particle transport under strong hydrogen recycling condition in the GAMMA 10 central cell," *Journal of Nuclear Materials*, **266-269**, pp. 566-570, 1999.
- [45] S. KOBAYASHI, Y. NAKASHIMA, M. SHOJI, K. TSUCHIYA, Y. ISHIMOTO, H. AMINAKA, N. YAMAGUCHI, M. YOSHIKAWA, T. TAMANO and K. YATSU, "Hydrogen Recycling in a Long-Pulse Discharge Plasma on the Tandem Mirror GAMMA 10," *Journal of Plasma and Fusion Research SERIES*, **3**, pp. 303-306, 2000.
- [46] D. P. Stotler, C. H. Skinner, R. V. Budny, A. T. Ramsey, D. N. Ruzic, and R. B. Turkot Jr., "Modeling of neutral hydrogen velocities in the Tokamak Fusion Test Reactor," *Physics of Plasmas*, **3**, 11, pp. 4084-4094, 1996.

# Acknowledgments

The author would like to express his sincere gratitude to Prof. Y. Nakashima at University of Tsukuba for his continuous guidance and assists in the course of the present study. His helpful advices or suggestions and deep discussions are absolutely imperative for the accomplishment of the present studies.

He would like to deeply appreciate Prof. A. Hatayama at Keio University for his significant discussions and invaluable aids and suggestions for the developing the fluid code and the resolution of the numerical problems. The simulation study using the fluid code can be made solid progress thanks to his substantial help.

He especially thanks to Prof. M. Sakamoto and Assoc. Prof. M. Yoshikawa at University of Tsukuba for significant advices for accomplishment of this thesis.

Also, he acknowledges Prof. M. Ichimura at University of Tsukuba and Prof. T. Imai at University of Tsukuba for the study of the phenomena of plasma by using the GAMMA 10/PDX and useful suggestion about this study.

He wishes to thanks to the member of NBI group for their discussions and encouragements.

This study is partly supported by the bi-directional collaboration research program of National Institute for Fusion Science , Keio University and University of Tsukuba.

Finally, he would like to thank the member of GAMMA 10/PDX groups for their collaboration in the experiments and for helpful discussions.